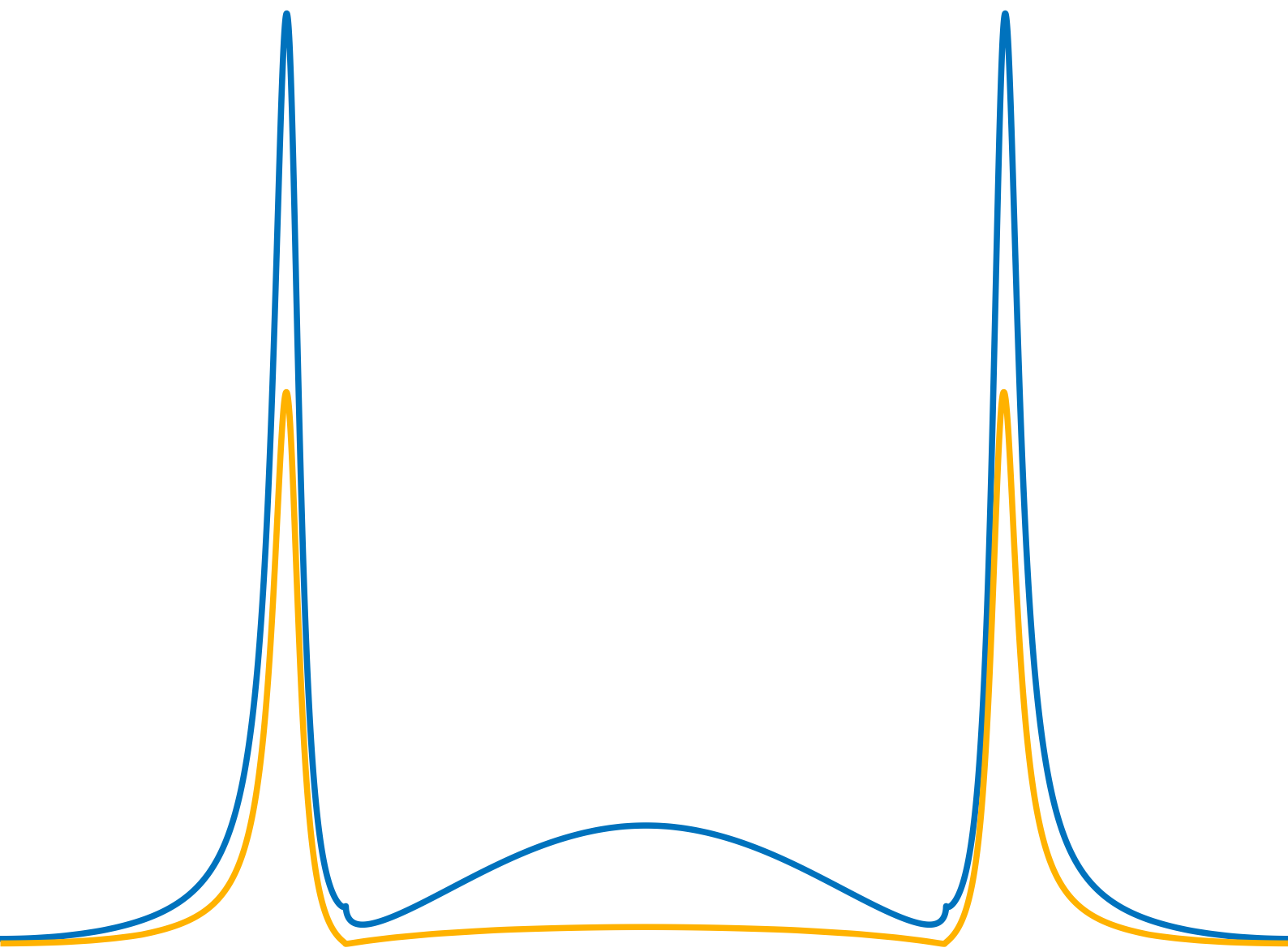


Optimization of SPP Excitation for Nanofibers Deposited on a Silver Film

Master's Thesis
Christian Storgaard & Søren Rulle
10th of June, 2019





AALBORG UNIVERSITY
STUDENT REPORT

**Fifth year at The Faculty-
of Engineering and Science**
Physics
Skjernvej 4a
9220 Aalborg
<http://www.mp.aau.dk/>

Title:

Optimization of SPP Excitation for
Nanofibers Deposited on a Silver Film

Project:

Master's Thesis

Project period:

February 2019 - June 2019

Project group:

5.317b

Students:

Christian Storgaard Kristensen
Søren Rulle

Supervisor:

Thomas Søndergaard

Pages: 77

Appendix: 2

Submission date 10-06-2019

Abstract:

I dette projekt er kohærent lokal eksitation af overflade plasmon polaritoner (forkortet SPPs) ved hjælp af lineær spredning i individuelle organiske 1-cyano-p-quaterphenylene (CNHP4) nanofibre lagt på en sølvfilm teoretisk analyseret. Specifikt er fiberdimensioneringen analyseret i et forsøg på at optimere eksitationen af SPPs, samt at kunne forudsige hvilken geometri der er bedst. Sølvlaget er lagt på et glas substrat for at kunne observere mængden af lækkede SPPs. Andre faktorer som orienteringen af dipoler inde i fiberen for anden harmonisk generering (forkortet SHG), samt sølvfilmens tykkelse bliver også undersøgt på samme grundlag. Det blev dog ikke muligt at finde en rigid model som forudsiger den bedst mulige størrelse af fiberen, dette er grundet at en højere fiber introducere komplicerede effekter som gør det svært at fortolke. En hypotese er sat op der beskriver ét aspekt af de observerede effekter, men denne kan ikke konstituere en fuldendt model. Ydermere er eksitering af SH-SPPs i 3D blevet analyseret med henblik på dipol orientering i søgen efter størst asymmetrisk SHG. Den kritiske tykkelse af sølvfilms laget viser sig at være afhængig af fiber størrelsen og giver derfor ikke konkluderbare resultater.

Preface

This report is written by Christian Storgaard and Søren Rulle from the 4th semester of the master in physics at the Department of Materials and Production, Aalborg University. The subject of the project is *Optimization of SPP Excitation for Nanofibers Deposited on a Silver Film* and has the purpose of studying the optimal geometry for organic nanofibers in relation to excitation of surface plasmon polaritons on a silver-air interface.

The report is divided into three parts; a theoretical introduction which is necessary for the understanding of formulae and concepts used to describe and discuss the results; an analyzing part where different geometries are considered, and lastly a concluding part where the theoretical knowledge is utilized to discuss and conclude upon the results.

Reading Guide

In this report, references are a part of the text and are collected in the bibliography in the back of the report. In this report the references are indicated with [number]. These numbers refer to the bibliography where books are stated with author, title, edition, and publisher while web-pages are stated with author, title and the date the information was gathered.

In the text, vectors are shown as \mathbf{A} , normal vectors are shown as $\hat{\mathbf{A}}$, matrices are shown as $\overline{\overline{\mathbf{A}}}$ and tensors is shown as $\overleftrightarrow{\mathbf{A}}$.

Figures and tables are numbered according to the chapter they appear in, i.e. the first figure in chapter 2 is numbered 2.1, the second figure has the number 2.2, etc. Both figures and tables have an explaining caption placed below.

Christian Storgaard Kristensen

Søren Rulle

Table of Contents

Chapter 1 Introduction	1
1.1 Historical Context	1
1.2 Case Study	2
1.2.1 Objective	3
Chapter 2 Introductory Theory	5
2.1 Maxwell's Equations	5
2.1.1 The Wave Equations	7
2.1.2 Poynting Vector	7
2.2 Surface Plasmons Polaritons	8
2.2.1 Derivation of the Dispersion Relation for SPPs	8
2.2.2 Surface Plasmon Polariton Properties	9
Chapter 3 Scattering Problem in Two Dimensions	13
3.1 Green's Function Area Integral Equation	13
3.1.1 Calculations for s -polarization	14
3.1.2 Calculations for p -polarization	15
3.2 Scatterer on a Layered Structure	15
3.2.1 Plane Wave Expansion of the Green's Function	16
3.2.2 Calculations for p -polarization	19
3.3 Green's Function Area Integral Equation in the Far Field	21
3.4 Optical Cross Section	23
3.4.1 Differential Cross Section	27
3.5 Mode Index Analysis	27
3.5.1 Preliminary Theory	28
3.5.2 Results	28
Chapter 4 Scattering Problem in Three Dimensions	31
4.1 Scatterer On a Layered Structure	31
4.1.1 Direct Green's Tensor	31
4.1.2 Indirect and Transmitted Green's Tensor	32
4.2 Far Fields and Cross Sections	34
4.3 Second Harmonic Generation	35
Chapter 5 Numerical Conversion and Solution Method	37
5.1 Discretization into Square Elements	37

5.2	Numerical Method	38
5.3	Applying the Fast Fourier Transform	40
Chapter 6 Analysis of Results in Two Dimensions		43
6.1	Convergence of the Model	43
6.2	Effective Dimensions of a Fiber for Plasmon Excitation	45
6.2.1	Effect of the Width of the Fiber	46
6.2.2	Effect of the Height of the Fiber	53
6.2.3	Summary	58
6.3	Near Field Examination and Alternative Hypothesis	59
6.4	Effect of the Thickness of the Silver Film	62
Chapter 7 Analysis of Results in Three Dimensions		65
7.1	Preliminary Theory	66
7.2	Asymmetric Coupling by Dipole Orientation	66
7.3	Comparing Linear Scattering to SH Scattering	70
Chapter 8 Conclusion		73
Bibliography		75
Appendix A Additional Theory		79
A.1	Boundary Conditions	79

Chapter 1

Introduction

1.1 Historical Context

In 1959 a patent was raised for the idea of integrated circuits (ICs), which is a miniaturized circuit that made use of transistors, by Jack Kilby [1][2]. An IC is essentially a connected array of transistors and other electronic components designed to perform a specific task. This invention made it possible to replace vacuum tubes which was widespread in electronic applications, thus sparking a whole revolution in electronics and opening a span of possibilities of applications. Independently of Jack Kilby the IC was developed by Robert Noyce, thus highlighting the necessity of replacing Vacuum tubes [1][2]. Technology today still relies on the invention, as do it on the discovery of transistors, which is made smaller and faster at an ongoing pace. Jack Kilby's own words illustrates the impact of the technology.

"What we didn't realize then was that the integrated circuit would reduce the cost of electronic functions by a factor of a million to one, nothing had ever done that for anything before."

-Jack Kilby

However, it is an ongoing task to better the already great performance that has been achieved up to this very day. Research in the field of nanostructures in regards to graphene has been suggested as a promising tool to improve electronic components. However, the use of graphene has its issues, e.g. patterning of the graphene lattice compromises the lattice structure such that it becomes a less efficient conductor [3]. Solutions are already being developed using embedded graphene in a sandwiched layered structure as shown in Ref. [3]. The advancement in the field of graphene and graphene related materials can very well become the new standard material in ICs as it is already a well studied material and can find its use for a great deal of applications as shown in Ref. [4].

However, all these new technologies still relies on the idea of pushing electrons around as the main mechanism that enables electronic components to work. An alternative to using electronic components and using electrons as signals can be by using photons and smart optical components to achieve the same thing. The technology is based on the subject of nano-optics which is the study field of near-field optics, plasmonics, photonic crystals to name a few. In plasmonics particular, the research of bound light at an interface is of

interest when trying to construct an IC based on light interaction. Effort has been put into developing the necessary advances, which has made progress at an increasing pace in the last decade [5]. One crucial step is developing a component which can locally excite surface plasmon polaritons (SPPs) in a desired direction. It has been shown that this is already possible using grating, ridge and slit couplers to locally excite SPPs in for example Ref. [6]. However, with the use of non-linear effects, such as second harmonic generation, it can also be achieved. The additional effect of being able to use a near-infrared pump beam which generates SPPs in the visible range can prove useful as visible light is easier to detect or use afterwards in other optical components [5]. One such way of achieving these non-linear effects is by using specifically grown nanofibers which has been shown in Ref. [5] and [7]. Thus they are of great interest and will therefore be the focus of this rapport.

1.2 Case Study

It has become possible to grow organic 1-cyano-p-quaterphenylene (CNHP4) crystalline nano-fibers with a large second order non-linear properties, which is able to efficiently create second harmonic (SH) radiation [8][9]. This effect has been used in the works of Ref. [5] and [7] for nano-fibers deposited on an air-silver interface. The detection of SPPs at the air-silver interface was possible due to leakage radiation into the substrate at a larger angle than the critical angle for an air-glass interface, which for these cases was quartz. The general layered structure thus becomes of the form as shown in Figure 1.1. It was shown that an ensemble of fibers lead to a symmetric second harmonic generation (SHG), however asymmetric scattering for the SHG was achieved in Ref. [5] focusing on a single fiber, thus showing a non-symmetric generation of SPPs. The test conducted in the article compares linear scattering using a fundamental harmonic (FH) wavelength of 390 nm pump beam to SHG using a FH wavelength of 780 nm.

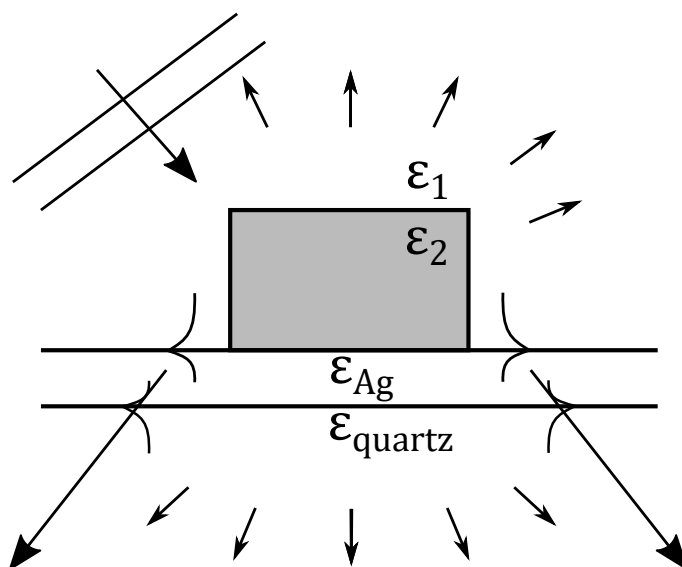


Figure 1.1. Illustrated cross section of a fiber deposited on top of a silver film on a quartz substrate. The fiber is illuminated by an incoming light beam and the light is then scattered, including coupling into surface plasmon polariton modes at both interfaces.

These fibers consists of dipoles that are oriented at an angle in relation to the interface. It is this angle that enables the asymmetric generation. In the experiment analyzed in Ref. [5] a 100 nm high and 350 nm wide fiber was considered. However, these resulted in weak excitation of SPPs and in Ref. [10] it is hypothesized that this could be due to interference inside of the fiber. This would result in fibers with widths near the SPP wavelength at the air/silver interface to diminish plasmon excitation. In Ref. [10] an example of a three dimensional fiber that is 100 nm in height, 100 nm in width and 400 nm in length is shown. This fiber is significantly better at exciting SPPs than the previously examined fibers. This could suggest that the aforementioned hypothesis could be have truth to it.

1.2.1 Objective

In order to create the best possible circumstances for excitation of SPPs, it is thus of great interest to examine the ability to excite such SPPs of fibers of different dimensions. The aim thus becomes to confirm or deny the aforementioned hypothesis, and hopefully create a rigid model that can predict the optimal dimensions of a fiber for a given pump beam wavelength.

This will be done by doing theoretical calculations, based on the Green's function integral equation method that is presented in Ref. [10]. It is assumed that the width and height of the fiber will have the largest effect on SPP excitation, and that in practice most fibers will have a length significantly larger than both the width or height. Therefore, this examination will be limited to the two dimensional case. This is also done as three dimensional calculations are much heavier computationally. In order to create a data set of different dimensions of sufficient size, the method used in Ref. [5] and [7] have to be improved in computation time and complexity. This will be achieved by applying the fast Fourier transformation algorithm as well as solving the problem iteratively, by the conjugate gradient algorithm.

In addition to the dimensions of the fiber, the impact of the thickness of the silver layer, thus a full analysis of the geometry of the overall structure will be conducted. For this geometrical analysis of the structure, both in changing the dimensions of the fibers and the thickness of the silver film, linear scattering will be applied.

Furthermore, and separate from the aforementioned analysis, an examination of the effects of SHG in three dimensions will be conducted. The aim here will be to test the effects of the orientation of the dipoles in the fibers. This is done by changing the orientation of the dipoles defined by two angles.

Chapter 2

Introductory Theory

2.1 Maxwell's Equations

When working with Maxwell's equations it is easier to consider them in the frequency domain, as this simplifies the derivations substantially. In order to do so, consider Maxwell's equations in the time domain, in which the macroscopic Maxwell's equations are given as

$$\nabla \times \mathbf{E}(\mathbf{r}, t) = -\frac{\partial \mathbf{B}(\mathbf{r}, t)}{\partial t}, \quad (2.1)$$

$$\nabla \times \mathbf{H}(\mathbf{r}, t) = \mathbf{J}(\mathbf{r}, t) + \frac{\partial \mathbf{D}(\mathbf{r}, t)}{\partial t}, \quad (2.2)$$

$$\nabla \cdot \mathbf{D}(\mathbf{r}, t) = \rho(\mathbf{r}, t), \quad (2.3)$$

$$\nabla \cdot \mathbf{B}(\mathbf{r}, t) = 0, \quad (2.4)$$

where \mathbf{E} is the electric field, \mathbf{H} is the magnetic field, \mathbf{D} is the electric displacement field, \mathbf{B} is the magnetic induction field, ρ is the free charge density and \mathbf{J} is the free current density [11][10].

The electromagnetic properties of matter is often described by the macroscopic polarization density \mathbf{P} and magnetization density \mathbf{M} , which is related to the electric field and the magnetic induction field by

$$\mathbf{D}(\mathbf{r}, t) = \varepsilon_0 \mathbf{E}(\mathbf{r}, t) + \mathbf{P}(\mathbf{r}, t), \quad (2.5)$$

$$\mathbf{B}(\mathbf{r}, t) = \mu_0 (\mathbf{H}(\mathbf{r}, t) + \mathbf{M}(\mathbf{r}, t)). \quad (2.6)$$

However, for practical purposes in the field of optics, the magnetization density is a negligible factor and is thus not considered [10]. This results in the direct relation $\mathbf{B} = \mu_0 \mathbf{H}$. In linear, local and isotropic media, which will be one of the main assumptions of this report, the polarization and current density follows roughly the same form,

$$\mathbf{P}(\mathbf{r}, t) = \varepsilon_0 \int_{t'} \chi(\mathbf{r}, t - t') \mathbf{E}(\mathbf{r}, t') dt', \quad (2.7)$$

$$\mathbf{J}(\mathbf{r}, t) = \mathbf{J}_s(\mathbf{r}, t) + \int_{t'} \sigma(\mathbf{r}, t - t') \mathbf{E}(\mathbf{r}, t') dt', \quad (2.8)$$

where \mathbf{J}_s is the source current density and σ and χ are the conductivity and the susceptibility respectively [6][10]. These integrals are known as convolution integrals and

the convolution theorem states that when the Fourier transform is applied on a convolution integral, it becomes the transformed product of the constituents of the integrand [12]. The Fourier transform and its reverse can now be applied to $\mathbf{P}(\mathbf{r}, t)$ as

$$\mathbf{P}(\mathbf{r}, t) = \int_{\omega} \mathbf{P}(\mathbf{r}, \omega) e^{-i\omega t} d\omega, \quad (2.9)$$

$$\mathbf{P}(\mathbf{r}, \omega) = \frac{1}{2\pi} \int_t \mathbf{P}(\mathbf{r}, t) e^{i\omega t} dt. \quad (2.10)$$

This can be done in the same manner to every field in the Maxwell's equations as well as the current density. Thus, following the convolution theorem, in the frequency domain $\mathbf{P}(\mathbf{r}, \omega)$ can be written simply as

$$\mathbf{P}(\mathbf{r}, \omega) = \varepsilon_0 \chi(\mathbf{r}, \omega) \mathbf{E}(\mathbf{r}, \omega). \quad (2.11)$$

In the same manner, the current density can be written as,

$$\mathbf{J}(\mathbf{r}, \omega) = \mathbf{J}_s(\mathbf{r}, \omega) + \sigma(\mathbf{r}, \omega) \mathbf{E}(\mathbf{r}, \omega). \quad (2.12)$$

Consider now the Fourier transform of equation (2.2),

$$\nabla \times \mathbf{H}(\mathbf{r}, \omega) = \mathbf{J}_s(\mathbf{r}, \omega) + \sigma(\mathbf{r}, \omega) \mathbf{E}(\mathbf{r}, \omega) - i\omega \varepsilon_0 (1 + \chi(\mathbf{r}, \omega)) \mathbf{E}(\mathbf{r}, \omega). \quad (2.13)$$

This can be derived by inserting the time domain fields written in the same manner as equation (2.9) into (2.2) and then letting the time derivative work on the exponential $e^{-i\omega t}$ and afterwards leave out the Fourier transform as it is working on every term of the equation. From this expression the displacement can be written as

$$\mathbf{D}(\mathbf{r}, \omega) = \varepsilon_0 \left(1 + \chi(\mathbf{r}, \omega) + \frac{i\sigma(\mathbf{r}, \omega)}{\omega \varepsilon_0} \right) \mathbf{E}(\mathbf{r}, \omega), \quad (2.14)$$

and hence, a new factor that correlates the displacement field to the electric field can be introduced, this factor is termed the relative dielectric constant,

$$\varepsilon(\mathbf{r}, \omega) = 1 + \chi(\mathbf{r}, \omega) + \frac{i\sigma(\mathbf{r}, \omega)}{\omega \varepsilon_0}. \quad (2.15)$$

Then the Maxwell's equation can be simplified in the frequency domain to

$$\nabla \times \mathbf{E}(\mathbf{r}, \omega) = i\omega \mu_0 \mathbf{H}(\mathbf{r}, \omega), \quad (2.16)$$

$$\nabla \times \mathbf{H}(\mathbf{r}, \omega) = \mathbf{J}_s(\mathbf{r}, \omega) - i\omega \varepsilon_0 \varepsilon(\mathbf{r}, \omega) \mathbf{E}(\mathbf{r}, \omega), \quad (2.17)$$

$$\nabla \cdot \mathbf{D}(\mathbf{r}, \omega) = \rho_s(\mathbf{r}, \omega), \quad (2.18)$$

$$\nabla \cdot \mathbf{B}(\mathbf{r}, \omega) = 0, \quad (2.19)$$

where $\rho_s = \nabla \cdot \mathbf{J}_s / i\omega$. Maxwell's equations will be considered in this domain as it simplifies all time derivatives as these can be effectively replaced with a $-i\omega$ factor. Since this is the case, fields like $\mathbf{E}(\mathbf{r}, \omega)$ is often noted as $\mathbf{E}(\mathbf{r})$, thus the dependence of ω is implicitly understood.

2.1.1 The Wave Equations

An essential part of the theory is the wave equations for the electric and magnetic fields, as they state the general behavior of the waves in question. To derive these equations one can take the curl of equations (2.16) and (2.17), which yields

$$-\nabla \times \nabla \times \mathbf{E}(\mathbf{r}) + k_0^2 \varepsilon(\mathbf{r}) \mathbf{E}(\mathbf{r}) = -i\omega \mu_0 \mathbf{J}_s(\mathbf{r}), \quad (2.20)$$

$$-\nabla \times \frac{1}{\varepsilon(\mathbf{r})} \nabla \times \mathbf{H}(\mathbf{r}) + k_0^2 \mathbf{H} = -\nabla \times \left(\frac{\mathbf{J}_s(\mathbf{r})}{\varepsilon(\mathbf{r})} \right), \quad (2.21)$$

where $k_0 = \omega/c$ is the free space wave vector and $c = 1/\sqrt{\mu_0 \varepsilon_0}$ is the speed of light in vacuum. The wave equations can be simplified to be of the form of the Helmholtz equation. In order to do so two assumptions are made. The first assumption is that the source current density is zero, and the second is that the dielectric constant does not depend on position, i.e. $\varepsilon(\mathbf{r}) = \varepsilon$. This results in the divergence of electric field to be zero which can be seen by

$$\nabla \cdot \mathbf{E}(\mathbf{r}) = \frac{\rho_s(\mathbf{r})}{\varepsilon_0 \varepsilon} = \frac{1}{i\omega \varepsilon_0 \varepsilon} \nabla \cdot \mathbf{J}_s(\mathbf{r}) = 0. \quad (2.22)$$

Applying $\nabla \times \nabla \times = \nabla \nabla \cdot - \nabla^2$, equations (2.20) and (2.21) simplifies to

$$(\nabla^2 + k_0^2 \varepsilon) \mathbf{E}(\mathbf{r}) = 0, \quad \text{and} \quad (\nabla^2 + k_0^2 \varepsilon) \mathbf{H}(\mathbf{r}) = 0. \quad (2.23)$$

2.1.2 Poynting Vector

The Poynting vector is defined as

$$\mathbf{S}(\mathbf{r}, t) = \mathbf{E}(\mathbf{r}, t) \times \mathbf{H}(\mathbf{r}, t) \quad (2.24)$$

which represents the energy flux density. Keep in mind that the fields oscillate, thus it is often convenient to consider the time average Poynting vector given by

$$\langle \mathbf{S}(\mathbf{r}, t) \rangle = \frac{1}{T} \int_{t=0}^T \mathbf{S}(\mathbf{r}, t) dt, \quad (2.25)$$

where T is the period of the electromagnetic wave. A more useful equation for the time average Poynting vector can be found if the electric and magnetic field is re-written. The electric field for a monochromatic light source can be expressed as

$$\mathbf{E}(\mathbf{r}, t) = \text{Real}\{\mathbf{E}(\mathbf{r}, \omega) e^{-i\omega t}\} = \frac{1}{2} (\mathbf{E}(\mathbf{r}, \omega) e^{-i\omega t} + (\mathbf{E}(\mathbf{r}, \omega))^* e^{-i\omega t}). \quad (2.26)$$

Using this notation, the time average Poynting can be re-written to

$$\langle \mathbf{S}(\mathbf{r}, t) \rangle = \frac{1}{2} \text{Real}\{\mathbf{E}(\mathbf{r}, \omega) \times (\mathbf{H}(\mathbf{r}, \omega))^*\}, \quad (2.27)$$

where it has been used that the period is $T = 2\pi/\omega$. For the most part the time average Poynting vector is for monochromatic fields will be used. The Poynting vector is the energy flux density, the power, e.g. from the light scattered on a scatterer, can be found as

$$P(t) = \oiint_{\delta\Omega} \mathbf{S}(\mathbf{r}, t) \cdot \hat{\mathbf{n}} dS. \quad (2.28)$$

2.2 Surface Plasmons Polaritons

Metals have many interesting properties, one such property is the ability to sustain surface or volume oscillations at distinct wavelengths. These oscillations consists of free conduction electrons and can be viewed as oscillations of electron plasma. Just as photons are a quanta of electromagnetic oscillations, a quanta of plasma oscillations is called a plasmon.

For the purposes of this report the main subject of discussion will be surface plasmon polaritons (SPPs). In general these SPPs should be seen as homogeneous solutions to Maxwell's equations, i.e. a solution that can exist without external excitation, and is bound to an interface between a metal and a dielectric. In order for the photon to be bound at an interface the fields needs to decay exponentially away from the interface. In general these are particular solutions and not all photons can excite a SPP. To have a better understanding of which photons can excite a SPP a dispersion relation is derived.

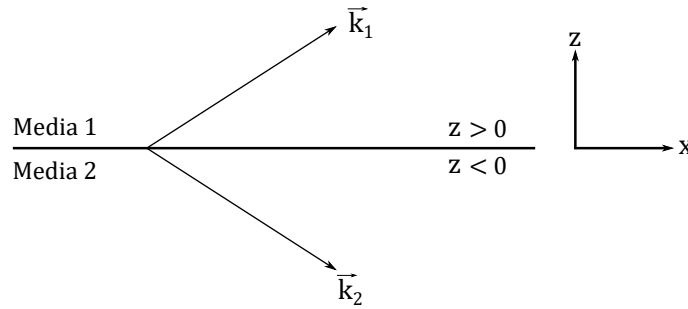


Figure 2.1. Here the theoretical case of a two layered system is shown, for different media with corresponding wavevectors.

2.2.1 Derivation of the Dispersion Relation for SPPs

Assuming a two layered system, an example of such a system is shown in figure 2.1, where a p -polarized wave is propagating in the x -direction on an interface between air (ϵ_1) and some metal (ϵ_2), which is located at $z = 0$. It is enough to consider only p -polarized waves as no s -polarized wave can excite a surface-bound mode [6][11]. The wave in both air and metal will be on the form:

$$z > 0 : \quad \mathbf{H}_1 = (0, H_{y,1}, 0) e^{i(k_{x,1}x + k_{z,1}z - \omega t)}, \quad (2.29)$$

$$\mathbf{E}_1 = (E_{x,1}, 0, E_{z,1}) e^{i(k_{x,1}x + k_{z,1}z - \omega t)}, \quad (2.30)$$

$$z < 0 : \quad \mathbf{H}_2 = (0, H_{y,2}, 0) e^{i(k_{x,2}x - k_{z,2}z - \omega t)}, \quad (2.31)$$

$$\mathbf{E}_2 = (E_{x,2}, 0, E_{z,2}) e^{i(k_{x,2}x - k_{z,2}z - \omega t)}. \quad (2.32)$$

From the continuity relations derived from Maxwell's equations it is found that $k_x = k_{x,1} = k_{x,2}$. Applying the Maxwell equation, $\nabla \times \mathbf{H}_i = \epsilon_i \frac{1}{c} \frac{\partial \mathbf{E}_i}{\partial t}$ [13], to the relevant electric and magnetic fields yields

$$\frac{\partial H_{y,i}}{\partial z} = -i\epsilon_i E_{x,i} \frac{\omega}{c} \quad \Rightarrow \quad k_{z,i} H_{y,i} = \pm \frac{\omega}{c} \epsilon_i E_{x,i}, \quad (2.33)$$

where $i \in \{1, 2\}$ represents if it is for air or metal respectively, and \pm is (+) when $i = 2$ and (-) when $i = 1$. The continuity relations show that $E_{x,1} = E_{x,2}$ and $H_{y,1} = H_{y,2}$, which can be applied to Eq. (2.33) in order to get

$$\frac{k_{z,1}}{\varepsilon_1} + \frac{k_{z,2}}{\varepsilon_2} = 0. \quad (2.34)$$

This is the dispersion relation for the relevant SPPs for the discussed system. A relation for k_x can be found by taking the rotor on one of the Maxwell's equations, $\nabla \times \mathbf{H}_i = \varepsilon_i \frac{1}{c} \frac{\partial \mathbf{E}_i}{\partial t}$ or $\nabla \times \mathbf{E}_i = \frac{1}{c} \frac{\partial \mathbf{H}_i}{\partial t}$ [13]. Then by applying equation (2.33) it can be found that

$$k_x^2 + k_{z,i}^2 = \frac{\omega^2}{c^2} \varepsilon_i \quad \Rightarrow \quad k_{z,i} = \sqrt{\frac{\omega^2}{c^2} \varepsilon_i - k_x^2}. \quad (2.35)$$

Inserting equation (2.35) into (2.34) yields

$$k_x^2 \left(\frac{1}{\varepsilon_1^2} - \frac{1}{\varepsilon_2^2} \right) = \frac{\omega^2}{c^2} \left(\frac{1}{\varepsilon_1} - \frac{1}{\varepsilon_2} \right) \quad \Rightarrow \quad k_x = \frac{\omega}{c} \sqrt{\frac{\varepsilon_1 \varepsilon_2}{\varepsilon_1 + \varepsilon_2}}. \quad (2.36)$$

This is the SPP dispersion relation and it describes the relation between the surface wavevector in the direction of propagation and the angular frequency of the wave.

2.2.2 Surface Plasmon Polariton Properties

Considering a surface plasmon polariton at the interface between air and metal as previous, however, loss is now considered for the metal, meaning its dielectric function becomes complex, i.e. $\varepsilon_2 = \varepsilon'_2 + i\varepsilon''_2$. Losses are assumed to be negligible for air. This results in k_x becoming a complex number, i.e. $k_x = k'_x + ik''_x$. Examining a standard electric wave, $\mathbf{E} = \hat{\mathbf{x}}E_x e^{ik_x x}$, it becomes clear that the real part of k_x determines the frequency of the SPP and the imaginary part determines the rate at which the SPP is damped due to the aforementioned loss. The wavelength of the SPP can be calculated by using that $\lambda_{SPP} = 2\pi/k'_x$, and k'_x can be found by using equation (2.36) and, under the assumption that $|\varepsilon''_2| \ll |\varepsilon'_2|$, is found to be

$$k'_x \simeq \frac{\omega}{c} \sqrt{\frac{\varepsilon'_2 \varepsilon_1}{\varepsilon'_2 + \varepsilon_1}}. \quad (2.37)$$

This results in a SPP wavelength of

$$\lambda_{SPP} \simeq \lambda \sqrt{\frac{\varepsilon'_2 + \varepsilon_1}{\varepsilon'_2 \varepsilon_1}}, \quad (2.38)$$

where λ is the vacuum wavelength.

From the imaginary part of k_x the propagation length can also be calculated, since k''_x results in the decay in the x -direction. So the 1/e decay length in the direction of the interface can be found as $1/k''_x$ and for the intensity it can be found as $1/(2k''_x)$ [11]. Following the same assumptions as in equation (2.37), k''_x can be found as

$$k''_x \simeq \frac{\omega}{c} \sqrt{\frac{\varepsilon'_2 \varepsilon_1}{\varepsilon'_2 + \varepsilon_1}} \frac{\varepsilon''_2 \varepsilon_1}{2\varepsilon'_2(\varepsilon'_2 + \varepsilon_1)}. \quad (2.39)$$

In this report in general two specific incident wavelengths are used, 390 nm and 780 nm. For a silver surface these wavelengths result in the dielectric function becoming $-3.87 + 0.20i$ and $-29.30 + 0.36i$, which results in 1/e intensity decay lengths of 3.01 μm and 278.72 μm , respectively.

Excitation

As is evident from equation (2.36), the wavevector, k_x , is always smaller than the wavevector of the incident light from free space. In Fig. 2.2, it is shown how this results in the plasmon dispersion curve always being to the right of the light-line for free space light, which is the left most striped line. This makes it more difficult to excite plasmons, as the incident light needs to have a larger wavevector than its free space counterpart in order to work. There are several methods of increasing the wavevector component of the incident light, one way would be by the use of evanescent waves, by placing a material with refractive index $n > 1$ between a medium and air. This shifts the light-line with a factor of n , such that $\omega = ck/n$ consists of larger k_x . This effect is also shown in Fig. 2.2, by the rightmost striped line in the leftmost plot.

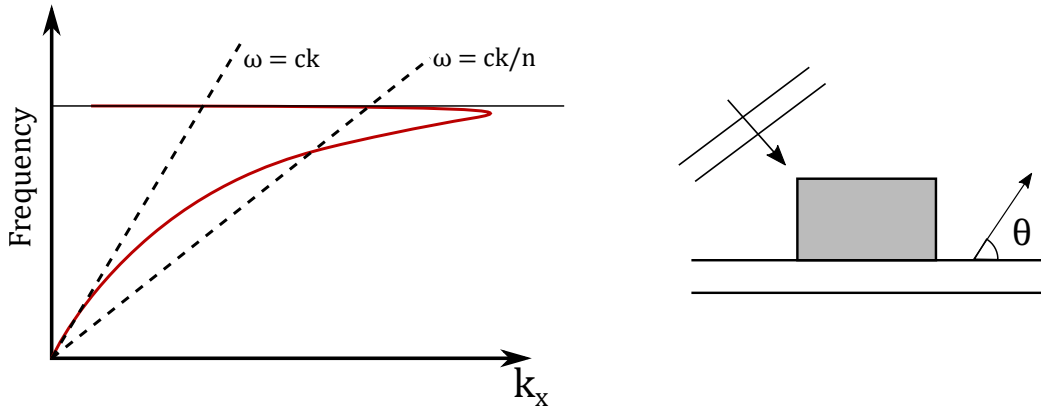


Figure 2.2. The left figure shows the plasmon dispersion curve with two light lines, one from air and another from a material with a higher refractive index, n . The right picture shows the angle notation used when describing far fields.

The scenario that is examined in this report is a nanofiber placed on a silver interface in order to excite SPPs. However, in order to test how well a given nanofiber excites SPPs one need to be able to observe how many plasmons are excited. The way this is done in this report, is by observing the amount of plasmons that have leaked out of the air-silver interface. The trick is that one can calculate at what very specific angles the SPPs will leak of out the interface from into a substrate. These can be found by using the fact that k_x is the x -component of k_0 , i.e. $k_0 = k_x n \cos(\theta)$, and that it must follow the dispersion relation for plasmons, equation (2.37). In total this yields

$$n \cos(\theta) = \text{Real} \left(\sqrt{\frac{\varepsilon_2 \varepsilon_1}{\varepsilon_2 + \varepsilon_1}} \right), \quad (2.40)$$

where n is the refractive index for the material that the plasmons are leaking into and θ is the leakage angle. If one tries to solve this equation using the refractive index for silver, one will find no real solutions for θ , meaning that the plasmons are bound to the interface. However, if one uses e.g. glass with a refractive index of 1.5, solutions are found. So in order to observe the amount of bound plasmons the silver layer is changed to a thin silver film placed on a glass layer.

If the angle is defined as given in the right figure of figure 2.2, negative angles are given when the angles turns in the clockwise direction. Then for the 390 nm incident wave the

leakage angles, θ , are found to be -39.26° and -140.74° . Furthermore, for the 780 nm wavelength these angles are found to be -47.29° and -132.71° . Since these modes have a higher k_x than what is possible by simply shining light on the surface, the leakage radiation will leak at a larger angle than the critical angle of the air-glass interface. The critical angles of the air-glass interface is, by the given notation, -48.2° and $-131,8^\circ$, which means that the leakage angles for both incident wavelengths are beyond the critical angles.

Chapter 3

Scattering Problem in Two Dimensions

This chapter seeks to derive the Green's function and tensor for s - and p -polarized light that is incident on a scatterer. The examined case is depicted in figure 3.1. Different subjects will be covered such as defining and using a reference structure, constructing a dyadic Green's tensor and separating it into a direct and indirect part, and then constructing the far fields. Lastly, the far field will be used to calculate different optical cross sections.

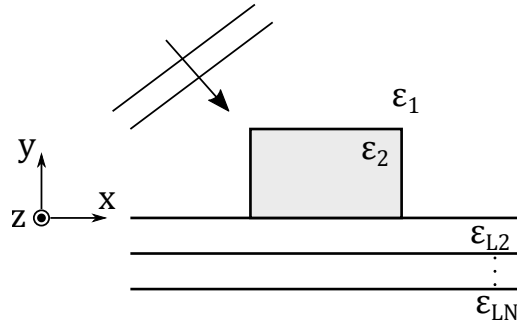


Figure 3.1. Illustration of a scatterer placed on top of a layered dielectric structure.

The fundamental mechanic that is considered is that the scattering of light inside of the scatterer is a coupled system, since when different parts of the scatterer gets polarized they emit radiation that affects all other parts of the scatterer. Thus the field scattered at a point inside of the scatterer is a sum of the incident field and the scattered field from all positions inside the fiber.

3.1 Green's Function Area Integral Equation

When finding the electric field, the central equation that is considered is the wave equation (2.20),

$$-\nabla \times \nabla \times \mathbf{E}(\mathbf{r}) + k_0^2 \epsilon(\mathbf{r}) \mathbf{E}(\mathbf{r}) = -i\omega\mu_0 \mathbf{J}_s(\mathbf{r}),$$

where it is assumed that the electric field and the current density only vary in the xy -plane, i.e., $\mathbf{r} = \hat{\mathbf{x}}x + \hat{\mathbf{y}}y$. This means that the electric field and the current density are invariant in the z -direction.

3.1.1 Calculations for s -polarization

For an electric field that is s -polarized, the electric field is pointing along the z -axis, thus

$$\mathbf{E}(\mathbf{r}) = \hat{\mathbf{z}}E(\mathbf{r}), \quad (3.1)$$

$$\mathbf{J}_s(\mathbf{r}) = \hat{\mathbf{z}}J_s(\mathbf{r}). \quad (3.2)$$

This in turn simplifies the wave equation, since

$$\nabla \cdot \mathbf{E}(\mathbf{r}) = \frac{\partial E(\mathbf{r})}{\partial z} = 0, \quad (3.3)$$

thus when considering the operator $\nabla \times \nabla \times = -\nabla \nabla \cdot + \nabla^2$, only the Laplace operator, ∇^2 , is left. The wave equation for the electric field then simplifies to the scalar Helmholtz equation,

$$(\nabla^2 + k_0^2 \varepsilon(\mathbf{r})) E(\mathbf{r}) = -i\omega\mu_0 J_s(\mathbf{r}). \quad (3.4)$$

A Green's function can then be found to solve the following equation:

$$(\nabla^2 + k_0^2 \varepsilon(\mathbf{r})) g(\mathbf{r}, \mathbf{r}') = -\delta(\mathbf{r} - \mathbf{r}'). \quad (3.5)$$

where \mathbf{r} is the observation point and \mathbf{r}' is the source of the field. A solution to equation (3.4) can now be found in terms of the Green's function as

$$E(\mathbf{r}) = i\omega\mu_0 \int g(\mathbf{r}, \mathbf{r}') J_s(\mathbf{r}') d^2 r'. \quad (3.6)$$

Now, the structure without the scatterer is considered. This structure is termed the reference geometry. Let $\varepsilon_{\text{ref}}(\mathbf{r})$ be the dielectric function for the reference geometry, and consider the Helmholtz equation

$$(\nabla^2 + k_0^2 \varepsilon_{\text{ref}}(\mathbf{r})) E_0(\mathbf{r}) = -i\omega\mu_0 J_s(\mathbf{r}), \quad (3.7)$$

where the electric field $E_0(\mathbf{r})$ is the field generated by the same current density $J_s(\mathbf{r})$ as before, however, only in the reference geometry. Using the reference dielectric function, equation (3.4) can be re-written to

$$(\nabla^2 + k_0^2 \varepsilon_{\text{ref}}(\mathbf{r})) E(\mathbf{r}) = -k_0^2 (\varepsilon(\mathbf{r}) - \varepsilon_{\text{ref}}(\mathbf{r})) E(\mathbf{r}) - i\omega\mu_0 J_s(\mathbf{r}). \quad (3.8)$$

Subtracting equation (3.7) from (3.8) removes $i\omega\mu_0 J_s(\mathbf{r})$ as a driving term, this leaves

$$(\nabla^2 + k_0^2 \varepsilon_{\text{ref}}(\mathbf{r})) (E(\mathbf{r}) - E_0(\mathbf{r})) = -k_0^2 (\varepsilon(\mathbf{r}) - \varepsilon_{\text{ref}}(\mathbf{r})) E(\mathbf{r}). \quad (3.9)$$

A solution to equation (3.9) can then be found by

$$E(\mathbf{r}) = E_0(\mathbf{r}) + \int g(\mathbf{r}, \mathbf{r}') k_0^2 (\varepsilon(\mathbf{r}') - \varepsilon_{\text{ref}}(\mathbf{r}')) E(\mathbf{r}') d^2 r', \quad (3.10)$$

where $g(\mathbf{r}, \mathbf{r}')$ now need to satisfy equation (3.5), but for the reference geometry. Since $\varepsilon(\mathbf{r}') - \varepsilon_{\text{ref}}(\mathbf{r}')$ is only nonzero when inside the scatterer, one only needs to evaluate the integral at coordinates inside the scatterer.

3.1.2 Calculations for p -polarization

In the case of p -polarized fields, the electric field is polarized in the xy -plane, and is still invariant in the z -direction. This means that the electric field and the current density can be written as

$$\mathbf{E}(\mathbf{r}) = \hat{\mathbf{x}}E_x(\mathbf{r}) + \hat{\mathbf{y}}E_y(\mathbf{r}), \quad (3.11)$$

$$\mathbf{J}_s(\mathbf{r}) = \hat{\mathbf{x}}J_{x,s}(\mathbf{r}) + \hat{\mathbf{y}}J_{y,s}(\mathbf{r}). \quad (3.12)$$

The electric wave equation can thus not be simplified to the Helmholtz equation, therefore the starting point becomes equation (2.20). A solution can be constructed using a dyadic Green's tensor which needs to be a solution to

$$(-\nabla\nabla \cdot + \nabla^2 + k_0^2\varepsilon(\mathbf{r})) \overleftrightarrow{\mathbf{G}}(\mathbf{r}, \mathbf{r}') = -\overleftrightarrow{\mathbf{I}}\delta(\mathbf{r} - \mathbf{r}'). \quad (3.13)$$

Just as before, the same wave equation can be used for the reference structure defined by the reference dielectric function, $\varepsilon_{\text{ref}}(\mathbf{r})$, in which the reference field, \mathbf{E}_0 , is generated by the same current density. The field can then be found by evaluating the integral

$$\mathbf{E}_0(\mathbf{r}) = i\omega\mu_0 \int \overleftrightarrow{\mathbf{G}}(\mathbf{r}, \mathbf{r}') \cdot \mathbf{J}_s(\mathbf{r}') d^2r', \quad (3.14)$$

which solves

$$(-\nabla\nabla \cdot + \nabla^2 + k_0^2\varepsilon_{\text{ref}}(\mathbf{r})) \mathbf{E}_0(\mathbf{r}) = -i\omega\mu_0\mathbf{J}_s(\mathbf{r}). \quad (3.15)$$

The same method as before of subtracting the two wave equations, one for the reference structure and one for the whole structure, can be applied to yield a combined wave equation

$$(-\nabla\nabla \cdot + \nabla^2 + k_0^2\varepsilon_{\text{ref}}(\mathbf{r})) (\mathbf{E}(\mathbf{r}) - \mathbf{E}_0(\mathbf{r})) = -k_0^2(\varepsilon(\mathbf{r}) - \varepsilon_{\text{ref}}(\mathbf{r}))\mathbf{E}(\mathbf{r}). \quad (3.16)$$

This results in the Green's function area integral equation for p -polarization, which has a form similar to the s -polarization case,

$$\mathbf{E}(\mathbf{r}) = \mathbf{E}_0(\mathbf{r}) + \int \overleftrightarrow{\mathbf{G}}(\mathbf{r}, \mathbf{r}') k_0^2 \cdot (\varepsilon(\mathbf{r}') - \varepsilon_{\text{ref}}(\mathbf{r}')) \mathbf{E}(\mathbf{r}') d^2r', \quad (3.17)$$

here $\overleftrightarrow{\mathbf{G}}(\mathbf{r}, \mathbf{r}')$ needs to solve equation (3.13), but for the reference geometry.

3.2 Scatterer on a Layered Structure

Before the electric field is found, in the case where a scatterer is placed on top of a layered structure, it is needed to separate the working parts of the Green's function and Green's tensor. In the upper half plane of the structure, where $y, y' > 0$, the Green's function and tensor can be separated into two terms, the direct part and the indirect part, this is indexed with a (d) and (i) respectively, which for the Green's function is shown in figure 3.2. The direct part represents the direct scattering effect in the scatterer, while the indirect part represents the the scattered field that gets reflected back into the scatterer. Since the scatterer scatters the field in a continuous array of plane waves with different k_x , a plane wave expansion for the direct Green's function and tensor can be derived.

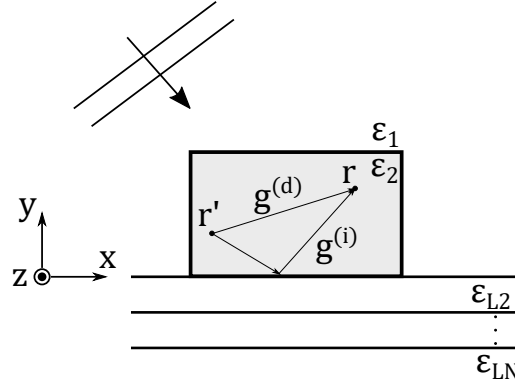


Figure 3.2. Illustration of the direct and indirect Green's function from a source point to an observation point inside of a scatterer.

3.2.1 Plane Wave Expansion of the Green's Function

In the upper half plane, where $\varepsilon_{\text{ref}} = \varepsilon_1$, the Helmholtz equation for the Green's function becomes

$$(\nabla^2 + k_0^2 \varepsilon_1(\mathbf{r})) g(\mathbf{r}, \mathbf{r}') = -\delta(\mathbf{r} - \mathbf{r}').$$

A particular solution to this equation can be found as [14]

$$g^{(d)}(\mathbf{r}, \mathbf{r}') = \frac{i}{4} H_0^{(1)}(k_0 n_1 |\mathbf{r} - \mathbf{r}'|), \quad (3.18)$$

where $n_1 = \sqrt{\varepsilon_1}$ and $H_0^{(1)}$ is a Hankel function of first kind and of 0'th order. Next a plane wave expansion of the direct Green's function will be derived. This is done by the use of the eigenvalue expansion method [15]. The method starts by considering the left hand operator of equation (3.5), and defining eigenmodes E_λ with eigenvalue λ . The eigenvalue problem becomes

$$(\nabla^2 + k_0^2 \varepsilon_1) E_\lambda(\mathbf{r}) = \lambda E_\lambda(\mathbf{r}), \quad (3.19)$$

which can be re-written as

$$(\nabla^2 + k^2) E_{\mathbf{k}}(\mathbf{r}) = 0, \quad (3.20)$$

where $k^2 = k_0^2 \varepsilon_1 - \lambda_{\mathbf{k}} = \mathbf{k} \cdot \mathbf{k}$. A solution to this differential equation is of the form

$$E_{\mathbf{k}}(\mathbf{r}) = e^{i\mathbf{k} \cdot \mathbf{r}}, \quad (3.21)$$

where $\mathbf{k} = \hat{\mathbf{x}}k_x + \hat{\mathbf{y}}k_y$. These modes are orthogonal modes, thus the normalization factor can be found by the overlap integral,

$$\int E_{\mathbf{k}}(\mathbf{r}) (E_{\mathbf{k}'}(\mathbf{r}))^* d^2r = N_{\mathbf{k}} \delta(\mathbf{k} - \mathbf{k}'), \quad (3.22)$$

where the normalization factor can be found to be $N_{\mathbf{k}} = (2\pi)^2$ by applying the definition of the Dirac delta function. A solution to Eq. (3.5), where $\varepsilon_{\text{ref}}(\mathbf{r}) = \varepsilon_1$, can now be found using eigenmode expansion, i.e. plane wave expansion,

$$g^{(d)}(\mathbf{r}, \mathbf{r}') = - \int \frac{E_{\mathbf{k}}(\mathbf{r}) (E_{\mathbf{k}}(\mathbf{r}'))^*}{N_{\mathbf{k}} \lambda_{\mathbf{k}}} d^2k. \quad (3.23)$$

This can be verified as a solution by inserting it into Eq. (3.5) and then applying the result from equation (3.19), as the operator works on the unmarked term in the integral. The scalar Helmholtz then becomes

$$(\nabla^2 + k_0^2 \varepsilon_1) g^{(d)}(\mathbf{r}, \mathbf{r}') = - \int \frac{E_{\mathbf{k}}(\mathbf{r})(E_{\mathbf{k}}(\mathbf{r}'))^*}{N_{\mathbf{k}}} d^2k. \quad (3.24)$$

Inserting $E_{\mathbf{k}}(\mathbf{r})(E_{\mathbf{k}}(\mathbf{r}'))^* = e^{i\mathbf{k} \cdot (\mathbf{r} - \mathbf{r}')}$ and $N_{\mathbf{k}} = (2\pi)^2$ it can be shown, by using (3.22), that the direct Green's function is a solution.

In order to evaluate the integral of Eq. (3.23) it is used that $dk^2 = dk_x dk_y$. Only the integral over k_y is evaluated, as the integral over k_x is equivalent. However, when evaluating the integral, one must consider the poles found when

$$\lambda_{\mathbf{k}} = k_0^2 \varepsilon_1 - k^2 = \left(\sqrt{k_0^2 \varepsilon_1 - k_x^2} - k_y \right) \left(\sqrt{k_0^2 \varepsilon_1 - k_x^2} + k_y \right) = 0, \quad (3.25)$$

where two poles are found as

$$k_{y,p} = \pm \sqrt{k_0^2 \varepsilon_1 - k_x^2}. \quad (3.26)$$

In order to avoid integrating directly over the poles, a small imaginary part, $i\eta$, is added to the poles, where the poles are given as

$$k_{y,p} = \pm \left(\sqrt{k_0^2 \varepsilon_1 - k_x^2} + i\eta \right). \quad (3.27)$$

This results in a shift of the poles into the imaginary plane. This results in a direct Green's function of the form

$$g^{(d)}(\mathbf{r}, \mathbf{r}') = \lim_{\eta \rightarrow 0^+} \frac{1}{(2\pi)^2} \iint \frac{e^{ik_x(x-x')} e^{ik_y(y-y')}}{\left(k_y - \left(\sqrt{k_0^2 \varepsilon_1 - k_x^2} + i\eta \right) \right) \left(k_y + \left(\sqrt{k_0^2 \varepsilon_1 - k_x^2} + i\eta \right) \right)} dk_y dk_x. \quad (3.28)$$

Due to this small imaginary part, the integral of k_y can now be replaced by a closed line integral in the complex plane depicted in figure 3.3. The idea is to evaluate the integral so that it is still equivalent to integrating over the real axis for k_y , this is done by applying the residue theorem when evaluating the integral.

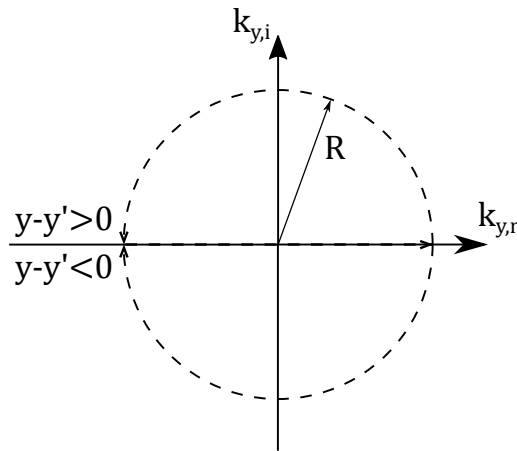


Figure 3.3. Illustration of the poles of the integrand in equation (3.28) as well as the closed integration path that extends the integration over k_y into the complex plane as two half circles, one for each pole.

The two poles of equation (3.27) are illustrated in the figure. One closed line path can be drawn for each pole. Since the integral needs to include the real axis the closed line path is chosen from $-R$ to R on the real axis and a half circle with radius R is chosen for each pole extending into the complex plane. In order to only integrate over $k_{y,\text{real}}$, it is required that the contribution from the exponential function in Eq. (3.28), regarding $k_{y,\text{img}}$, becomes to zero, i.e. $e^{-k_{y,\text{img}}(y-y')} \rightarrow 0$. Taking the limit $R \rightarrow \infty$ extends the integration of the real axis to cover the entire real axis. For the imaginary part the exponential $e^{-k_{y,\text{img}}(y-y')}$ converges either to 0 or ∞ depending of the sign of $k_{y,\text{img}}$ and $(y - y')$. This means that the sign of $k_{y,\text{img}}$ and $(y - y')$ needs to match so that the complex contribution to the integral converges to zero for $R \rightarrow \infty$. The sign needed for $y - y'$ is shown in figure 3.3. Since the complex contribution of k_y converges to zero as $R \rightarrow \infty$ the integral is still only an integral over $k_{y,\text{real}}$.

Since the integral is now a line integral over a closed path in the complex plane it can be solved using residual calculus [12]

$$\oint_C f(z)dz = \pm 2\pi i \sum_{j=1}^n [\text{Res} f(z)]_{z=z_j}, \quad (3.29)$$

where Res stands for residual, which can be calculated as

$$[\text{Res} f(z)]_{z=z_j} = \lim_{z \rightarrow z_j} (z - z_j) f(z), \quad (3.30)$$

and z_j are the poles of the function $f(z)$ and C is the closed integration path. The sign change occur when the integration around the closed path changes direction, if the direction is counterclockwise (+) is used, for clockwise (-) is used.

Let the integrand of equation (3.28) be noted as $f(k_y; k_x)$. Now one can apply the residual theorem to $f(k_y; k_x)$, first note that when evaluating the right side of equation (3.29) only one of the closed paths needs to be considered. Depending of the chose of closed path, either $y - y' < 0$ or $y - y' > 0$, the (\pm) either become a (-) or a (+) in the residual theorem. For completion both paths are considered, thus including both poles. This is indexed by the sign of the pole given from equation (3.27), noted by a (+) or a (-) index. The residual theorem yields,

$$\oint f(k_y) dk_y \Big|_{y-y'=\pm|y-y'|} = \pm 2\pi i \left(\lim_{k_y \rightarrow k_{y,p}^{(\pm)}} (k_y - k_{y,p}^{(\pm)}) f(k_y) \right) \Big|_{y-y'=\pm|y-y'|}. \quad (3.31)$$

Each of the limits will leave the exponentials with a factor of $1/2(\sqrt{k_0^2 \varepsilon_1 - k_x^2} + i\eta)$ since

$$\begin{aligned} & \pm \lim_{k_y \rightarrow k_{y,p}^{(\pm)}} (k_y - k_{y,p}^{(\pm)}) f(k_y) \\ &= \pm \lim_{k_y \rightarrow k_{y,p}^{(\pm)}} (k_y - k_{y,p}^{(\pm)}) \frac{e^{ik_x(x-x')} e^{ik_y(\pm)|y-y'|}}{(k_y - (\sqrt{k_0^2 \varepsilon_1 - k_x^2} + i\eta)) (k_y + (\sqrt{k_0^2 \varepsilon_1 - k_x^2} + i\eta))} \\ &= \frac{e^{ik_x(x-x')} e^{i(\sqrt{k_0^2 \varepsilon_1 - k_x^2} + i\eta)|y-y'|}}{2(\sqrt{k_0^2 \varepsilon_1 - k_x^2} + i\eta)}. \end{aligned} \quad (3.32)$$

Equation (3.32) shows that the residual theorem gives the same result for each of the two poles. After applying the residue theorem, the limit where $\eta \rightarrow 0^+$ is applied. This leads

to the plane wave expanded direct Green's function,

$$g^{(d)}(\mathbf{r}, \mathbf{r}') = \frac{i}{2\pi} \int \frac{e^{ik_x(x-x')} e^{ik_{y,1}|y-y'|}}{2k_{y,1}} dk_x. \quad (3.33)$$

where $k_{y,1} = \sqrt{k_0^2 \varepsilon_1 - k_x^2}$.

3.2.2 Calculations for p -polarization

The Direct Green's Tensor

It has already been established that for p -polarization, the field can be found by using the Green's tensor, this is described in section 3.1.2. Such a direct Green's tensor must satisfy

$$(-\nabla\nabla \cdot + \nabla^2 + k_0 \varepsilon_1) \overleftrightarrow{\mathbf{G}}^{(d)}(\mathbf{r}, \mathbf{r}') = -\overleftrightarrow{\mathbf{I}} \delta(\mathbf{r} - \mathbf{r}'). \quad (3.34)$$

To construct such a Green's tensor one can use the direct Green's function, which satisfies Eq. (3.5) and it can be written as

$$\overleftrightarrow{\mathbf{G}}^{(d)}(\mathbf{r}, \mathbf{r}') = \left(\overleftrightarrow{\mathbf{I}} + \frac{1}{k_1^2} \nabla\nabla \right) g^{(d)}(\mathbf{r}, \mathbf{r}'), \quad (3.35)$$

where $k_1^2 = k_0^2 \varepsilon_1$. This can be shown to satisfy Eq. (3.34),

$$\begin{aligned} & (-\nabla\nabla \cdot + \nabla^2 + k_1^2) \left(\overleftrightarrow{\mathbf{I}} + \frac{1}{k_1^2} \nabla\nabla \right) g^{(d)}(\mathbf{r}, \mathbf{r}') \\ &= \left(-\nabla\nabla \cdot \overleftrightarrow{\mathbf{I}} - \frac{1}{k_1^2} \nabla\nabla \cdot \nabla\nabla + \nabla^2 \overleftrightarrow{\mathbf{I}} + \frac{1}{k_1^2} \nabla^2 \nabla\nabla + k_1^2 \overleftrightarrow{\mathbf{I}} + \nabla\nabla \right) g^{(d)}(\mathbf{r}, \mathbf{r}') \\ &= (\nabla^2 + k_1^2) \overleftrightarrow{\mathbf{I}} g^{(d)}(\mathbf{r}, \mathbf{r}') = -\overleftrightarrow{\mathbf{I}} \delta(\mathbf{r} - \mathbf{r}'). \end{aligned} \quad (3.37)$$

Equation (3.18) and (3.33) are two equally valid expressions to use in Eq. (3.35). If Eq. (3.18) is chosen the direct Green's tensor can be found analytically which is obviously beneficial. The results in

$$\begin{aligned} \overleftrightarrow{\mathbf{G}}^{(d)}(\mathbf{r}, \mathbf{r}') &= \overleftrightarrow{\mathbf{I}} \frac{i}{4} \left(H_0^{(1)}(k_1 R) - H_1^{(1)}(k_1 R) \frac{1}{k_1 R} \right) \\ &\quad - \frac{\mathbf{R}\mathbf{R}}{R^2} \frac{i}{4} \left(\frac{1}{2} \left(H_0^{(1)}(k_1 R) - H_1^{(2)}(k_1 R) \right) - H_1^{(2)}(k_1 R) \frac{1}{k_1 R} \right), \end{aligned} \quad (3.38)$$

where $\mathbf{R} = \mathbf{r} - \mathbf{r}'$ and $R = |\mathbf{R}|$. This is done by applying the calculus identity: $\nabla\nabla = \hat{\mathbf{x}}\hat{\mathbf{x}} \frac{\partial^2}{\partial x^2} + \hat{\mathbf{y}}\hat{\mathbf{y}} \frac{\partial^2}{\partial y^2} + \hat{\mathbf{x}}\hat{\mathbf{y}} \frac{\partial^2}{\partial xy} + \hat{\mathbf{y}}\hat{\mathbf{x}} \frac{\partial^2}{\partial xy}$ and the identity regarding differentiating a n 'th order Hankel function of the first kind which is [16]

$$\frac{\partial}{\partial z} H_m^{(1)}(z) = \frac{m H_m^{(1)}(z)}{z} - H_{m+1}^{(1)}(z). \quad (3.39)$$

The Indirect Green's Tensor

In order to find an equation for the indirect Green's tensor, the plane wave expansion can be used. This is done by constructing the direct Green's tensor by using equation (3.35)

and (3.33). Doing so yields

$$\begin{aligned}\overleftarrow{\mathbf{G}}^{(d)}(\mathbf{r}, \mathbf{r}') &= \left(\overleftarrow{\mathbf{I}} + \frac{1}{k_1} \nabla \nabla \right) \frac{i}{4\pi} \int \frac{e^{ik_x(x-x')} e^{ik_{y,1}|y-y'|}}{k_{y,1}} dk_x \\ &= \frac{i}{4\pi} \int \left(\hat{\mathbf{x}}\hat{\mathbf{x}} + \hat{\mathbf{y}}\hat{\mathbf{y}} - \hat{\mathbf{x}}\hat{\mathbf{x}} \frac{k_x^2}{k_1^2} - \hat{\mathbf{y}}\hat{\mathbf{y}} \frac{k_{y,1}^2}{k_1^2} - (\hat{\mathbf{x}}\hat{\mathbf{y}} + \hat{\mathbf{y}}\hat{\mathbf{x}}) \frac{k_x k_{y,1}}{k_1^2} \frac{y-y'}{|y-y'|} \right) \\ &\quad \times \frac{e^{ik_x(x-x')} e^{ik_{y,1}|y-y'|}}{k_{y,1}} dk_x.\end{aligned}\quad (3.40)$$

Using that $k_{y,1}^2 = k_1^2 - k_x^2$, the integrand can be simplified to

$$\overleftarrow{\mathbf{G}}^{(d)}(\mathbf{r}, \mathbf{r}') = \frac{i}{4\pi} \int \left(\hat{\mathbf{x}}\hat{\mathbf{x}} \frac{k_{y,1}^2}{k_1^2} + \hat{\mathbf{y}}\hat{\mathbf{y}} \frac{k_x^2}{k_1^2} - (\hat{\mathbf{x}}\hat{\mathbf{y}} + \hat{\mathbf{y}}\hat{\mathbf{x}}) \frac{k_x k_{y,1}}{k_1^2} \frac{y-y'}{|y-y'|} \right) \frac{e^{ik_x(x-x')} e^{ik_{y,1}|y-y'|}}{k_{y,1}} dk_x.\quad (3.41)$$

In order to proceed, instead of a layered reference structure, consider one where there is only one interface such that

$$\varepsilon_{\text{ref}}(\mathbf{r}) = \begin{cases} \varepsilon_1, & y > 0 \\ \varepsilon_{L2}, & y < 0 \end{cases}.\quad (3.42)$$

The indirect Green's tensor can now be found by using the direct Green's tensor. This is done by finding the incoming electric fields and applying reflection from the interface. Consider the incident field on the interface as

$$\begin{aligned}\mathbf{E}_{i,x}(\mathbf{r}) &= \overleftarrow{\mathbf{G}}^{(d)}(\mathbf{r}, \mathbf{r}') \cdot \hat{\mathbf{x}} \\ &= \frac{i}{4\pi} \int \left(\hat{\mathbf{x}} \frac{k_{y,1}^2}{k_1^2} - \hat{\mathbf{y}} \frac{k_x k_{y,1}}{k_1^2} \frac{y-y'}{|y-y'|} \right) \frac{e^{ik_x(x-x')} e^{ik_{y,1}|y-y'|}}{k_{y,1}} dk_x,\end{aligned}\quad (3.43)$$

in which the incident field is $\mathbf{E}_i(\mathbf{r}) = \mathbf{E}_{i,x}(\mathbf{r}) + \mathbf{E}_{i,y}(\mathbf{r})$, and $\mathbf{E}_{i,y}$ is found by taking the y -component of the direct Green's tensor. If the field is found at the interface then $0 < y < y'$, thus the wave propagates towards the interface. This means that

$$\frac{y-y'}{|y-y'|} = -1.\quad (3.44)$$

The plane wave expansion expands the incoming wave into a continuum of plane waves by k_x . It is then possible to define a reflection coefficient function, as this is a function of k_x , which can be multiplied to the integrand to ensure that different plane waves are reflected appropriately. When the field is reflected off the surface the x -component of the field changes sign, and $y-y'$ becomes the collective distance $y+y'$ since the fields needs to travel to the interface and then change direction upwards to the observation point. The reflected field is then

$$\mathbf{E}_{r,x}(\mathbf{r}) = \frac{i}{2\pi} \int r^{(p)}(k_x) \left(-\hat{\mathbf{x}} \frac{k_{y,1}^2}{k_1^2} + \hat{\mathbf{y}} \frac{k_x k_{y,1}}{k_1^2} \right) \frac{e^{ik_x(x-x')} e^{ik_{y,1}(y+y')}}{k_{y,1}} dk_x.\quad (3.45)$$

This can be done equivalently for $\mathbf{E}_{r,y}$. The indirect Green's tensor can now be found by multiplying $\hat{\mathbf{x}}$ and $\hat{\mathbf{y}}$ on $\mathbf{E}_{r,x}$ and $\mathbf{E}_{r,y}$ respectively. By doing so yields

$$\begin{aligned} \overleftrightarrow{\mathbf{G}}^{(i)}(\mathbf{r}, \mathbf{r}') &= \frac{i}{4\pi} \int r^{(p)}(k_x) \left(-\hat{\mathbf{x}}\hat{\mathbf{x}} \frac{k_{y,1}^2}{k_1^2} + \hat{\mathbf{y}}\hat{\mathbf{y}} \frac{k_x^2}{k_1^2} + (\hat{\mathbf{y}}\hat{\mathbf{x}} - \hat{\mathbf{x}}\hat{\mathbf{y}}) \frac{k_x k_{y,1}}{k_1^2} \right) \\ &\quad \times \frac{e^{ik_x(x-x')} e^{ik_{y,1}(y+y')}}{k_{y,1}} dk_x. \end{aligned} \quad (3.46)$$

In order to find the reflection coefficient it is needed to construct the transmitted field and then apply boundary conditions at the interface. Finding the transmitted field is straight forward as it can be found by using the incoming field as before. The transmitted field concerning an incident field given by equation (3.43) is

$$\mathbf{E}_{t,x}(\mathbf{r}) = \frac{i}{4\pi} \int t^{(p)}(k_x) \frac{\varepsilon_1}{\varepsilon_{L2}} \left(\hat{\mathbf{x}} \frac{k_{y,1} k_{y,L2}}{k_1^2} + \hat{\mathbf{y}} \frac{k_x k_{y,1}}{k_1^2} \right) \frac{e^{ik_x(x-x')} e^{ik_{y,1}y'} e^{-ik_{y,L2}y}}{k_{y,1}} dk_x, \quad (3.47)$$

where $t^{(p)}(k_x)$ is the transmission coefficient, and is related to the reflection coefficient by

$$1 + r^{(p)}(k_x) = t^{(p)}(k_x). \quad (3.48)$$

The boundary condition stated in equation (A.7) can be used to derive an expression for the reflection coefficient. In this case the tangential component is in direction of $\hat{\mathbf{x}}$, thus

$$\mathbf{E}_{t,x} \cdot \hat{\mathbf{x}} = \mathbf{E}_{i,x} \cdot \hat{\mathbf{x}} - \mathbf{E}_{r,x} \cdot \hat{\mathbf{x}}, \quad \text{for } y = 0. \quad (3.49)$$

This results in

$$\frac{k_{y,1}^2}{k_1^2} (1 - r^{(p)}(k_x)) = t^{(p)}(k_x) \frac{\varepsilon_1}{\varepsilon_{L2}} \frac{k_{y,1} k_{y,L2}}{k_1^2}, \quad (3.50)$$

which can be rearranged to yield

$$r^{(p)}(k_x) = \frac{k_{y,1}\varepsilon_{L2} - k_{y,L2}\varepsilon_1}{k_{y,1}\varepsilon_{L2} + k_{y,L2}\varepsilon_1}. \quad (3.51)$$

3.3 Green's Function Area Integral Equation in the Far Field

The far fields gives a visual representation of how a field is scattered by a scatterer. This section aim to rigid and simple equation for calculating the far field. As before, the case is considered for p -polarized light. One can find the electric far field, by applying a so called far field Green's tensor, found by

$$\mathbf{E}^{(\text{ff})}(\mathbf{r}) = \mathbf{E}_0(\mathbf{r}) + \int \overleftrightarrow{\mathbf{G}}^{(\text{ff})}(\mathbf{r}, \mathbf{r}') k_0^2 \cdot (\varepsilon(\mathbf{r}') - \varepsilon_{\text{ref}}(\mathbf{r}')) \mathbf{E}(\mathbf{r}') d^2 r', \quad (3.52)$$

where

$$\overleftrightarrow{\mathbf{G}}^{(\text{ff})}(\mathbf{r}, \mathbf{r}') = \overleftrightarrow{\mathbf{G}}^{(\text{ff},d)}(\mathbf{r}, \mathbf{r}') + \overleftrightarrow{\mathbf{G}}^{(\text{ff},i)}(\mathbf{r}, \mathbf{r}'). \quad (3.53)$$

The direct Green's tensor is given by equation (3.38), thus a far field expression of the Hankel function is needed in order to find $\overleftrightarrow{\mathbf{G}}^{(\text{ff},d)}$. A Hankel function of the first and second kind consists of a Bessel J and a Bessel Y function, and can thus be written on the form

$$H_m^{(1)}(x) \equiv J_m(x) + iY_m(x), \quad \text{and} \quad H_m^{(2)}(x) \equiv J_m(x) - iY_m(x). \quad (3.54)$$

The Bessel functions can be approximated for large x as [16][17]

$$J_m(x) \approx \sqrt{\frac{2}{\pi x}} \cos\left(x - \frac{m\pi}{2} - \frac{\pi}{4}\right), \quad \text{for } x \gg 1 \quad \text{and} \quad (3.55)$$

$$Y_m(x) \approx \sqrt{\frac{2}{\pi x}} \sin\left(x - \frac{m\pi}{2} - \frac{\pi}{4}\right), \quad \text{for } x \gg 1. \quad (3.56)$$

If one uses these approximations and $x = k_1|\mathbf{r} - \mathbf{r}'|$, then the Hankel function can be written as

$$H_0^{(1)}(k_1|\mathbf{r} - \mathbf{r}'|) \approx \sqrt{\frac{2}{\pi k_0 n_1 r}} e^{-i\pi/4} e^{ik_0 n_1 r} e^{ik_0 n_1 \hat{\mathbf{r}} \cdot \mathbf{r}'}, \quad (3.57)$$

where it has been used that $|\mathbf{r} - \mathbf{r}'| \approx r - \hat{\mathbf{r}} \cdot \mathbf{r}'$. Then the direct Green's tensor can be found for the far field as

$$\overleftrightarrow{\mathbf{G}}^{(\text{ff},d)}(\mathbf{r}, \mathbf{r}') = \left(\overleftrightarrow{\mathbf{I}} + \frac{1}{(k_0 n_1)^2} \nabla \nabla \right) \frac{i}{4} \sqrt{\frac{2}{\pi k_0 n_1 r}} e^{-i\pi/4} e^{ik_0 n_1 r} e^{ik_0 n_1 \hat{\mathbf{r}} \cdot \mathbf{r}'}. \quad (3.58)$$

Applying the dyadic operator $\nabla \nabla$ results in terms that scale as $1/r$ or of higher order, which can be ignored in the far field. After, only one term is left which originates from the $\hat{\mathbf{r}} \hat{\mathbf{r}} \frac{\partial^2}{\partial r^2}$ -term from the operator. Since $\overleftrightarrow{\mathbf{I}} = \hat{\mathbf{r}} \hat{\mathbf{r}} + \hat{\boldsymbol{\theta}} \hat{\boldsymbol{\theta}}$, the direct Greens tensor for the far field becomes

$$\overleftrightarrow{\mathbf{G}}^{(\text{ff},d)}(\mathbf{r}, \mathbf{r}') = \hat{\boldsymbol{\theta}} \hat{\boldsymbol{\theta}} \frac{1}{4} \sqrt{\frac{2}{\pi k_0 n_1 r}} e^{i\pi/4} e^{ik_0 n_1 r} e^{ik_0 n_1 \hat{\mathbf{r}} \cdot \mathbf{r}'}, \quad (3.59)$$

where it has been used that $i\sqrt{-i} = \sqrt{i} = e^{i\pi/4}$.

The next step is to find the far field indirect Green's tensor, so far it is of the form of equation (3.46). An alternative expression of this equation can be found by re-writing the direct Green's function (3.33) and conduct a new derivation, this results in

$$g^{(d)}(\mathbf{r}, \mathbf{r}') = \frac{i}{2\pi} \int_0^\infty \frac{\cos(k_x(x - x')) e^{ik_{y,1}|y-y'|}}{k_{y,1}} dk_x, \quad (3.60)$$

using this Green's function for calculating the Green's tensor results in [10]

$$\begin{aligned} \overleftrightarrow{\mathbf{G}}^{(i)}(\mathbf{r}, \mathbf{r}') &= \frac{i}{2\pi} \int_0^\infty r^{(p)}(k_x) \left(-\hat{\mathbf{x}} \hat{\mathbf{x}} \frac{k_{y,1}^2}{k_1^2} + \hat{\mathbf{y}} \hat{\mathbf{y}} \frac{k_x^2}{k_1^2} \right) \cos(k_x(x - x')) \frac{e^{ik_{y,1}(y+y')}}{k_{y,1}} \\ &\quad + r^{(p)}(k_x) (\hat{\mathbf{y}} \hat{\mathbf{x}} - \hat{\mathbf{x}} \hat{\mathbf{y}}) \frac{ik_x k_{y,1}}{k_1^2} \sin(k_x(x - x')) \frac{e^{ik_{y,1}(y+y')}}{k_{y,1}} dk_x. \end{aligned} \quad (3.61)$$

In the far field the exponential function $\exp\{ik_{y,1}(y + y')\}$ will go towards zero when $k_x > k_0 n_1$, as this is where $k_{1,y}$ is imaginary. Therefore, can the integration boundary be limited to integration from 0 to $k_0 n_1$. By doing the coordinate substitution;

$$x = r \cos \theta, \quad y = r \sin \theta, \quad \text{for } 0 < \theta < \pi, \quad (3.62)$$

$$k_x = k_1 \cos \alpha, \quad k_{y,1} = k_1 \sin \alpha, \quad \text{for } 0 < \alpha < \pi/2, \quad (3.63)$$

a shift in integration variable can be done as $dk_x = -k_{y,1}d\alpha$. The indirect Green's tensor can now be written on the form

$$\begin{aligned} \overleftrightarrow{\mathbf{G}}^{(i)}(\mathbf{r}, \mathbf{r}') &= \int_0^{\pi/2} \frac{i}{2\pi} (U(\alpha) \cos(k_x(x-x')) + Q(\alpha) \sin(k_x(x-x'))) e^{ik_{y,1}(y+y')} d\alpha, \\ \text{where } Q(\alpha) &= r^{(p)}(k_1 \cos \alpha) (\hat{\mathbf{y}}\hat{\mathbf{x}} - \hat{\mathbf{x}}\hat{\mathbf{y}}) \cos \alpha \sin \alpha, \quad \text{and} \\ U(\alpha) &= r^{(p)}(k_1 \cos \alpha) (-\hat{\mathbf{x}}\hat{\mathbf{x}} \sin^2 \alpha + \hat{\mathbf{y}}\hat{\mathbf{y}} \cos^2 \alpha), \end{aligned} \quad (3.64)$$

which follows by inserting equations (3.62) and (3.63) and using the change of integration variable on Eq. (3.46). In order to proceed the far field approximation $k_0 n_1 r \gg 1$ needs to be considered and the cosine and the sin in Eq. (3.64) must be re-written as a sum of two exponential terms. In the far field some exponential terms oscillate fast with α , and will thus vanish when considering the integration. This concept, in addition to the use of the expression

$$\int_{-\infty}^{\infty} e^{-ax^2+bx} dx = e^{b^2/4a} \sqrt{\frac{\pi}{a}}, \quad (3.65)$$

results in an analytic expression for the far field indirect Green's tensor. This is done in reference [10], and the result is

$$\begin{aligned} \overleftrightarrow{\mathbf{G}}^{(\text{ff},i)}(\mathbf{r}, \mathbf{r}') &= (-\hat{\mathbf{x}} \sin \theta + \hat{\mathbf{y}} \sin \theta)(\hat{\mathbf{x}} \sin \theta + \hat{\mathbf{y}} \cos \theta) \\ &\times e^{ik_0 n_1 r} \sqrt{\frac{2}{\pi k_0 n_1 r}} \frac{e^{i\pi/4}}{4} r^{(p)}(k_0 n_1 \cos \theta) e^{-ik_0 n_1 x' \cos \theta} e^{ik_{y,1} y'}, \quad 0 < \theta < \pi. \end{aligned} \quad (3.66)$$

3.4 Optical Cross Section

This section seeks to derive expressions of the optical cross section for the scatterer when subject to an incoming beam. The optical cross section, noted by σ , can be split into factors that contribute to an extinction of the incoming fields, such as absorption and coupling into bound modes, however, here the extinction due to scattering is of most importance. The case in question is shown in figure 3.4.

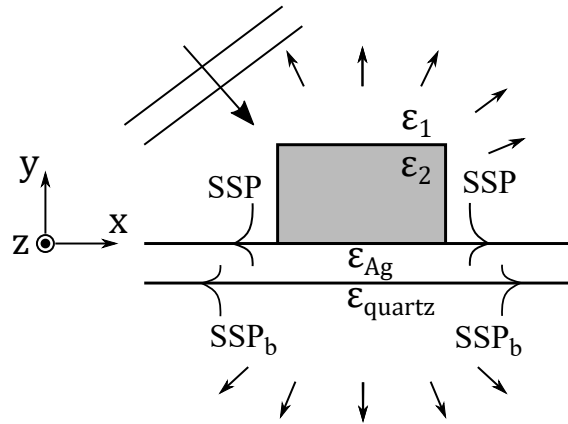


Figure 3.4. Illustration of light incident on a scatterer. The scattered light can be coupled into modes at the air-silver and silver-quartz interfaces as SPPs. Only the SPPs at the silver-quartz interface are bound modes, the SPPs at the air-silver interface will leak down into the quartz substrate and contribute to the scattered field.

It is expected that the scattering cross sections obey conservation of energy, it is thus required that

$$\sigma_{\text{ext}} = \sigma_{\text{scat}} + \sigma_{\text{abs}} + \sigma_{\text{b}}, \quad (3.67)$$

where the ext, scat, abs and b index notes extinction, scattering, absorption and bound respectively. A cross section, with regards to electromagnetism, can be found as [10]

$$\sigma = \frac{P}{I_i}, \quad (3.68)$$

where P is the power lost and I_i is the incoming intensity. If the scatterer was removed, it is appropriate to divide the cross section into two part, one for reflection and one for transmission.

The power of the reflected beam is obtained by considering only the power that is reflected directly up in the far field, thus not including the scattered field. This is done by integrating the Poynting vector for just the right angular interval such that it covers on the reflected beam. This interval is defined to be from $-\theta_b$ to θ_b . The reflected beam power can be written as

$$P_{\text{beam},r} = P_{0,r} - P_{\text{ext},r}, \quad (3.69)$$

whereas a similar expression can be formulated for the transmitted beam. The power of the reflected beam can be found by

$$P_{\text{beam},r} = \int_{-\theta_b}^{\theta_b} \frac{1}{2} \text{Real} \left\{ \mathbf{E}_{\text{beam},r}^{(\text{ff})}(\mathbf{r}, \theta) \times \left[\mathbf{H}_{\text{beam},r}^{(\text{ff})}(\mathbf{r}, \theta) \right]^* \right\} \cdot \hat{\mathbf{r}} r d\theta. \quad (3.70)$$

The reflected fields can be represented as

$$\mathbf{E}_{\text{beam},r}^{(\text{ff})}(\mathbf{r}, \theta) = \mathbf{E}_{0,r}^{(\text{ff})}(\mathbf{r}, \theta) + \mathbf{E}_{\text{scat},r}^{(\text{ff})}(\mathbf{r}, \theta), \quad (3.71)$$

which, since the far field is considered, points in the radial direction. Using that the Poynting vector, in the far field, can be written as [11]

$$\langle \mathbf{S} \rangle = \frac{1}{2\mu_0} \frac{n}{c} |E^{(\text{ff})}|^2 \hat{\mathbf{r}} \quad (3.72)$$

equation (3.70) can be written as

$$P_{\text{beam},r} = \frac{1}{2} \sqrt{\frac{\varepsilon_0}{\mu_0}} n_1 \int_{-\theta_b}^{\theta_b} |E_{0,r}^{(\text{ff})}(\mathbf{r}, \theta) + E_{\text{scat},r}^{(\text{ff})}(\mathbf{r}, \theta)|^2 r d\theta. \quad (3.73)$$

Since $P_{0,r}$ is given as

$$P_{0,r} = \frac{1}{2} \sqrt{\frac{\varepsilon_0}{\mu_0}} n_1 \int_{-\theta_b}^{\theta_b} |E_{0,r}^{(\text{ff})}(\mathbf{r}, \theta)|^2 r d\theta, \quad (3.74)$$

$P_{\text{ext},r}$ can be found to be

$$P_{\text{ext},r} = \sqrt{\frac{\varepsilon_0}{\mu_0}} n_1 \int_{-\theta_b}^{\theta_b} \text{Real} \left\{ E_{0,r}^{(\text{ff})}(\mathbf{r}, \theta) \left[E_{\text{scat},r}^{(\text{ff})}(\mathbf{r}, \theta) \right]^* \right\} r d\theta. \quad (3.75)$$

The term concerning the scattered field of second order, in equation (3.73), is assumed to be insignificant in magnitude compared to the incident field since the angular interval is small enough to only include the beam. In order to obtain analytic expressions for the powers, an expression for the incident electric field must be found. The incident electric field can be approximated as a Gaussian beam with a wide beam waist of w_0 , thus the field can be assumed to be of the form

$$\mathbf{E}_0(x, y = 0) \approx \hat{\mathbf{x}} E_0 e^{-x^2/w_0^2}. \quad (3.76)$$

The field can be found at any position y by using Fourier transformations, thus the field at any y is [11]

$$E_0(x, y) = \int \tilde{E}_0(k_x; y = 0) e^{ik_x x} e^{-ik_{y,1} y} dk_x, \quad (3.77)$$

where $k_{y,1} = \sqrt{k_0^2 n_1^2 + k_x^2}$ and

$$\tilde{E}_0(k_x; y = 0) = \int E_0(x, y = 0) e^{-ik_x x} dx. \quad (3.78)$$

By using Eq. (3.65) two times and by approximating the beam to be wide, meaning $k_0 n_1 w_0 \gg 1$, such that the paraxial approximation [11] can be used, i.e. $k_{y,1} = k_0 n_1 - k_x^2/2k_0 n_1$, the electric field can be approximated to be

$$E_0(x, y) \approx E_0 \sqrt{\frac{w_0^2}{\frac{2iy}{2r} + w_0^2}} e^{ik_0 n_1 y} \exp\left(\frac{-x^2}{\frac{2iy}{k_0 n_1} + w_0^2}\right). \quad (3.79)$$

It can be used that $y = r \cos \theta$ and $x = r \sin \theta$ for $0 < \theta < 2/(k_0 n_1 w_0)$, where the sine and cosine can be approximated by a Taylor series of the second order since the beam waist is large, meaning $\theta \ll 1$. In addition, the far field approximation $k_0 n_1 r \gg 1$ can be used to obtain the far field [10]

$$E_0^{(\text{ff})}(r, \theta) = E_0 w_0 \sqrt{\frac{k_0 n_1}{2r}} e^{-i\pi/4} e^{ik_0 n_1 r} \exp\left(-\frac{\theta^2}{4}(k_0 n_1 w_0)^2\right). \quad (3.80)$$

Then the reflected and transmitted field can be found by using the appropriate reflection and transmission coefficient. Since the beam waist radius is large only a insignificant interval of k_x is relevant, therefore it is assumed that $k_x \simeq 0$. This allows one to replace $r^{(p)}(k_x)$ and $t^{(p)}(k_x)$ with $r^{(p)}(k_x = 0)$ and $t^{(p)}(k_x = 0)$, as well as approximating $E_{\text{scat}}^{(\text{ff})}(r, \theta) \approx E_{\text{scat}}^{(\text{ff})}(r, \theta = 0)$. The reflected electric field then becomes

$$E_{0,r}^{(\text{ff})}(r, \theta) \approx -r^{(p)}(k_x = 0) E_0^{(\text{ff})}(r, \theta). \quad (3.81)$$

For the transmitted field, $x = r \sin \tilde{\theta}$ and $y = -r \sin \tilde{\theta}$ is used instead when rewriting equation (3.79) and a similar derivation is carried out. The transmitted electric field is then

$$E_{0,t}^{(\text{ff})}(r, \tilde{\theta}) \approx \frac{n_1}{n_2} t^{(p)}(k_x = 0) E_0 w_0 \sqrt{\frac{k_0 n_2}{2r}} e^{-i\pi/4} e^{-ik_0 n_2 d} e^{-ik_0 n_2 r} \exp\left(-\frac{\tilde{\theta}^2}{4}(k_0 n_2 w_0)^2\right), \quad (3.82)$$

where a factor n_1/n_2 has been added since $t^{(p)}$ is the transmission coefficient for the magnetic field [10], which is much easier to find. From these expressions the extinction power can be found analytically by the use of Eq. (3.65). The extinction power for reflected and transmitted light is

$$\begin{aligned} -P_{\text{ext},r} &= \sqrt{\frac{\varepsilon_0}{\mu_0} \frac{2\pi}{k_0 n_1}} \text{Real} \left\{ E_0 r^{(p)}(k_x = 0) \sqrt{r} \left[E_{\text{scat}}^{(\text{ff})}(\mathbf{r}, \theta = 0) \right]^* e^{-i\pi/4} e^{ik_0 n_1 r} \right\}, \text{ and} \\ -P_{\text{ext},t} &= -\sqrt{\frac{\varepsilon_0}{\mu_0} \frac{2\pi}{k_0 n_2}} \text{Real} \left\{ E_0 t^{(p)}(k_x = 0) \sqrt{r} \left[E_{\text{scat}}^{(\text{ff})}(\mathbf{r}, \theta = 0) \right]^* e^{-i\pi/4} e^{ik_0 n_2 r} e^{-ik_0 n_2 d} \right\}. \end{aligned} \quad (3.83)$$

The extinction cross section can then be found by normalizing with the incident power per unit area,

$$I_i = \frac{1}{2} \sqrt{\frac{\varepsilon_0}{\mu_0}} n_1 |E_0|^2, \quad (3.84)$$

yielding

$$\sigma_{\text{ext},r} = 2 \frac{\sqrt{\frac{2\pi}{k_0 n_1}}}{|E_0|^2} \text{Real} \left\{ E_0 r^{(p)}(k_x = 0) \sqrt{r} \left[E_{\text{scat}}^{(\text{ff})}(\mathbf{r}, \theta = 0) \right]^* e^{-i\pi/4} e^{ik_0 n_1 r} \right\}, \quad (3.85)$$

$$\sigma_{\text{ext},t} = -2 \frac{\sqrt{\frac{2\pi}{k_0 n_2}}}{|E_0|^2} \text{Real} \left\{ E_0 t^{(p)}(k_x = 0) \sqrt{r} \left[E_{\text{scat}}^{(\text{ff})}(\mathbf{r}, \theta = 0) \right]^* e^{-i\pi/4} e^{ik_0 n_2 r} e^{-ik_0 n_2 d} \right\}. \quad (3.86)$$

The scattering cross section can be found by considering the scattered field and be separated into scattering in the half plane containing reflected light and transmitted light respectively. The scattering cross sections are

$$\sigma_{\text{scat},r} = \frac{1}{|E_0|^2} \int_0^\pi |E_{\text{scat}}(r, \theta)|^2 r d\theta, \quad (3.87)$$

$$\sigma_{\text{scat},t} = \frac{n_2}{n_1} \frac{1}{|E_0|^2} \int_{-\pi}^0 |E_{\text{scat}}(r, \tilde{\theta})|^2 r d\theta, \quad (3.88)$$

where the additional factor n_2/n_1 arises since $S_{\text{scat},t} \propto n_2 |E_{\text{scat},t}|^2$ and $S_0 \propto n_1 |E_0|^2$.

It is important to note that the scatterer absorbs part of the incident wave, and thus power is lost to ohmic losses inside of the scatterer. The power absorbed is [11][18]

$$P_{\text{abs}} = \left\langle -\frac{1}{2} \int \mathbf{E}(\mathbf{r}, t) \cdot \mathbf{J}(\mathbf{r}, t) dV \right\rangle, \quad (3.89)$$

which can be simplified if there are no source currents such that $\mathbf{J}(\mathbf{r}, \omega) = \sigma(\mathbf{r}, \omega) \mathbf{E}(\mathbf{r}, \omega)$. By using the definition of ε in equation (2.15) such that $\sigma = \omega \varepsilon_0 \text{Imag}\{\varepsilon\}$ the absorption cross section for p -polarized light can be written as [10]

$$\sigma_{\text{abs}} = \frac{k_0/n_1}{|E_0|^2} \int \text{Imag}\{\varepsilon(\mathbf{r})\} |\mathbf{E}(\mathbf{r})|^2 dA. \quad (3.90)$$

3.4.1 Differential Cross Section

Instead of examining the cross section as defined in Eq. (3.68) it can be convenient to consider the differential cross section defined as the number of particles scattered into direction (θ, ϕ) pr. unit time pr. unit solid angle, divided by incident flux, [19]

$$\sigma_{\text{diff}} = \frac{\partial \sigma}{\partial \Omega}, \quad (3.91)$$

such that the cross section can be found by integrating over all solid angles, i.e.

$$\sigma = \int \sigma_{\text{diff}} d\Omega. \quad (3.92)$$

The differential cross section gives the angular distribution of the scattered particles, hence it is a useful tool to visualize e.g. far fields. The scattering cross section, which is given by equations (3.87) and (3.88), the differential scattering cross section is proportional to

$$\frac{\partial \sigma_{\text{scat}}}{\partial \Omega} \propto \langle \mathbf{S}_{\text{scat}} \cdot \hat{\mathbf{n}}r \rangle, \quad (3.93)$$

thus can be thought to represent the power scattered in all directions.

3.5 Mode Index Analysis

In this section allowed modes inside of a layer in a layered structure will be derived and discussed by a method described in Appendix F in Ref. [10]. This method utilizes a central equation, $f(k_x)$, that builds upon continuity of the fields across a layer. A mode inside of the layer will be characterized by the k_x wave number. If this wave number cannot be obtained using closed expressions, it is common to define a mode index such that k_x is given as $k_x = k_0 n_m$, where n_m is referred to as the mode index. The idea is to consider a layered structure consisting of air, then CNHP4 and finally a silver substrate; the calculations are based on figure 3.5(a).

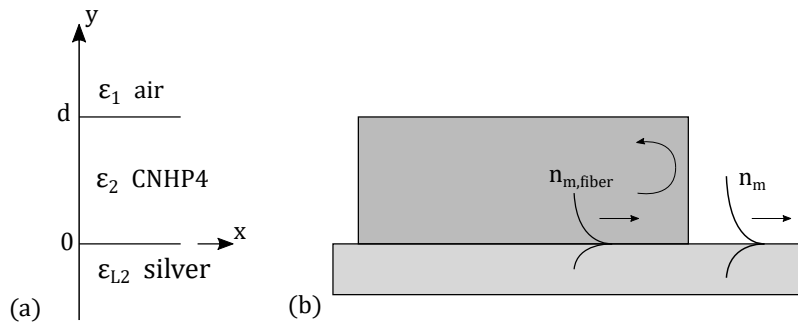


Figure 3.5. Figure (a) shows the labeling of the layers for the theoretical structure. Figure (b) illustrates SPPs being reflected and transmitted from inside of the fiber to outside.

The amount of found mode indexes equal the amount of allowed modes for a given structure, with height d . Then using the given mode index, one can calculate the wavelength of the mode as $\lambda_m = \lambda_0/n_m$. The mode index can also be used to determine whether the mode is confined inside of the fiber, as shown in figure 3.5(b). If the mode index is larger than that for the air-silver interface, then the mode can transmit out of the fiber.

3.5.1 Preliminary Theory

The following derivations are based on a layered structure given by figure 3.5(a). In this report, $\mathbf{H} = \hat{\mathbf{z}}H$ and is thus generally given by

$$H = \begin{cases} A e^{ik_{y,1}(y-d)} e^{ik_x x}, & y > 0, \\ (B e^{ik_{y,2}y} + C e^{-ik_{y,2}y}) e^{ik_x x}, & d < y < 0, \\ D e^{ik_{y,L2}y} e^{ik_x x}, & y < 0, \end{cases} \quad (3.94)$$

where A , B , C and D are constant, and $k_{y,i}^2 = k_0^2 \varepsilon_i - k_x^2$. Using boundary conditions across the first and second interface yield

$$A = B e^{ik_{y,2}d} + C e^{-ik_{y,2}d} \quad \text{and} \quad B + C = D, \quad (3.95)$$

respectively. Using that $E_x \propto \varepsilon^{-1} \partial H / \partial y$ is continuous across the same interfaces yields

$$\frac{ik_{y,1}A}{\varepsilon_1} = \frac{ik_{y,2}}{\varepsilon_2} (B e^{ik_{y,2}d} + C e^{-ik_{y,2}d}), \quad \text{and} \quad \frac{ik_{y,2}}{\varepsilon_2} (B - C) = \frac{-ik_{y,L2}}{\varepsilon_{L2}} D. \quad (3.96)$$

Solving this system of equations leads to

$$f(k_x) = e^{ik_{y,2}d} \left(1 - \frac{\varepsilon_1 k_{y,2}}{\varepsilon_2 k_{y,1}}\right) \left(1 - \frac{\varepsilon_2 k_{y,L2}}{\varepsilon_{L2} k_{y,2}}\right) + e^{-ik_{y,2}d} \left(1 + \frac{\varepsilon_1 k_{y,2}}{\varepsilon_2 k_{y,1}}\right) \left(1 + \frac{\varepsilon_2 k_{y,L2}}{\varepsilon_{L2} k_{y,2}}\right) = 0. \quad (3.97)$$

Solving this equation for $k_x = k_0 n_m$ thus gives the modes allowed for a fiber of height d . It can be solved graphically by plotting $(\text{Real}\{f(k_x)\}, \text{Imag}\{f(k_x)\}) = (0, 0)$ for different $n_m = n'_m + in''_m$ in a contour plot, and the solution is the coordinates of the crossing point of the real and imaginary part of $f(k_x)$. This is not a very accurate method, but gives a rough estimate of the mode index.

3.5.2 Results

The result of calculating these modes, with an incident wavelength of 780 nm for different values of d , is given in Tab. 3.1.

Height (d)	Mode 1			Mode 2			Mode 3		
	n'_m	n''_m	λ_m	n'_m	n''_m	λ_m	n'_m	n''_m	λ_m
100 nm	1.3900	0.0020	560	-	-	-	-	-	-
200 nm	1.6486	0.0017	473	-	-	-	-	-	-
300 nm	1.0175	0.0002	766	1.7060	0.0014	457	-	-	-
400 nm	1.1840	0.0005	659	1.7228	0.0012	453	-	-	-
500 nm	1.3460	0.0005	579	1.7286	0.0018	451	-	-	-
600 nm	1.0172	0.0002	766	1.4440	0.0004	540	1.7309	0.0011	451
700 nm	1.1338	0.0003	688	1.5030	0.0003	519	1.7320	0.0012	450
800 nm	1.2520	0.0003	623	1.5405	0.0002	506	1.7322	0.0011	450

Table 3.1. Table of allowed modes in a layer consisting of CNHP4 on top of silver, illuminated by light with a wavelength of 780 nm. The height, d , of the CNHP4 layer is shown, and the allowed modes are given to the right of that particular height.

In Tab. 3.1, for the 100 nm and 200 nm high fibers, the real values of the mode indexes are smaller than the refractive index of the fiber, which is $n = 1.65$. This means that the modes

are propagating modes inside of the fiber for these heights, however, since the modes have a larger real value than air, the modes decays away from the fiber. This creates guided mode, which for small d behaves like a regular plasmon, thus it can be understood as a pseudo-SPP. For larger heights semi consistent a SPP mode is found. The mode index for these are around $n_m \approx 1.7254 + i0.0013$, thus the average mode wavelength is 452 nm.

The result of calculating these modes, with an incident wavelength of 390 nm for different values of d , is given in Tab. 3.2.

	n'_m	n''_m	λ_m	n'_m	n''_m	λ_m
Height (d)	Mode 1			Mode 2		
100 nm	3.006	0.1802	130	-	-	-
200 nm	3.007	0.1796	130	1.301	0.0032	300
300 nm	3.007	0.1796	130	1.070	0.0002	364
400 nm	3.007	0.1796	130	1.315	0.0016	296
500 nm	3.007	0.1796	130	1.163	0.0016	335
	Mode 3			Mode 4		
100 nm	-	-	-	-	-	-
200 nm	-	-	-	-	-	-
300 nm	1.503	0.0011	260	-	-	-
400 nm	1.570	0.0005	248	-	-	-
500 nm	1.443	0.0009	270	1.600	0.0002	244

Table 3.2. Table of allowed modes in a layer consisting of CNHP4 on top of silver, illuminated by light with a wavelength of 390 nm. The height, d , of the CNHP4 layer is shown, and the allowed modes are given to the right of that particular height.

In Tab 3.2 a consistent mode of around $n_m = 3.007 + i0.1796$ is found for all heights. This results in a SPP mode wavelength around 130 nm. Compared to the 780 nm case, more allowed modes appear for higher fibers, which is most likely a result of the shorter wavelength.

The decay length into the fiber of the SPP into can be calculated as $1/|\text{Imag}\{k_{y,1}\}|$, where $k_{y,1}$ is given as [11]

$$k_{y,2} = \frac{2\pi}{\lambda_m} \sqrt{\frac{\varepsilon_2^2}{\varepsilon'_{L2} + \varepsilon_2}} \left(1 - i \frac{\varepsilon''_{L2}}{2(\varepsilon'_{L2} + \varepsilon_2)} \right), \quad (3.98)$$

where ε_2 and $\varepsilon_{L2} = \varepsilon'_{L2} + i\varepsilon''_{L2}$ is the dielectric constant of CNHP4 and silver respectively. Calculating the decay length for the two modes, $n_m \approx 1.7254 + i0.0013$ and $n_m \approx 3.007 + i0.1796$, yields decay lengths of around 20 000 nm and 95 nm respectively. The long decay length of the 780 nm mode is a results of the real part of the mode index being close to the refractive index of the fiber, thus the modes are less localized to the interface. Interestingly, that coincides with how stable the modes are for the different heights; the consistent mode for 780 nm incoming light varies a little for the different heights due to the tail interfering with the air-fiber interface, and the mode recorded for 390 nm is stable for all heights, due to the tail not reaching the other interface. As mentioned in order for these modes in the fiber to transmit to the interface outside of the fiber, i.e. going from a fiber-silver to a air-silver interface, the mode index for the air-silver SPP needs to be

smaller than the SPP mode index for fiber-silver interface. It is thus of interest to calculate the mode index for the SPP outside of the fiber, which can be found by equation (2.36), i.e.

$$n'_m = \text{Real} \left\{ \sqrt{\frac{\varepsilon_{L2}}{\varepsilon_{L2} + 1}} \right\}. \quad (3.99)$$

The real part of the mode index outside of the fiber can thus be calculated to be 1.1607 for the 390 nm incident wave, and 1.0175 for the 780 nm incident wave. These are significantly smaller than those found in Tab. 3.1 and 3.2, thus the SPPs would easily transmit to the air-silver interface.

Chapter 4

Scattering Problem in Three Dimensions

This chapter seeks to expand the equations and concepts, presented in chapter 3 into three dimensions. Most of the results are very similar, as are most of the methods. In addition, the theory follows closely chapter 6 in [10], thus the theory will not be summarized in detail, however the main results important for constructing a 3D simulation regarding a scatterer on top of a layered structure will be discussed.

First consider the wave equation (2.20) where now $\mathbf{r} = \hat{\mathbf{x}}x + \hat{\mathbf{y}}y + \hat{\mathbf{z}}z$. A reference structure defined by $\varepsilon_{\text{ref}}(\mathbf{r})$, which is the dielectric function for the structure without the scatterer, is then introduced. This can be added into the wave equation such that the left side of the wave equation is zero outside of the scatterer. This leads to the Green's function volume integral equation

$$\mathbf{E}(\mathbf{r}) = \mathbf{E}_0(\mathbf{r}) + \int \overleftrightarrow{\mathbf{G}}(\mathbf{r}, \mathbf{r}') k_0^2 \cdot (\varepsilon(\mathbf{r}') - \varepsilon_{\text{ref}}(\mathbf{r}')) \mathbf{E}(\mathbf{r}') d^3 r'. \quad (4.1)$$

4.1 Scatterer On a Layered Structure

In this section the direct and indirect Green's tensor will be derived for a scatterer on top of a layered structure. As before, the direct Green's tensor can be found analytically whilst the indirect Green's tensor can be derived by considering a mode expansion method.

4.1.1 Direct Green's Tensor

The direct Green's tensor needs to solve

$$(-\nabla \times \nabla \times + k_0^2 \varepsilon_1) \overleftrightarrow{\mathbf{G}}^{(d)}(\mathbf{r}, \mathbf{r}') = -\overleftrightarrow{\mathbf{I}} \delta(\mathbf{r} - \mathbf{r}'), \quad (4.2)$$

where a solution can be found as

$$\overleftrightarrow{\mathbf{G}}^{(d)}(\mathbf{r}, \mathbf{r}') = \left(\overleftrightarrow{\mathbf{I}} + \frac{1}{k_0^2 \varepsilon_1} \nabla \nabla \right) g^{(d)}(\mathbf{r}, \mathbf{r}'). \quad (4.3)$$

Equation (4.2) is satisfied if the direct Green's function satisfies

$$(\nabla^2 + k_0^2 \varepsilon_1) g^{(d)}(\mathbf{r}, \mathbf{r}') = -\delta(\mathbf{r}, \mathbf{r}'), \quad (4.4)$$

where it can be shown that

$$g^{(d)}(\mathbf{r}, \mathbf{r}') = \frac{e^{ik_0\varepsilon_1|\mathbf{r}-\mathbf{r}'|}}{4\pi|\mathbf{r}-\mathbf{r}'|} \quad (4.5)$$

is a solution [10][15]. The direct Green's tensor can then be found analytically by differentiation and using the dyadic operator $\nabla\nabla = \hat{\mathbf{x}}\hat{\mathbf{x}}\frac{\partial^2}{\partial x^2} + \hat{\mathbf{y}}\hat{\mathbf{y}}\frac{\partial^2}{\partial y^2} + (\hat{\mathbf{x}}\hat{\mathbf{y}} + \hat{\mathbf{y}}\hat{\mathbf{x}})\frac{\partial^2}{\partial x\partial y}$ to be

$$\overleftrightarrow{\mathbf{G}}^{(d)}(\mathbf{r}, \mathbf{r}') = \left(\overleftrightarrow{\mathbf{I}} \left[1 + \frac{i}{k_1 R} - \frac{1}{(k_1 R)^2} \right] - \frac{\mathbf{R}\mathbf{R}}{R^2} \left[1 + \frac{3i}{k_1 R} - \frac{3}{(k_1 R)^2} \right] \right) g^{(d)}(\mathbf{r}, \mathbf{r}'), \quad (4.6)$$

where $\mathbf{R} = \mathbf{r} - \mathbf{r}'$, $R = |\mathbf{R}|$ and $k_1 = k_0 n_1$.

4.1.2 Indirect and Transmitted Green's Tensor

The indirect Green's tensor can be constructed by considering a plane wave expansion of equation (4.5) as applied previously. The plane wave expansion is [20]

$$g^{(d)}(\mathbf{r}, \mathbf{r}') = \frac{i}{2} \frac{1}{(2\pi)^2} \int_{k_x} \int_{k_y} \frac{e^{ik_x(x-x')} e^{ik_y(y-y')} e^{ik_{z,1}|z-z'|}}{k_{z,1}} dk_x dk_y, \quad (4.7)$$

where $k_{z,1} = \sqrt{k_0^2\varepsilon_1 - k_x^2 - k_y^2}$. This can be shown using an eigenvalue expansion method [15] and introducing an imaginary part to the poles of the equation. The direct Green's function can then be expressed as [10]

$$g^{(d)}(\mathbf{r}, \mathbf{r}') = \lim_{\alpha \rightarrow 0^+} \int \frac{e^{i\mathbf{k}\cdot(\mathbf{r}-\mathbf{r}')}}{(2\pi)^3 \left(k_z - \left(\sqrt{k_0^2\varepsilon_1 - k_\rho^2} + i\alpha \right) \right) \left(k_z + \left(\sqrt{k_0^2\varepsilon_1 - k_\rho^2} + i\alpha \right) \right)} d^3k, \quad (4.8)$$

where $k_\rho^2 = k_x^2 + k_y^2$. Now residual calculations using the same methods as the ones previously leads to the plane wave expansion, equation (4.7). Using polar coordinates

$$k_x = k_1 \cos \theta_k, \quad x - x' = \rho_r \cos \theta_r, \quad (4.9)$$

$$k_y = k_1 \sin \theta_k, \quad y - y' = \rho_r \sin \theta_r, \quad (4.10)$$

the Bessel J of 0'th order can be found in the equation such that,

$$g^{(d)}(\mathbf{r}, \mathbf{r}') = \frac{i}{4\pi} \int_0^\infty \frac{J_0(k_\rho \rho_r) e^{ik_{z,1}|z-z'|}}{k_{z,1}} k_\rho dk_\rho. \quad (4.11)$$

Inserting this equation into Eq. (4.3) and using that the gradient can be expressed for cylindrical coordinates as $\nabla = \hat{\mathbf{z}}\frac{\partial}{\partial z} + \hat{\boldsymbol{\rho}}_r\frac{\partial}{\partial \rho_r} + \hat{\boldsymbol{\phi}}_r\frac{1}{\rho_r}\frac{\partial}{\partial \phi_r}$, the direct Green's tensor can be derived to be

$$\begin{aligned} \overleftrightarrow{\mathbf{G}}^{(d)}(\mathbf{r}, \mathbf{r}') = & \frac{1}{4\pi} \int_0^\infty \left\{ \hat{\boldsymbol{\rho}}_r \hat{\boldsymbol{\rho}}_r \left(J_0(k_\rho \rho_r) + \frac{k_\rho^2}{k_1^2} J_0''(k_\rho \rho_r) \right) + \hat{\boldsymbol{\phi}}_r \hat{\boldsymbol{\phi}}_r \left(J_0(k_\rho \rho_r) + \frac{k_\rho^2}{k_1^2} \frac{J_0'(k_\rho \rho_r)}{k_\rho \rho_r} \right) \right. \\ & \left. + \hat{\mathbf{z}} \hat{\mathbf{z}} \frac{k_\rho^2}{k_1^2} J_0(k_\rho \rho_r) + (\hat{\boldsymbol{\rho}}_r \hat{\mathbf{z}} + \hat{\mathbf{z}} \hat{\boldsymbol{\rho}}_r) \frac{ik_{z,1} k_\rho}{k_1^2} \frac{z-z'}{|z-z'|} J_0'(k_\rho \rho_r) \right\} e^{ik_{z,1}|z-z'|} \frac{k_\rho}{k_{z,1}} dk_\rho, \quad (4.12) \end{aligned}$$

where $k_\rho^2 = k_1^2 - k_{z,1}^2$. The next step is to find the incident, reflected and transmitted electric fields in order to construct the dyadic tensors. This is done for a two layered reference structure defined by

$$\varepsilon_{\text{ref}}(\mathbf{r}) = \begin{cases} \varepsilon_1, & z > 0 \\ \varepsilon_{L2}, & z < 0 \end{cases}. \quad (4.13)$$

Consider now an incident field where $0 < z < z'$ which can be written as

$$\mathbf{E}_i(\mathbf{r}) = \mathbf{E}_{i,x}(\mathbf{r}) + \mathbf{E}_{i,y}(\mathbf{r}) + \mathbf{E}_{i,z}(\mathbf{r}). \quad (4.14)$$

These parts can be found by taking the appropriate component of the direct Green's tensor. However, since the fields are three dimensional both p - and s -polarization needs to be considered, thus the total field becomes

$$\mathbf{E}(\mathbf{r}) = \begin{cases} \mathbf{E}_i^{(s)}(\mathbf{r}) + \mathbf{E}_i^{(p)}(\mathbf{r}) + \mathbf{E}_r^{(s)}(\mathbf{r}) + \mathbf{E}_r^{(p)}(\mathbf{r}), & z > 0 \\ \mathbf{E}_t^{(s)}(\mathbf{r}) + \mathbf{E}_t^{(p)}(\mathbf{r}), & z < 0 \end{cases}. \quad (4.15)$$

Using these fields the appropriate Green's tensors can be found. It is intended for the Green's tensor to become of the form

$$\overleftrightarrow{\mathbf{G}}(\mathbf{r}, \mathbf{r}') = \begin{cases} \overleftrightarrow{\mathbf{G}}^{(d)}(\mathbf{r}, \mathbf{r}') + \overleftrightarrow{\mathbf{G}}^{(i)}(\mathbf{r}, \mathbf{r}'), & z > 0 \\ \overleftrightarrow{\mathbf{G}}^{(t)}(\mathbf{r}, \mathbf{r}'), & z < 0 \end{cases}, \quad (4.16)$$

where

$$\overleftrightarrow{\mathbf{G}}^{(t)}(\mathbf{r}, \mathbf{r}') = \mathbf{E}_{t,x}(\mathbf{r})\hat{\mathbf{x}} + \mathbf{E}_{t,y}(\mathbf{r})\hat{\mathbf{y}} + \mathbf{E}_{t,z}(\mathbf{r})\hat{\mathbf{z}}, \quad (4.17)$$

and

$$\overleftrightarrow{\mathbf{G}}^{(i)}(\mathbf{r}, \mathbf{r}') = \mathbf{E}_{r,x}(\mathbf{r})\hat{\mathbf{x}} + \mathbf{E}_{r,y}(\mathbf{r})\hat{\mathbf{y}} + \mathbf{E}_{r,z}(\mathbf{r})\hat{\mathbf{z}}. \quad (4.18)$$

The Indirect Green's tensor can then be obtained as

$$\begin{aligned} \overleftrightarrow{\mathbf{G}}^{(i)}(\mathbf{r}, \mathbf{r}') &= \frac{i}{4\pi} \int_0^\infty \left\{ r^{(p)}(k_\rho) \left(\hat{\mathbf{z}}\hat{\mathbf{z}}J_0(k_\rho\rho_r) \frac{k_\rho^2}{k_1^2} + \hat{\phi}_r\hat{\phi}_r \frac{J'_0(k_\rho\rho_r)}{k_\rho\rho_r} \frac{k_{z,1}^2}{k_1^2} \right. \right. \\ &\quad \left. \left. + \hat{\rho}_r\hat{\rho}_r J_0''(k_\rho\rho_r) \frac{k_{z,1}^2}{k_1^2} - (\hat{\mathbf{z}}\hat{\rho}_r - \hat{\rho}_r\hat{\mathbf{z}}) \frac{ik_{z,1}k_\rho}{k_1^2} J'_0(k_\rho\rho_r) \right) \right. \\ &\quad \left. - r^{(s)}(k_\rho) \left(\hat{\phi}_r\hat{\phi}_r J_0''(k_\rho\rho_r) + \hat{\rho}_r\hat{\rho}_r \frac{J'_0(k_\rho\rho_r)}{k_\rho\rho_r} \right) \right\} e^{ik_{z,1}(z+z')} \frac{k_\rho}{k_{z,1}} dk_\rho, \end{aligned} \quad (4.19)$$

and the transmitted Green's tensor as

$$\begin{aligned} \overleftrightarrow{\mathbf{G}}^{(t)}(\mathbf{r}, \mathbf{r}') &= \frac{i}{4\pi} \int_0^\infty \left\{ t^{(p)}(k_\rho) \frac{\varepsilon_1}{\varepsilon_{L2}} \left(\hat{\mathbf{z}}\hat{\mathbf{z}}J_0(k_\rho\rho_r) \frac{k_\rho^2}{k_1^2} - \hat{\phi}_r\hat{\phi}_r \frac{J'_0(k_\rho\rho_r)}{k_\rho\rho_r} \frac{k_{z,1}k_{z,L2}}{k_1^2} \right. \right. \\ &\quad \left. \left. - \hat{\rho}_r\hat{\rho}_r J_0''(k_\rho\rho_r) \frac{k_{z,1}k_{z,L2}}{k_1^2} - \left(\hat{\mathbf{z}}\hat{\rho}_r + \hat{\rho}_r\hat{\mathbf{z}} \frac{k_{z,L2}}{k_{z,1}} \right) \frac{ik_{z,1}k_\rho}{k_1^2} J'_0(k_\rho\rho_r) \right) \right. \\ &\quad \left. - t^{(s)}(k_\rho) \left(\hat{\phi}_r\hat{\phi}_r J_0''(k_\rho\rho_r) + \hat{\rho}_r\hat{\rho}_r \frac{J'_0(k_\rho\rho_r)}{k_\rho\rho_r} \right) \right\} e^{ik_{z,1}z'} e^{-ik_{z,L2}z} \frac{k_\rho}{k_{z,1}} dk_\rho. \end{aligned} \quad (4.20)$$

4.2 Far Fields and Cross Sections

In order to derive an expression for the electric field in the far field one must first derived both the direct and indirect far field Green's tensors. The far field direct Green's tensor is derived by considering the result obtained previously, namely equation (4.6). In relation to the far field, \mathbf{r}' is close to the origin in comparison to \mathbf{r} . This means that $\mathbf{R} = \mathbf{r} - \mathbf{r}' \approx \mathbf{r}$. Then removing all terms that converge to zero, as $k_1 r \rightarrow \infty$, yields

$$\overleftrightarrow{\mathbf{G}}^{(\text{ff},d)}(\mathbf{r}, \mathbf{r}') = \left(\overleftrightarrow{\mathbf{I}} - \hat{\mathbf{r}}\hat{\mathbf{r}} \right) g^{(\text{ff},d)}(\mathbf{r}, \mathbf{r}'). \quad (4.21)$$

Using that $\overleftrightarrow{\mathbf{I}} = \hat{\mathbf{r}}\hat{\mathbf{r}} + \hat{\boldsymbol{\theta}}\hat{\boldsymbol{\theta}} + \hat{\boldsymbol{\phi}}\hat{\boldsymbol{\phi}}$ and that $|\mathbf{r} - \mathbf{r}'| \approx r - \hat{\mathbf{r}} \cdot \mathbf{r}'$ in the far field, the tensor can be written as

$$\overleftrightarrow{\mathbf{G}}^{(\text{ff},d)}(\mathbf{r}, \mathbf{r}') = \left(\hat{\boldsymbol{\theta}}\hat{\boldsymbol{\theta}} + \hat{\boldsymbol{\phi}}\hat{\boldsymbol{\phi}} \right) \frac{e^{ik_1 r} e^{-ik_1 \hat{\mathbf{r}} \cdot \mathbf{r}'}}{4\pi r}. \quad (4.22)$$

In order to get an analytic expression for the indirect Green's tensor, one must consider equation (4.19). The same methods can be applied as for the two dimensional case, where the fast oscillating exponential terms vanishes evaluating the integral. In this context, it is required to approximate the Bessel J functions for large x , as done in Eq. (3.55), in which the mentioned exponential terms are found. Along with a coordinate shift and replacing the integration boundaries, the indirect Green's tensor can be analytically found as [10]

$$\overleftrightarrow{\mathbf{G}}^{(\text{ff},i)}(\mathbf{r}, \mathbf{r}') = \frac{e^{ik_1 r}}{4\pi r} e^{-ik_\rho \mathbf{r} \cdot \hat{\boldsymbol{\rho}}} e^{ik_{z,1} z'} \left(r^{(s)}(k_\rho) \hat{\boldsymbol{\phi}}\hat{\boldsymbol{\phi}} - r^{(s)}(k_\rho) \hat{\boldsymbol{\theta}} \left(\hat{\mathbf{z}} \frac{k_\rho}{k_1} + \hat{\boldsymbol{\rho}} \frac{k_{z,1}}{k_1} \right) \right). \quad (4.23)$$

These far field Green's tensors constitutes the electric field in the far field by

$$\mathbf{E}_{\text{scat}}^{(\text{ff})}(\mathbf{r}) = \int \overleftrightarrow{\mathbf{G}}^{(\text{ff})}(\mathbf{r}, \mathbf{r}') k_0^2 (\varepsilon(\mathbf{r}') - \varepsilon_{\text{ref}}(\mathbf{r}')) \cdot \mathbf{E}(\mathbf{r}') d^3 r', \quad z > 0. \quad (4.24)$$

Using equation (4.23) and (4.22), equation (4.24) can be split up into a direct and indirect part given by

$$\mathbf{E}_{\text{scat}}^{(\text{ff},d)}(\mathbf{r}) = \frac{e^{ik_1 r}}{4\pi r} (\hat{\boldsymbol{\theta}}\hat{\boldsymbol{\theta}} + \hat{\boldsymbol{\phi}}\hat{\boldsymbol{\phi}}) \cdot \int k_0^2 (\varepsilon(\mathbf{r}') - \varepsilon_{\text{ref}}(\mathbf{r}')) e^{-ik_1 \mathbf{r}' \cdot \hat{\boldsymbol{\rho}}} \mathbf{E}(\mathbf{r}') d^3 r', \quad (4.25)$$

and

$$\begin{aligned} \mathbf{E}_{\text{scat}}^{(\text{ff},i)}(\mathbf{r}) = & \frac{e^{ik_1 r}}{4\pi r} \left(-r^{(p)}(k_{k_\rho}) \hat{\boldsymbol{\theta}} \left(\hat{\mathbf{z}} \frac{k_\rho}{k_1} + \hat{\boldsymbol{\rho}} \frac{k_{z,1}}{k_1} \right) + r^{(s)}(k_\rho) \hat{\boldsymbol{\phi}}\hat{\boldsymbol{\phi}} \right) \\ & \cdot \int k_0^2 (\varepsilon(\mathbf{r}') - \varepsilon_{\text{ref}}(\mathbf{r}')) e^{ik_\rho \mathbf{r}' \cdot \hat{\boldsymbol{\rho}}} e^{ik_{z,1} z'} \mathbf{E}(\mathbf{r}') d^3 r', \end{aligned} \quad (4.26)$$

respectively. By applying these fields the scattering cross sections for the three dimension case can be found as

$$\sigma_{\text{scat},r} = \frac{1}{|\mathbf{E}_0|^2} \int_0^{\pi/2-} \int_0^{2\pi} |\mathbf{E}_{\text{scat}}^{(\text{ff})}(\mathbf{r})|^2 r^2 \sin \theta d\theta d\phi, \quad (4.27)$$

and

$$\sigma_{\text{scat},t} = \frac{1}{|\mathbf{E}_0|^2} \frac{n_2}{n_1} \int_{\pi/2+}^{\pi} \int_0^{2\pi} |\mathbf{E}_{\text{scat}}^{(\text{ff})}(\mathbf{r})|^2 r^2 \sin \theta d\theta d\phi. \quad (4.28)$$

4.3 Second Harmonic Generation

Some materials responds non-linearly to an electric field. These effects arise due to a non-linear response of embedded dipoles in the material. These dipoles facilitate valence electrons that responds in a non-linear manner when excited by an external electric field [21]. The non-linear response can found in the polarization density in the frequency domain given by [22]

$$P(\omega) = \varepsilon_0 \left(\chi^{(1)}(\omega)E(\omega) + \chi^{(2)}(\omega = \omega' + \omega'')E(\omega')E(\omega'') + \dots + \chi^{(n)}(\omega = \omega' + \omega'' + \dots + \omega^{(n)})E(\omega)\dots E(\omega^{(n)}) \right), \quad (4.29)$$

where $\chi^{(n)}$ is the response strength of the n th term. The second term is called the sum-frequency generation since it sums the frequency as $\omega = \omega' + \omega''$. Second harmonic generation (SHG) is a special case of the sum frequency generation where $\omega' = \omega'' = \omega$, this is denoted as $2\omega = \omega' + \omega''$. This effect is examined in the report, thus other higher order effects are ignored. This also implies $E(\omega')E(\omega'') = (E(\omega))^2$. The resulting second harmonic (SH) dipole polarization can thus be expressed as

$$P(\mathbf{r}, 2\omega) = \chi^{(2)}(E(\mathbf{r}, \omega))^2. \quad (4.30)$$

Considering that the dipoles are orientated in some direction the polarization density needs to be rewritten. The polarization density points in the same direction as the dipoles, noted $\hat{\mathbf{n}}_{\text{dip}}$, and is driven by the component of the electric field that points in that direction. The polarization density is thus on the form,

$$\mathbf{P}(\mathbf{r}, 2\omega) = \chi^{(2)}\hat{\mathbf{n}}_{\text{dip}}(\hat{\mathbf{n}}_{\text{dip}} \cdot \mathbf{E}(\mathbf{r}, \omega))^2. \quad (4.31)$$

SHG, in a scattering fiber, becomes a new source of fields that is subject to scattering from the moment it is generated. The field that is calculated for the reference structure takes the form

$$\mathbf{E}_0(\mathbf{r}, 2\omega) = \int \overleftrightarrow{\mathbf{G}}(\mathbf{r}, \mathbf{r}'; 2\omega) \frac{(2\omega)^2}{c^2} \cdot \frac{\mathbf{P}(\mathbf{r}, 2\omega)}{\varepsilon_0} d^3r'. \quad (4.32)$$

This in turn leads to the total field generated by a scatterer with SH properties;

$$\mathbf{E}(\mathbf{r}, 2\omega) = \mathbf{E}_0(\mathbf{r}, 2\omega) + \int \overleftrightarrow{\mathbf{G}}(\mathbf{r}, \mathbf{r}'; 2\omega) \frac{(2\omega)^2}{c^2} \cdot (\varepsilon(\mathbf{r}') - \varepsilon_{\text{ref}}(\mathbf{r}'))\mathbf{E}(\mathbf{r}, 2\omega) d^3r'. \quad (4.33)$$

In order to find the scattering cross section the far field of the scattered field needs to be found. This deviates from the linearly scattered field, which is also called fundamental harmonic (FH) scattering, since $E_0(2\omega)$ now contributes to the far field. The scattered far field is given as

$$\mathbf{E}_{\text{scat}}^{(\text{ff})}(\mathbf{r}, 2\omega) = \int \overleftrightarrow{\mathbf{G}}^{(\text{ff})}(\mathbf{r}, \mathbf{r}'; 2\omega) \frac{(2\omega)^2}{c^2} \cdot \left(\frac{\mathbf{P}(\mathbf{r}, 2\omega)}{\varepsilon_0} + (\varepsilon(\mathbf{r}') - \varepsilon_{\text{ref}}(\mathbf{r}'))\mathbf{E}(\mathbf{r}, 2\omega) \right) d^3r'. \quad (4.34)$$

Chapter 5

Numerical Conversion and Solution Method

In chapter 3, equations for finding the electric field resulting from scattering by a scatterer on a layered structure were found. However, these require that complicated integrals are solved. This section aims to discretize these equations so that they can be solved numerically, and then finding a method for solving these equations quickly and finally applying them to the situation of a CNHP4 nanofiber on a silver film on quartz.

5.1 Discretization into Square Elements

The initial step is to discretize the fiber into smaller elements, and for the given problem the most practical approach would be to use a square discretization. The idea is to divide an area that includes the entire scatterer into small square elements and assigning each element a dielectric constant in order to represent the scatterer. In order to simplify the problem, the discretization is chosen in such a way that the height of the fiber are described by an integer amount of squares.

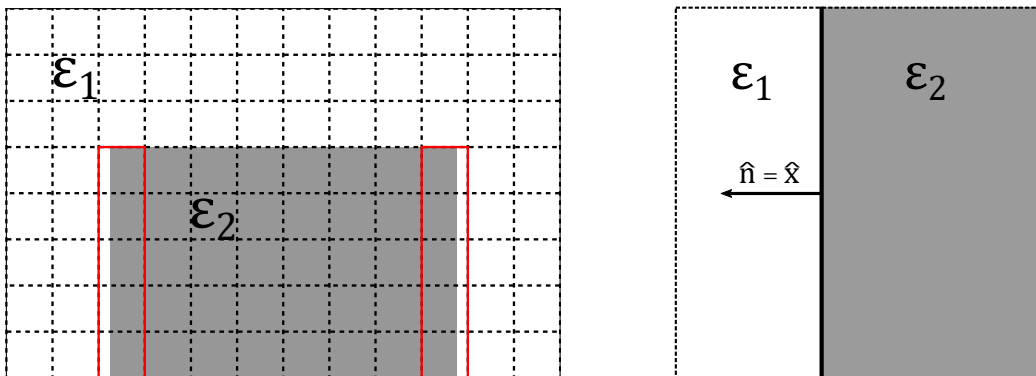


Figure 5.1. The left figure represents an area that has been discretized and the cells within the fiber have value ϵ_2 . The cells marked with red, have a dielectric constant that is a combination between ϵ_1 and ϵ_2 . The right figure is a closer look at one such cell.

However, not every square will be guaranteed to have a uniform dielectric constant, e.g. if the width of the strip does not match an integer amount of squares. This results in the cell

having some part ε_1 and some part ε_2 . An example of this is shown in figure 5.1, where the red boxes indicate which cells will have such a shared dielectric constant.

For these boxes an appropriate dielectric constant must be chosen. This is done by using an average for the cell. However, one must consider the polarization before calculating. For s -polarization, the field lies in the z -direction and is therefore parallel with every interface, thus for a cell i the dielectric constant is calculated as [23]

$$\varepsilon_{\parallel,i} = \frac{1}{\Delta_i} \int_i \varepsilon(\mathbf{r}) d^2r, \quad (5.1)$$

where Δ_i is the area of cell i . For p -polarization the field consists of a combination of components which is parallel and perpendicular to the interface. Following the same reason, if a component of a field is in the direction of the $\hat{\mathbf{n}}$ unit vector, the effective dielectric constant can be calculated as [23]

$$\frac{1}{\varepsilon_{\perp,i}} = \frac{1}{\Delta_i} \int_i \frac{1}{\varepsilon(\mathbf{r})} d^2r. \quad (5.2)$$

A tensor expression for the dielectric constant can be written as a combination of the two and results in a effective ε_i for p -polarization on the form;

$$\varepsilon_i = \varepsilon_{\perp,i} \hat{\mathbf{n}}\hat{\mathbf{n}} + \varepsilon_{\parallel,i} (\overleftrightarrow{\mathbf{I}} - \hat{\mathbf{n}}\hat{\mathbf{n}}). \quad (5.3)$$

In this report the fiber will always be assumed square and so will the discretization, and since the discretization is chosen to fit with the height of the fiber, only the sides will pose the possible problem of an averaged dielectric constant. Therefore, $\hat{\mathbf{n}}$ will be equal $\hat{\mathbf{x}}$ for any case in this report.

5.2 Numerical Method

In previous sections the direct and indirect Green's tensor was derived. In general the tensor, $\overleftrightarrow{\mathbf{G}}$, can be expressed as

$$\overleftrightarrow{\mathbf{G}} = \hat{\mathbf{x}}\hat{\mathbf{x}}G_{xx} + \hat{\mathbf{x}}\hat{\mathbf{y}}G_{xy} + \hat{\mathbf{y}}\hat{\mathbf{x}}G_{yx} + \hat{\mathbf{y}}\hat{\mathbf{y}}G_{yy}. \quad (5.4)$$

Similarly, the dielectric constant tensor, for a cell i , can be expressed as

$$\overleftrightarrow{\varepsilon}_i = \hat{\mathbf{x}}\hat{\mathbf{x}}\varepsilon_{xx,i} + \hat{\mathbf{x}}\hat{\mathbf{y}}\varepsilon_{xy,i} + \hat{\mathbf{y}}\hat{\mathbf{x}}\varepsilon_{yx,i} + \hat{\mathbf{y}}\hat{\mathbf{y}}\varepsilon_{yy,i}. \quad (5.5)$$

Since $\hat{\mathbf{n}} = \hat{\mathbf{x}}$ for a square fiber, equation (5.3) will not have dyadic $\hat{\mathbf{x}}\hat{\mathbf{y}}$ - or $\hat{\mathbf{y}}\hat{\mathbf{x}}$ -components. This would not be the case if $\hat{\mathbf{n}}$ pointed such that it is a combination of $\hat{\mathbf{x}}$ and $\hat{\mathbf{y}}$, as the dyadic $\hat{\mathbf{n}}\hat{\mathbf{n}}$ would then have $\hat{\mathbf{x}}\hat{\mathbf{y}}$ - or $\hat{\mathbf{y}}\hat{\mathbf{x}}$ -components.

It is assumed that within each cell both the reference electric field, $\mathbf{E}_{0,i}$, and total electric field are constant and can be written of the form $\mathbf{E}_i = \hat{\mathbf{x}}E_{x,i} + \hat{\mathbf{y}}E_{y,i}$. Given these assumptions and definitions, the integral equation in (3.17) can be written in discrete form as

$$\mathbf{E}_i = \mathbf{E}_{0,i} + \sum_j \overleftrightarrow{\mathbf{G}}_{ij} \cdot k_0^2 (\overleftrightarrow{\varepsilon}_j - \overleftrightarrow{\mathbf{I}} \varepsilon_{\text{ref}}) \cdot \mathbf{E}_j, \quad (5.6)$$

where

$$\overleftrightarrow{\mathbf{G}}_{ij} = \overleftrightarrow{\mathbf{G}}_{ij}^{(d)} + \overleftrightarrow{\mathbf{G}}_{ij}^{(i)} = \int_j \overleftrightarrow{\mathbf{G}}(\mathbf{r}_i, \mathbf{r}') d^2 r'. \quad (5.7)$$

However, both the direct and indirect Green's functions both have highly singular points. For the indirect part, this problem is circumvented by integrating around the singular point in the complex plane, and was discussed in Section 4.2.1 in Ref. [10]. However, the direct Green's tensor is only singular when $i = j$. In order to solve this, the area integral is converted to a surface integral for a surface that is far away from the point that is singular [24][25]. First the integral of the Green's tensor can be written as

$$\int_i \overleftrightarrow{\mathbf{G}}^{(d)}(\mathbf{r}_i, \mathbf{r}') = \int_i \left(\overleftrightarrow{\mathbf{I}} + \frac{1}{k^2} \nabla' \nabla' \right) g^{(d)}(\mathbf{r}_i, \mathbf{r}') d^2 r'. \quad (5.8)$$

However, the scalar Green's function, $g^{(d)}$, satisfies

$$(\nabla^2 + k^2) g^{(d)}(\mathbf{r}_i, \mathbf{r}') = -\delta(\mathbf{r} - \mathbf{r}'), \quad (5.9)$$

which implies that

$$g^{(d)}(\mathbf{r}_i, \mathbf{r}') = -\frac{1}{k^2} \nabla^2 g^{(d)}(\mathbf{r}_i, \mathbf{r}') - \frac{1}{k^2} \delta(\mathbf{r} - \mathbf{r}'). \quad (5.10)$$

If equation (5.10) is inserted into equation (5.8) and the divergence theorem is applied, it leads to

$$\int_i \overleftrightarrow{\mathbf{G}}^{(d)}(\mathbf{r}_i, \mathbf{r}') d^2 r' = -\frac{1}{k^2} \overleftrightarrow{\mathbf{I}} + \frac{1}{k^2} \int_{\partial i} (\hat{\mathbf{n}}' \nabla - \overleftrightarrow{\mathbf{I}} \hat{\mathbf{n}}' \cdot \nabla') g^{(d)}(\mathbf{r}_i, \mathbf{r}') dl', \quad (5.11)$$

where ∂i is the size of the line element i . In the limit of ∂i becoming very small, equation (5.11) goes towards a constant value [10];

$$\overleftrightarrow{\mathbf{G}}_{ii}^{(d)} = -\frac{\overleftrightarrow{\mathbf{I}}}{2k^2}. \quad (5.12)$$

For every point an appropriate approximation for the direct Green's tensor is thus

$$\overleftrightarrow{\mathbf{G}}_{ij}^{(d)} \simeq \begin{cases} \overleftrightarrow{\mathbf{G}}^{(d)}(\mathbf{r}_i, \mathbf{r}_j) \Delta_j, & i \neq j, \\ -\overleftrightarrow{\mathbf{I}}/2k^2, & i = j. \end{cases} \quad (5.13)$$

One can define vectors containing the electric fields, both total and incident, in every cell as

$$\mathbf{E}_x = [E_{x,1} \quad E_{x,2} \quad \dots \quad E_{x,N}]^T, \quad (5.14)$$

$$\mathbf{E}_{0,x} = [E_{0,x,1} \quad E_{0,x,2} \quad \dots \quad E_{0,x,N}]^T, \quad (5.15)$$

and similar vectors can be created for $\mathbf{E}_{0,y}$ and \mathbf{E}_y . Matrices for the Green's tensor can also be defined as $\overline{\overline{\mathbf{G}}}_{xy}$, where each matrix element is of the form $G_{xy,i,j} = \hat{\mathbf{x}} \cdot \overleftrightarrow{\mathbf{G}}_{i,j} \cdot \hat{\mathbf{y}}$. Equivalent matrices are defined for indices: (xx) , (yy) and (yx) . By defining dielectric constant matrices, $\overline{\overline{\boldsymbol{\varepsilon}}}_{xy}$, as diagonal matrices with elements $\varepsilon_{xy,i} = \hat{\mathbf{x}} \cdot \overleftrightarrow{\boldsymbol{\varepsilon}}_i \cdot \hat{\mathbf{y}}$. Again equivalent matrices with indices: (xx) , (yy) and (yx) , are also defined. Applying all of these definitions, equation (5.6) can be rewritten in matrix form, resulting in

$$\left(\overline{\overline{\mathbf{I}}} - \begin{bmatrix} \overline{\overline{\mathbf{G}}}_{xx} & \overline{\overline{\mathbf{G}}}_{xy} \\ \overline{\overline{\mathbf{G}}}_{yx} & \overline{\overline{\mathbf{G}}}_{yy} \end{bmatrix} k_0^2 \left(\begin{bmatrix} \overline{\overline{\boldsymbol{\varepsilon}}}_{xx} & \overline{\overline{\boldsymbol{\varepsilon}}}_{xy} \\ \overline{\overline{\boldsymbol{\varepsilon}}}_{yx} & \overline{\overline{\boldsymbol{\varepsilon}}}_{yy} \end{bmatrix} - \overline{\overline{\mathbf{I}}} \varepsilon_{\text{ref}} \right) \right) \begin{bmatrix} \mathbf{E}_x \\ \mathbf{E}_y \end{bmatrix} = \begin{bmatrix} \mathbf{E}_{0,x} \\ \mathbf{E}_{0,y} \end{bmatrix}. \quad (5.16)$$

Solving equation (5.16) results in the electric field in a given area, this area should be chosen to include the scatterer so that one can use equation (3.17) to find the field in all other positions.

5.3 Applying the Fast Fourier Transform

The matrix equation, (5.16), must now be solved. However, the matrix in question scales in size as N^2 , where N is the number of discretization elements. Furthermore, by applying matrix inversion the calculation time will scale as N^3 [10]. This results in limitations for the size of the numerical problem, N , as one will run out of memory or the calculation time becomes too long for practical purposes. Therefore, a more efficient method is needed that scales better with N .

A more efficient method would be to first use the Fast Fourier Transformation (FFT) algorithm. Considering the main problem of a scatterer placed on a surface, FFT can be applied due to the Green's tensor being of the form;

$$\vec{\mathbf{G}}(\mathbf{r}, \mathbf{r}') = \vec{\mathbf{G}}^{(d)}(x - x', y - y') + \vec{\mathbf{G}}^{(i)}(x - x', y + y'). \quad (5.17)$$

This results in the Green's function integral equation (3.17) becoming two convolution integrals. Convolution integrals are a type of integral which have the form

$$E(x, y) = \int f(x - x', y - y')h(x', y')dx'dy'. \quad (5.18)$$

Following the convolution theorem, which can be found in Ref. [26], the calculation-heavy convolution integral can be found as a simple product in reciprocal space, i.e.

$$\tilde{E}(k_x, k_y) = \tilde{f}(k_x, k_y)\tilde{h}(k_x, k_y). \quad (5.19)$$

Using this, the convolution integral in equation (5.18) can be solved by Fourier-transforming both f and h and doing the product of the two and then inverse Fourier-transforming back into real space, resulting in

$$E(x, y) = \frac{1}{(2\pi)^2} \int \tilde{f}(k_x, k_y)\tilde{h}(k_x, k_y)e^{ik_x x}e^{ik_y y}dk_x dk_y. \quad (5.20)$$

It should be noted that it is not necessarily a faster approach to Fourier transform back and forth, however, if the FFT algorithm is used it can save a lot of calculation time. This is because the FFT algorithm scales as $N \log N$ [27][28] and is thus significantly less dependent on the size of N . So in summary this provides a way to make calculations for large and finely discretized structures.

For the next step the square discretization of the Green's function integral equation, (5.6), is redefined so that it makes use of an extra index, resulting in

$$\mathbf{E}_{i_x, i_y} = \mathbf{E}_{0, i_x, i_y} + \sum_{j_x, j_y} \left(\overline{\mathbf{G}}_{i_x - j_x, i_y - j_y}^{(d)} + \overline{\mathbf{G}}_{i_x - j_x, i_y + j_y}^{(i)} \right) \cdot k_0^2 (\overline{\mathbf{\epsilon}}_{j_x, j_y} - \overline{\mathbf{I}}_{\text{ref}}) \cdot \mathbf{E}_{j_x, j_y}, \quad (5.21)$$

$$\text{where } \mathbf{E}_{i_x, i_y} = [E_{i_x, i_y}^{(x)} \quad E_{i_x, i_y}^{(y)}]^{(T)}, \quad \text{and } \mathbf{E}_{0, i_x, i_y} = [E_{0, i_x, i_y}^{(x)} \quad E_{0, i_x, i_y}^{(y)}]^{(T)}.$$

The Green's matrix, denoted as $\overline{\mathbf{G}}_{i_x, j_x, i_y, j_y} = \overline{\mathbf{G}}_{i_x - j_x, i_y - j_y}^{(d)} + \overline{\mathbf{G}}_{i_x - j_x, i_y + j_y}^{(i)}$, and the dielectric matrix $\overline{\mathbf{\epsilon}}_{j_x, j_y}$, are in this case of the form

$$\overline{\mathbf{G}}_{i_x, j_x, i_y, j_y} = \begin{bmatrix} G_{i_x, j_x, i_y, j_y}^{(xx)} & G_{i_x, j_x, i_y, j_y}^{(xy)} \\ G_{i_x, j_x, i_y, j_y}^{(yx)} & G_{i_x, j_x, i_y, j_y}^{(yy)} \end{bmatrix}, \quad \text{and } \overline{\mathbf{\epsilon}}_{j_x, j_y} = \begin{bmatrix} \epsilon_{j_x, j_y}^{(xx)} & \epsilon_{j_x, j_y}^{(xy)} \\ \epsilon_{j_x, j_y}^{(yx)} & \epsilon_{j_x, j_y}^{(yy)} \end{bmatrix}. \quad (5.22)$$

One can now separate equation (5.21) into an x -component and a y -component. This results in

$$E_{i_x, i_y}^{(x)} - \sum_{j_x, j_y} k_0^2 \left[\left(G_{i_x, j_x, i_y, j_y}^{(xx)} (\varepsilon_{j_x, j_y}^{(xx)} - \varepsilon_{\text{ref}}) + G_{i_x, j_x, i_y, j_y}^{(xy)} \varepsilon_{j_x, j_y}^{(yx)} \right) E_{i_x, i_y}^{(x)} + \left(G_{i_x, j_x, i_y, j_y}^{(xy)} \varepsilon_{j_x, j_y}^{(xy)} + G_{i_x, j_x, i_y, j_y}^{(yy)} (\varepsilon_{j_x, j_y}^{(yy)} - \varepsilon_{\text{ref}}) \right) E_{i_x, i_y}^{(y)} \right] = E_{0, i_x, i_y}^{(x)}, \quad (5.23)$$

and

$$E_{i_x, i_y}^{(y)} - \sum_{j_x, j_y} k_0^2 \left[\left(G_{i_x, j_x, i_y, j_y}^{(yy)} (\varepsilon_{j_x, j_y}^{(yy)} - \varepsilon_{\text{ref}}) + G_{i_x, j_x, i_y, j_y}^{(yx)} \varepsilon_{j_x, j_y}^{(xy)} \right) E_{i_x, i_y}^{(y)} + \left(G_{i_x, j_x, i_y, j_y}^{(yx)} \varepsilon_{j_x, j_y}^{(yx)} + G_{i_x, j_x, i_y, j_y}^{(xy)} (\varepsilon_{j_x, j_y}^{(xx)} - \varepsilon_{\text{ref}}) \right) E_{i_x, i_y}^{(x)} \right] = E_{0, i_x, i_y}^{(y)}. \quad (5.24)$$

For each of these components, one can define two operators that transform a sum of $\overline{\mathbf{E}}^{(x)}$ and $\overline{\mathbf{E}}^{(y)}$ into either $\overline{\mathbf{E}}_0^{(x)}$ or $\overline{\mathbf{E}}_0^{(y)}$, so that

$$\hat{C}_x \overline{\mathbf{E}}^{(x)} - \hat{C}'_x \overline{\mathbf{E}}^{(y)} = \overline{\mathbf{E}}_0^{(x)} \quad \text{and} \quad \hat{C}_y \overline{\mathbf{E}}^{(y)} - \hat{C}'_y \overline{\mathbf{E}}^{(x)} = \overline{\mathbf{E}}_0^{(y)}. \quad (5.25)$$

When it comes to applying these operators element-wise multiplication is used. This is denoted by $\overline{\mathbf{A}} * \overline{\mathbf{B}}$ and means that element (α, β) in the resulting matrix is found by multiplying element (α, β) of matrix $\overline{\mathbf{A}}$ with element (α, β) of matrix $\overline{\mathbf{B}}$. The matrices with the values of the Green's functions and the matrices containing the product of the dielectric function and the electric field are both Fourier transformed by applying the FFT algorithm. From here the product of these are completed in reciprocal space and thereafter it is transformed back into real space. Applying this, the operators for the x -component in (5.25) becomes;

$$\hat{C}_x \overline{\mathbf{E}}^{(x)} = \overline{\mathbf{E}}^{(x)} - IFFT \left[FFT \left(\overline{\mathbf{G}}^{(xx)} \right) * FFT \left(k_0^2 (\overline{\varepsilon}^{(xx)} - \overline{\mathbf{I}}_{\varepsilon_{\text{ref}}}) * \overline{\mathbf{E}}^{(x)} \right) - FFT \left(\overline{\mathbf{G}}^{(xy)} \right) * FFT \left(k_0^2 \overline{\varepsilon}^{(yx)} * \overline{\mathbf{E}}^{(x)} \right) \right], \quad \text{and} \quad (5.26)$$

$$-\hat{C}'_x \overline{\mathbf{E}}^{(y)} = IFFT \left[FFT \left(\overline{\mathbf{G}}^{(xx)} \right) * FFT \left(k_0^2 \overline{\varepsilon}^{(xy)} * \overline{\mathbf{E}}^{(y)} \right) + FFT \left(\overline{\mathbf{G}}^{(xy)} \right) * FFT \left(k_0^2 (\overline{\varepsilon}^{(yy)} - \overline{\mathbf{I}}_{\varepsilon_{\text{ref}}}) * \overline{\mathbf{E}}^{(y)} \right) \right]. \quad (5.27)$$

Similar operators are found for the y -component. An important detail is that every matrix with values of Green's functions are of the size $(2N_x - 1) \times (2N_y - 1)$, where N_x and N_y are the amount of elements in the x and y directions, and the $\overline{\mathbf{E}}$ and $\overline{\varepsilon}$ matrices are of the size $N_x \times N_y$. Therefore, the matrices must be zero-padded so that it has the same size as the Green's function matrices before the FFT algorithm is applied. After the inverse FFT has been applied, one must take the appropriate submatrix of size; $N_x \times N_y$.

The last step is to solve both components in equation (5.25), which can be done using an iterative method. The method used in this report is the conjugate gradient algorithm, which can be found in Appendix B of Ref. [10]. The algorithm requires an initial guess,

in this case the guesses are chosen to be $\overline{\overline{\mathbf{E}}}_0^{(x)}$ and $\overline{\overline{\mathbf{E}}}_0^{(y)}$, that is then iteratively improved until it is satisfactory according to a convergence criteria. In this report, the convergence criteria is chosen to be acceptable when the error, as described in the definition of the conjugate gradient algorithm, is below 10^{-10} .

The same method have been applied to the three dimensional case, this results in equations of the general form;

$$\begin{aligned} \mathbf{E}_{0,j_x,j_y,j_z} = \mathbf{E}_{i_x,i_y,i_z} - \sum_{j_x,j_y,j_z} \overline{\overline{\mathbf{G}}}_{i_x-j_x,i_y-j_y,i_z-j_z}^{(d)} k_0^2 (\varepsilon_{j_x,j_y,j_z} - \varepsilon_{\text{ref}}) \cdot \mathbf{E}_{j_x,j_y,j_z} \\ - \sum_{j_x,j_y,j_z} \overline{\overline{\mathbf{G}}}_{i_x-j_x,i_y-j_y,i_z+j_z}^{(i)} k_0^2 (\varepsilon_{j_x,j_y,j_z} - \varepsilon_{\text{ref}}) \cdot \mathbf{E}_{j_x,j_y,j_z}. \end{aligned} \quad (5.28)$$

Chapter 6

Analysis of Results in Two Dimensions

Following the theoretical structure, a method for efficiently calculating the electric field inside and outside of a fiber on a silver film on quartz has been developed and an analysis can now be conducted. Several aspects of the setup with a nanofiber on a silver film over quartz are interesting to examine, such as how efficient the fiber is at exciting plasmons dependent on its size or thickness of the silver film. This chapter aims to examine as many of these aspects as possible all while providing context and hypothesizing what is the cause of the effects that are examined. However, to start one must test how well the model converges.

6.1 Convergence of the Model

Convergence is tested in order to confirm how many discretization elements are needed for the model to be rigid and provide consistent results. In order to discuss how many elements is needed, a clear definition of the amount of elements is required. Therefore, the variable N_d is introduced, which describes the amount of points per 100 nm for a single axis in the fiber. For example, if one needs a 200 nm high and 400 nm wide fiber that is discretized so that $dx = dy = 5$ nm, dx and dy being the size of the sides of the discretization elements, 40 cells would be needed in the y -axis and 80 cells in the x -axis. This makes $N = 3200$ for the fiber and would be described as having $N_d = 20$. In summary, a $N_d = 10$ corresponds to a $dx = 10$ nm and a $N_d = 40$ corresponds to a $dx = 2.5$ nm.

To test convergence, a fiber with a height of 100 nm and a width of 100 nm, denoted 100×100 nm², is chosen and the method is applied with an incident wave with an incident wavelength of 390 nm, as well as the doubled wavelength, 780 nm. For the same setup, different discretizations are applied to see the effect of a higher or a lower N_d . In order to quantify the difference, the maximum value of the plasmon peaks is observed so to see the change dependent on N_d .

To start the incident wavelength of 390 nm is examined. In the left part of figure 6.1, one can see the downwards differential scattering cross section, σ_{diff} , for a fiber with a discretization of $N_d = 40$. Here one can see the two plasmon peaks that were predicted, however, they appear wider than expected. The right plot shows a convergence plot for

the scenario, where the value of σ_{diff} at the top of the peaks is shown for different N_d .

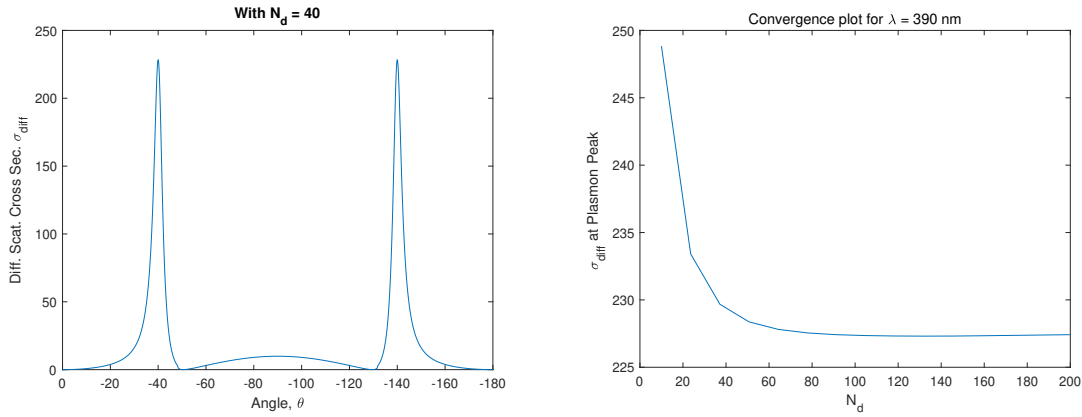


Figure 6.1. The left plot shows the downwards differential scattering cross section at different angles, where the two peaks at the plasmon angles are visible. The right plot is a convergence plot that shows the evolution of value of σ_{diff} in one of the plasmon peaks when N_d becomes larger.

From the convergence plot it appears that it converges towards a single value for higher N_d . Since the calculation time of the program scales significantly with the size of N_d , it is preferred to choose as small a value as possible for N_d that is still sufficient. For $N_d = 20$ the peak value is at 233.4 nm, for $N_d = 40$ it is 228.4 nm and for $N_d = 200$ it becomes 227.3 nm. This value appears to be close to a converged value and therefore a percent deviation between $N_d = 200$ and $N_d = 20$ as well $N_d = 40$ are calculated, and results in a deviation of 2.69% and 0.48% respectively. To further see the difference between the different discretizations, a plot that focuses on only one of the plasmon peaks are made where all three discussed values are used. This is seen in figure 6.2.

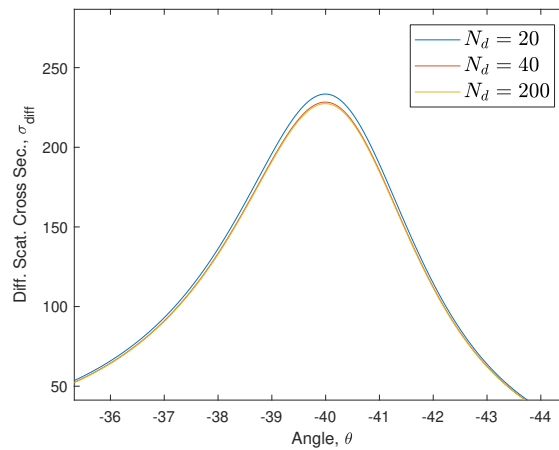


Figure 6.2. Three plots, with different N_d , of the σ_{diff} for the 100×100 fiber with an incident wavelength of 390 nm. However, here it is limited to only the left plasmon peak, in order to properly examine the the difference cause by N_d .

In the figure there does not appear to be a significant difference between using an N_d of 40 or 200 as the two lines are placed almost on top one another, as thus so far an N_d of 40 seems appropriate to use going forward.

An additional incident wavelength that will be thoroughly examined is the doubled wavelength; 780 nm. Again a fiber of size $100 \times 100 \text{ nm}^2$ is used, so in figure 6.3 two similar plot to figure 6.1 are made, however, using another wavelength.

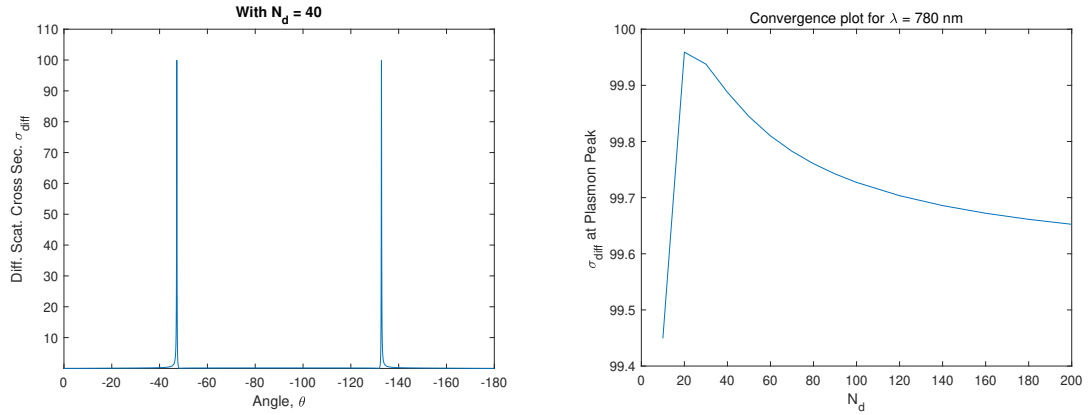


Figure 6.3. Here the right plot is a convergence plot that shows the evolution of value of σ_{diff} in one of the plasmon peaks when N_d becomes larger. The left plot shows σ_{diff} at different angles, here the two plasmon peaks are clearly visible and very defined.

Again the two plasmon peaks are present, however, for this wavelength the peaks are much more defined. Initially looking at the convergence plot it appears to vary more drastically than for the 390 nm wavelength. However, values vary on a significantly lower scale. It seem that after $N_d = 20$ the values start to drop and goes towards a single converged value, much like the previous example, though for $N_d = 200$ it does not appear to have reached it yet. Comparing the discretization with $N_d = 40$ with one with $N_d = 200$, the percent deviation is only 0.24 %, which is an even smaller difference then for the 390 nm incident wavelength.

It makes sense that for a higher wavelength a lower N_d is needed for sufficient results, as the lower frequency incident wave would result in less variance in the electric field inside the fiber.

In general an N_d of 40 appear to be sufficient for the purposes of this report and is also low enough to be able to examine a lot more complicated scenarios without the calculation time becoming too problematic. Therefore, $N_d = 40$ is used as a standard for the remainder of the report.

6.2 Effective Dimensions of a Fiber for Plasmon Excitation

In reference [10], it is mentioned that changing the size of the fiber results in a significant difference in ability to excite plasmons. From Ref. [5] a fiber with a width of 350 nm and a height of 100 nm was analyzed in relation to SPP excitation. In Ref. [10], it is shown that a fiber that is 100 nm high, 100 nm wide and 400 nm long is significantly better at exciting SPPs, than the one describe in Ref. [5]. this is hypothesized to be an effect of destructive interference outside of the fiber, by the SPPs at the air-silver interface. This seems to be the case that was found in Ref. [5], since a width of 350 nm matched the mode wavelength at the air-silver interface, which is $\lambda_{\text{SPP}} = 390 \text{ nm}/1.1607 \approx 336 \text{ nm}$. It is then hypothesized that when the fiber matches the SPP mode wavelength for the

air-silver interface, the resulting SPP-related peaks will be extinguished. This concept is shown in figure 6.4. Thereafter, for every period of $2\lambda_{\text{SPP}}$, the same conditions are met for destructive interference, thus the SPP-related peaks will be extinguished whenever the fiber width is an odd integer times λ_{SPP} .

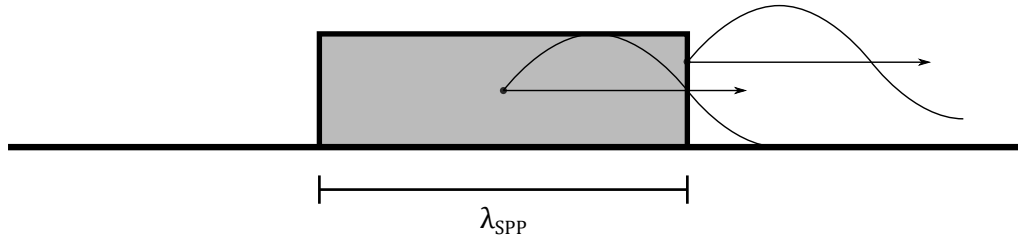


Figure 6.4. Illustration of the idea that a specific width for a fiber will result in minimum plasmon excitation.

The hypothesis in question is one that would be quite interesting to confirm or deny, and it would perhaps lead to a simple and rigid model for how well one can expect a given fiber to excite plasmons. So for the two wavelengths, 390 nm and 780 nm, the scattering is calculated for many different heights and widths. For the purpose of this initial examination, the thickness of the silver film will remain constant at 40 nm.

6.2.1 Effect of the Width of the Fiber

Initially the effects of the width of the fiber is examined, thus for this initial analysis the height is then kept at a constant value. First, the case of an incident wave with a 390 nm wavelength is studied.

Incident Wave with Significant Loss

The first thing that is examined, is a fiber with a height and width of 100 nm for the 390 nm incident wavelength. As found in section 2.2, for the case with 390 nm wavelength incident wave the angles at which the SPP leaks are expected to be -39.26° and -140.74° .

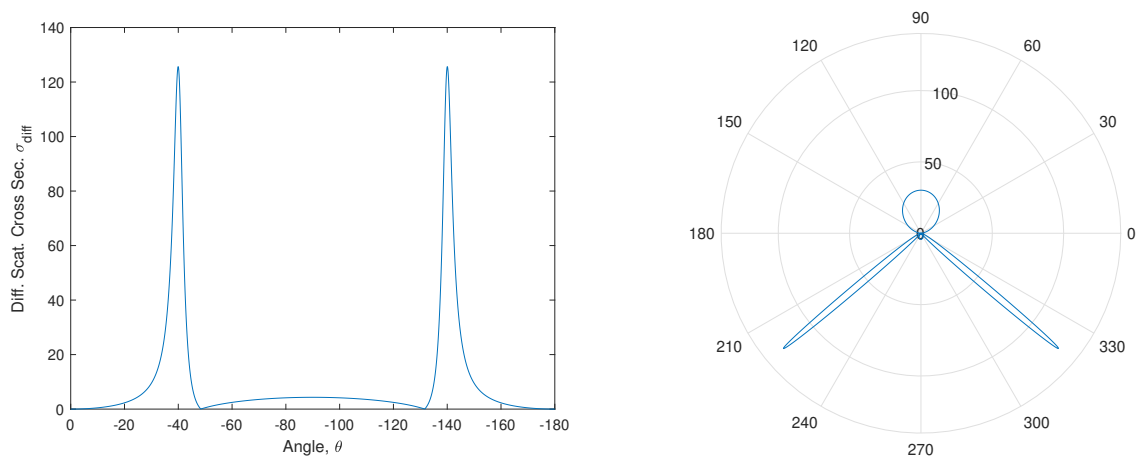


Figure 6.5. Far field plots for a fiber of size $100 \times 100 \text{ nm}^2$ for an incident wave with a 390 nm wavelength. The left plot is for the downwards differential scattering cross section and the right shows a polar plot of the differential scattering cross section for all angles.

In figure 6.5, a downwards differential scattering cross section plot of a fiber that is 100 nm high and 100 nm wide as well as a polar plot showing the scattering in every direction. For this fiber the plasmon peaks are very clear, with limited scattering in other downwards directions. The plasmon peaks are also found at angles -39.96° and -140.10° , which are very near to the angles at which they were expected to appear. The upwards scattering is not focused at specific angles as the plasmons are, however, a significant amount of the intensity is still scattered in the upwards direction.

As mentioned in the previous section, for an incident wavelength of 390 nm the peaks are much wider than for its 780 nm counterpart where the peaks are very defined at the predicted angles, this is seen in figure 6.3. This finite width of the peaks is related to the propagation loss of the SPP and is a result of absorption into the silver film [5]. For higher wavelength, however, this effect is greatly diminished.

To get a more holistic view of the scattering, the electric field around the fiber is also calculated, and in figure 6.6 a plot of the absolute value of the real part of E_y is presented. The y -component is chosen since it must be a result of the scattering by the fiber; the incoming field does not oscillate in y , and since the incoming field is much stronger than the scattered field. The near field image of the y -component of the electric field thus shows what is relevant.

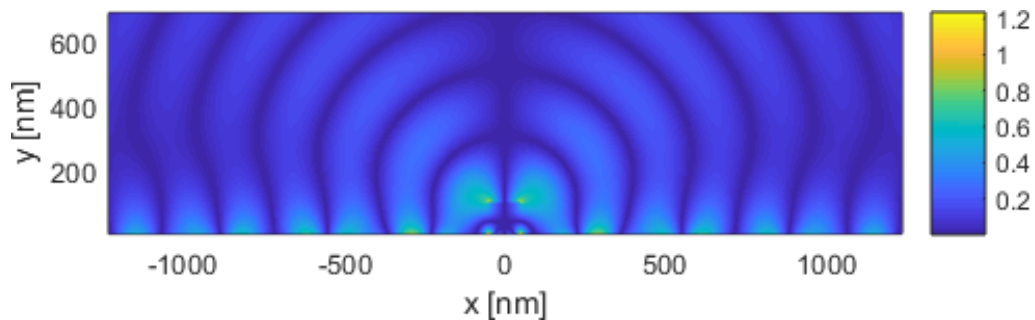


Figure 6.6. The absolute value of real part of the y -component of the electric field is shown in- and outside of the scatterer. The scatterer here is of size $100 \times 100 \text{ nm}^2$ and the incident wave has the wavelength 390 nm.

In the figure, one can see that the field is scattered upwards in every direction. One is also able to see a plasmon following the air and silver interface, as the field is stronger near this interface. However, it is difficult to differentiate between the surface plasmon and scattered field.

To further examine the fiber, it is kept at a height of 100 nm but the width is changed from 50 nm to 2000 nm with a 50 nm interval. This is represented in two ways and both can be seen in figure 6.7. For the left plot the differential scattering cross section at the peak of one of the plasmon peaks is plotted dependent on the size of the width of the fiber. For the right plot, however, an integral is calculated for the peaks. The resolution for the downwards scattered plot is chosen to consist of 10 000 points, so for the purposes of integrating over a peak, the point at which the peak is the highest is chosen and the integral is then started 100 values prior and ends 100 after the top point of the peak

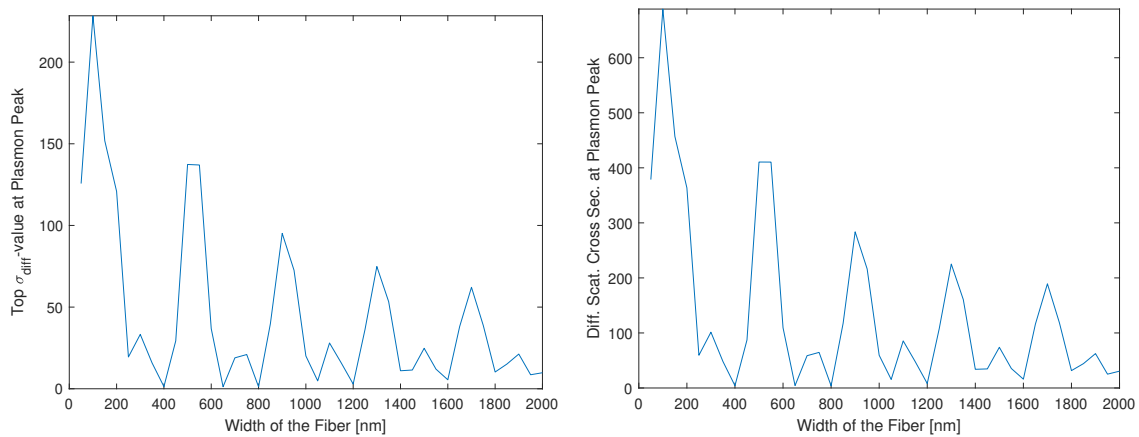


Figure 6.7. Plot of the value of σ_{diff} at the top point of the plasmon peaks, but for different fibers with varying widths. The right plot shows the same, however, the y -axis is found by integrating around the peaks.

The first feature one notices is the oscillating tendency of the values, going back and forth between being good and poor at exciting plasmons. An important note is also that it seems that at every width that is near an integer of 400 nm the fiber hits a low point of exciting plasmons, e.g. at 400 nm, 800 nm, 1200 nm, 1600 nm, etc. This is close to the incident wavelength, however, does not relate with the plasmon wavelength for either the silver-air interface or fiber-silver interface, which are 336.2 nm and 129.7 nm respectively. However, by expanding the fiber by only 100 nm in width results in a fiber that again is great at exciting plasmons. Furthermore, there appears to consistently be a smaller peak in σ_{diff} between each of these bigger peaks, which is interesting and might suggest that multiple factors determine if a fiber is effective at exciting plasmons. Another tendency that is observed is that it appears that the overall effectiveness for exciting plasmons slowly diminishes for wider fibers.

To examine a fiber with diminished plasmon excitation, the resulting downwards scattering for a fiber with a width of 400 nm is also shown in the right plot of figure 6.8.

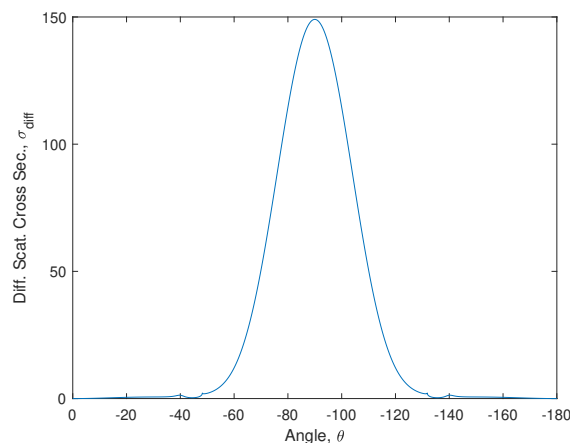


Figure 6.8. This plot shows an example of a fiber width that results in an extinction of the plasmon peaks, in this example this width is 400 nm.

Here it is clear that there are simply no clear peaks at the leakage angles. The transmitted

intensity in the middle is also significantly larger than for the $100 \times 100 \text{ nm}^2$ fiber, however, further examination shows that this appears to be a general effect for wider fibers. Additionally, a corresponding near field plot has also been calculated and is shown in figure 6.9.

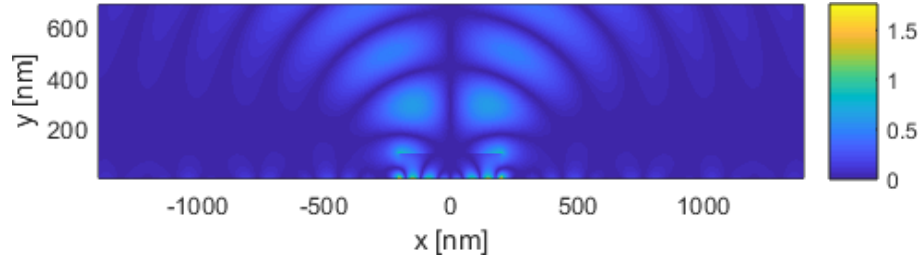


Figure 6.9. The absolute value of real part of the y -component of the electric field is shown in- and outside of the scatterer. The scatterer here is of size $100 \times 400 \text{ nm}^2$ and the incident wave has the wavelength 390 nm .

Here it is clear that there are no, or at least not very many, plasmons that are excited and propagate along the air-silver interface, as they are much weaker than for the previous example. This shows that it is in fact possible to extinguish plasmon excitation for specific widths.

Examining the far fields of wider fibers, one finds that the transmitted light, that does not correspond to plasmons, becomes much stronger and with more complex scattering pattern. Two such examples are shown in figure 6.10, where the far fields for fibers with widths of 600 nm and 1700 nm are used.

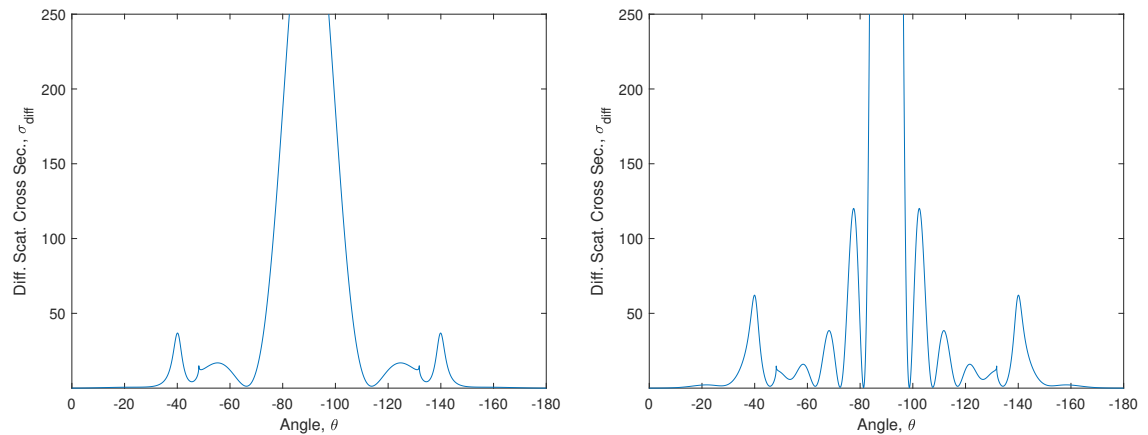


Figure 6.10. Far field plots for fibers of size $100 \times 600 \text{ nm}^2$ (left plot) and $100 \times 1700 \text{ nm}^2$ (right plot), for an incident wave with a 390 nm wavelength.

The axis is limited to a max of 250 nm for σ_{diff} in order to still be able to see the peaks for the plasmons, however, for the 600 nm wide fiber, the transmitted beam in the middle reaches a peak value of 355 nm , and for the 1700 nm wide fiber it reaches 2641 nm . This is a general observation, that for wider fibers more complex transmitted scattering pattern appears. This is most likely due to interference of the transmitted field.

Incident Wave without Significant Loss

The other examined wavelength of 780 nm is also applied to the same fiber with a width and height of 100 nm. A plot for the downwards σ_{diff} is presented in figure 6.11, together with the corresponding polar plot.

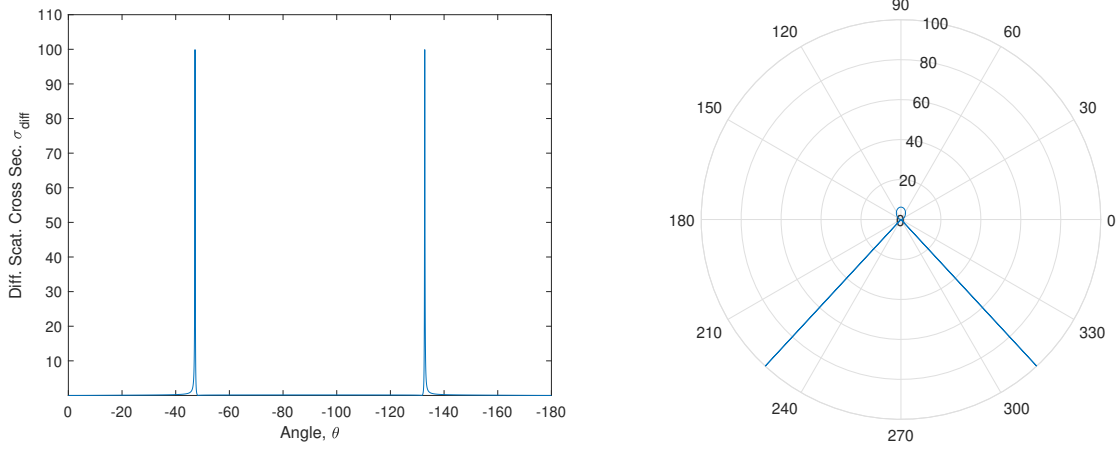


Figure 6.11. Far field plots for a fiber of size $100 \times 100 \text{ nm}^2$ for an incident wave with a 780 nm wavelength. The left plot is for the downwards differential scattering cross section and the right shows a polar plot of the differential scattering cross section for all angles.

Initially it is observed that the plasmon peaks are much more defined and also the maximum value of the peaks is slightly smaller. The much more defined peaks are a result of the lower frequency which results in much lower SPP propagation loss as mentioned. In order to truly see the difference in ability to excite plasmons between the two examples, the integral taken over the peaks for both the 390 nm and 780 nm incident wave is made. From doing this integral it is found that

$$390 \text{ nm incident wave: } \sigma_{\text{diff,peak}} = 885.3 \text{ nm, and}$$

$$780 \text{ nm incident wave: } \sigma_{\text{diff,peak}} = 28.6 \text{ nm.}$$

So for the 780 nm wavelength, there are significantly fewer plasmons that are excited even though it would appear that a similar amount is present looking at the peak value of the peaks. So one need to be cognizant of the widths of the peaks, and also be able to evaluate how much should be integrated when checking the plasmon power. For now, the method of integrating 100 value prior and after the peak is applied.

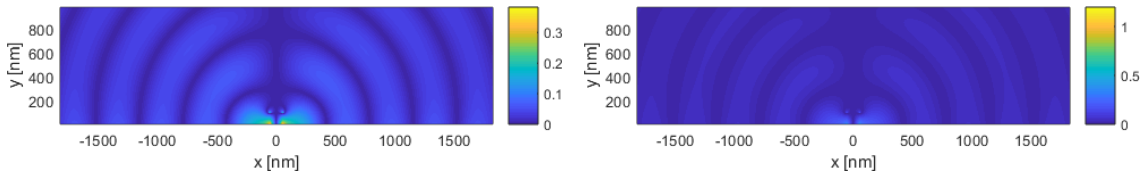


Figure 6.12. The absolute value of real part of the y -component of the electric field is shown in- and outside of the scatterer. The scatterer here is of size $100 \times 100 \text{ nm}^2$ and the incident wave has the wavelength 780 nm. For the right plot the colorbar has been expanded to correspond directly with figure 6.6.

To examine how the near field behaves for the scenario of a 780 nm wavelength incident wave, a plot is made and presented in figure 6.12. Initially, when examining the left plot it appears very similar for to figure 6.6, however, when the scale of the colorbar is expanded to the same scale, as in figure 6.6, it becomes clear that for this wavelength the same fiber scatter much less of the wave.

Following the same analysis method as for the 390 nm incident wave, a plot of the σ_{diff} around plasmon peaks for different widths of the fiber is carried out and shown in figure 6.13.

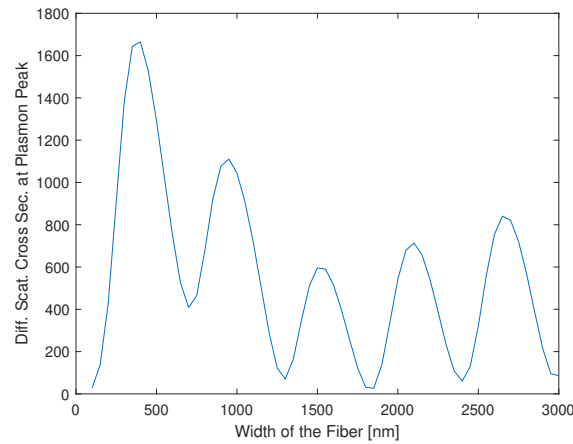


Figure 6.13. Integral of σ_{diff} around plasmon peaks for different widths of a fiber that is 100 nm high, with an incident wavelength of 780 nm.

For the purposes of this figure the width was expanded to 3000 nm, so to compensate for the longer wavelength. This figure is somewhat similar to figure 6.7, however, with a few key differences. This figure also oscillates, but does not have minor peaks between bigger peaks. Furthermore, for this figure the first peaks also appear to be the most effective, however, the peaks does not appear to have a simple trajectory of slowly becoming less effective for wider fibers, as it appears that the peaks again becomes better for even wider fibers. Examining the individual far field plots reveals that, similarly to 390 nm, the transmitted beam in the middle becomes stronger for wider fibers, however, the scattering pattern for this beam does not become more complex as for 390 nm. Furthermore, the period between peaks also corresponds very well with the wavelength of the SPP inside of the fiber, which has a wavelength of 560 nm for a 100 nm high fiber.

Unlike for 390 nm, where the first and most prominent peak was present at 100 nm, meaning around a quarter incident wavelength. the first and most prominent peak is present at around 400 nm, meaning at around half an incident wavelength. Furthermore, for this case the width where the plasmon peaks are extinguished are as follows; 700 nm, 1300 nm, 1825 nm and 2400 nm. This is also something that varies from earlier, as it does not follow an integer value of incident wavelength and also the difference between them varies, as the differences are; 700 nm, 600 nm, 525 nm and 575 nm, which was not the case previously.

Looking at the far field plots for the different widths, the scattering pattern does not significantly alter apart from the change in plasmon peak size. An example of this can be found in figure 6.14, where the scattering pattern of the fiber with a height of 100 nm and

a width of 400 nm is presented.

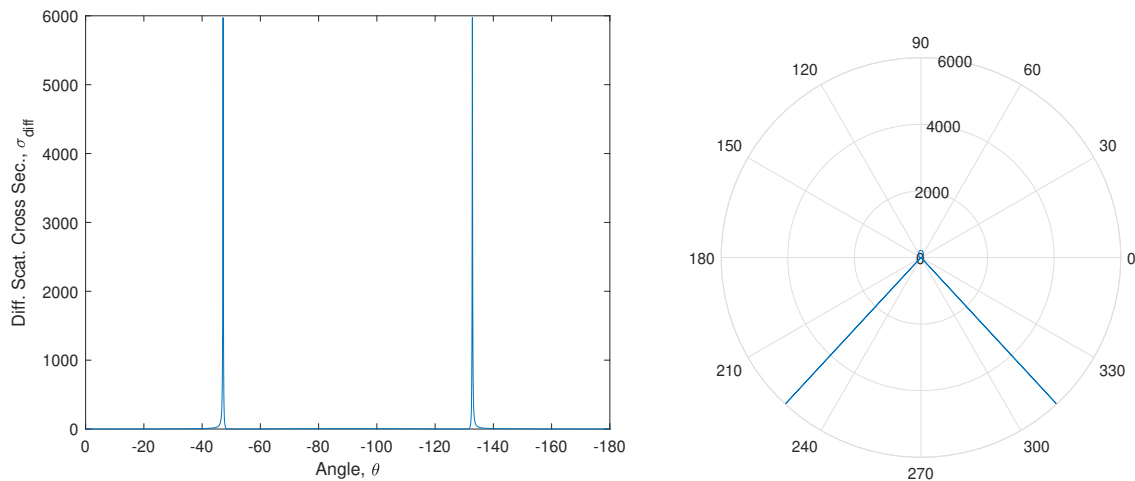


Figure 6.14. Far field plots for a fiber of size $100 \times 400 \text{ nm}^2$ for an incident wave with a 780 nm wavelength. The left plot is for the downwards differential scattering cross section and the right shows a polar plot of the differential scattering cross section for all angles.

This is a significantly better fiber at exciting plasmons for the 780 nm wavelength than a $100 \times 100 \text{ nm}^2$ fiber. It is worth noting that neither for this fiber is there any significant upwards scattering. To compare with the best fiber for 390 nm wavelength incident wave, an integral over one of the peaks is carried out, using the same method. This results in a $\sigma_{\text{diff,peak}}$ of 1665.2 nm, compared to the 885.3 nm for the 390 nm wavelength incident wave it is significantly larger. It would seem logical that a wavelength of 780 nm would be better, given that the propagation loss for the SPP is much lower, and therefore less plasmons will be absorbed before leaking into the quartz at the plasmon angle. However, it can be more difficult to evaluate how much of the peak for 390 nm one should integrate, so comparison between the two can be difficult. However, no matter the choice of integral boundaries, the 780 nm incident wave is still significantly better at exciting plasmons.

Additionally, a near field plot is made for the fiber examining quite a large area around the fiber.

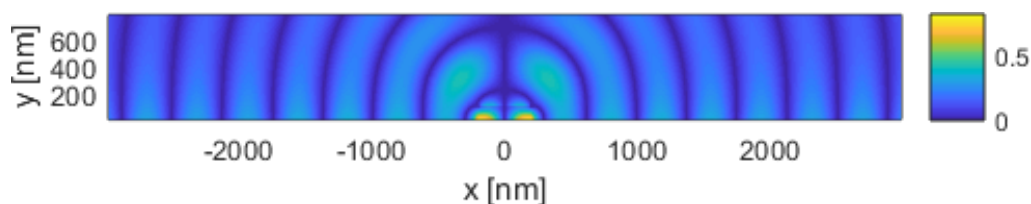


Figure 6.15. The absolute value of real part of the y -component of the electric field is shown in- and outside of the scatterer. The scatterer here is of size $100 \times 400 \text{ nm}^2$ and the incident wave has the wavelength 780 nm.

It is not quite possible to directly differentiate the surface plasmons from the rest of the scattered field. However, one can see that with a wavelength of 780 nm, loss does not appear to be a significant factor, as the field does not appear to diminish even at 3000 nm away from the fiber.

6.2.2 Effect of the Height of the Fiber

From what was initially assumed, most relevant feature of the dimensions of the fiber was the width, as it would cause inference between plasmons in both directions and extinguish the SPPs. This certainly seems to be the case, however, it would be interesting to see of the effectiveness of the fibers change when the height is changed.

Incident Wave with Significant Loss

First, the case of the 390 nm incident wave is considered with a fiber with a height of 200 nm. To inspect this difference, a plot of the integral around plasmon peaks for σ_{diff} with different widths is plotted. The resulting plot for a 200 nm high fiber is shown against the result obtained from figure 6.7. Both of these are shown in figure 6.16.

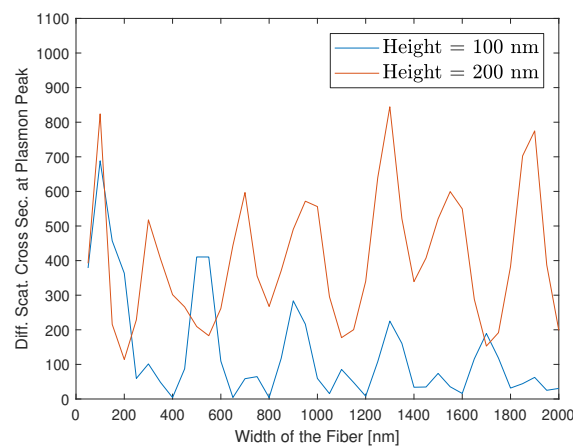


Figure 6.16. Plot of the value of σ_{diff} integrated around the plasmon peaks for fibers with different width, but fixed heights of 100 nm and 200 nm.

Examining the result, one will see a lot of difference between the two plots. One could suspect that the added height would not result in drastic changes in plasmon excitation. It would be logical that the width mostly determined the effectiveness of fiber for exciting plasmons, as the change in width would be assumed to have a larger effect on the wave following along the interface. However, the change in height has a significant impact on the plasmon excitation. Firstly, it notably improved overall plasmon excitation for most peaks. Secondly, the peaks are not necessarily in the same positions as for a 100 nm high fiber, as many large peaks are now present for widths that before did not provide great plasmon excitation, e.g. at around a 300 nm or 700 nm. Similarly at around a 500 nm width, where there were a peak for the 100 nm high fiber, is now one of the lowest points. And lastly, for a wider fiber the effectiveness of plasmon excitation does not seem to diminish as it was previously.

However, examining the result closer reveals that the result has been effected even further. In figure 6.17 two plots of the downwards σ_{diff} is shown. One where the height of the fiber is 100 nm and one where it is 200 nm, here the widths both vary from 50-2000 nm.

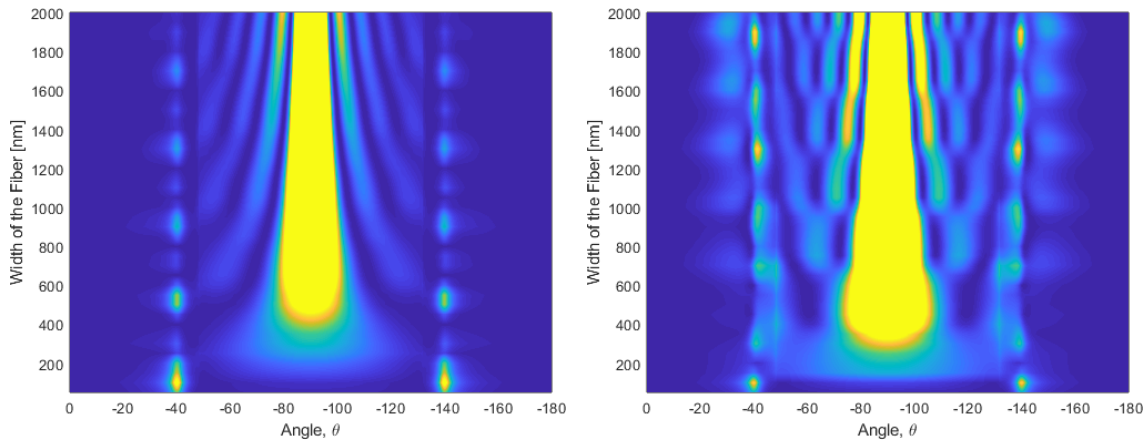


Figure 6.17. Downwards differential cross section for different widths. The left plot have a constant height of 100 nm and the right a constant height of 200 nm.

For the 100 nm high fiber, it is clear that the plasmon peaks are all present at the same leakage angle of around -39.26° and are not disrupted by other effects outside of the critical angle. However, for the 200 nm high fiber the image becomes much more messy and scattering beyond the critical angle clearly start to have an effect. If examined closely the different plasmon peaks also vary in position. For many of the larger peaks, at the -39° or -40° angles, the peak is actually at a minimum, but the peaks only a single angle away could be very large. An example of this is the scattering of a 200 nm high and 600 nm wide fiber shown in figure 6.18.

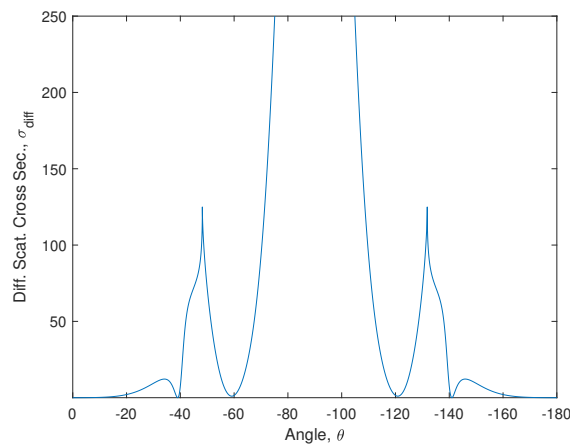


Figure 6.18. Downwards differential cross section for a fiber of size $200 \times 600 \text{ nm}^2$.

For this scattering pattern it can be difficult to distinguish what is an plasmon and what is not. At the exact plasmon leakage angle the value of σ_{diff} seems to drop to zero, however, the method of integrating used would not necessarily conclude that this fiber excites no plasmons, as it would include some of the effect close to it.

In general the added effects, together with a more complicated scattering pattern for wider fibers, results in more confusing images that make it hard to differentiate the plasmon peaks from other types of scattering. This is a problem when integrating for the plasmon peaks, as one can not easily determine where to integrate and if what is included is actually a plasmon.

Furthermore, the effects does not appear only for a 200 nm high fiber nor diminish for even higher fibers. In figure 6.19 two similar plots are presented, however for fibers that are 300 nm and 500 nm high.

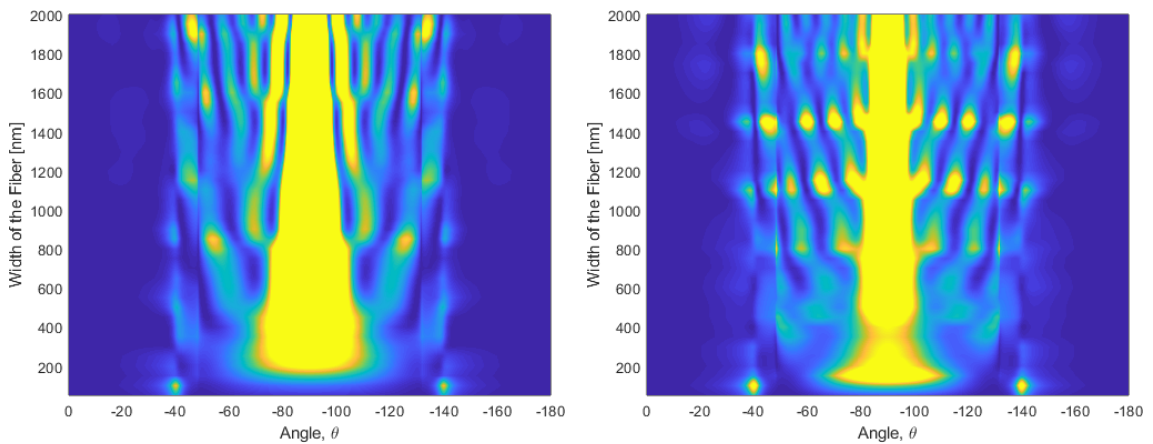


Figure 6.19. Downwards differential cross section for different widths. The left plot have a constant height of 300 nm and the right a constant height of 500 nm.

For these heights the scattering pattern appear to be just as, if not even more, complicated.

Given all this, is it correct to assume from figure 6.16 that there is no width where the plasmons completely diminish? Or is this just a result of included too much in the integration?

Returning to the example of a 200 nm high fiber, when examining the near field of fibers varying from 2000 nm to 50 nm in width, it can be seen that for any width there are always some clearly bound plasmons outside of the fiber. Such an example is shown in figure 6.20.

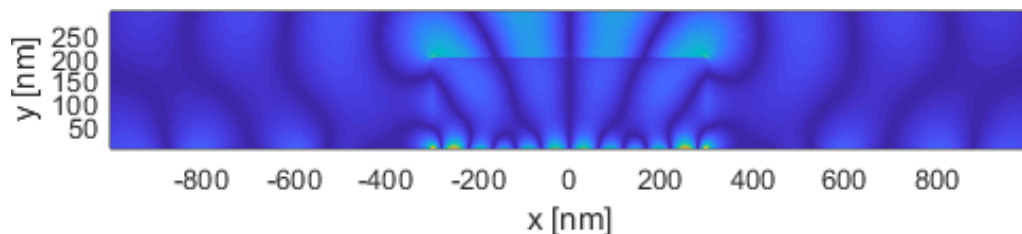


Figure 6.20. The absolute value of real part of the y -component of the electric field is shown in- and outside of the scatterer. Near field scattered by a fiber that is 200 nm high and 600 nm wide.

Here one can see that there is plasmons bound to the surface, and as mentioned this is the case for every width of the fiber, when it is 200 nm high. However, compared its 100 nm high counter part, this is not the case.

In figure 6.21 one can see an example where no or at least very little is bound to the surface. Another such example is given in figure 6.9 and more examples can be found for quite a few widths for a 100 nm high fiber. Of course this is not the case for every width, however, it does suggest that the fact that peaks, that are integrated over for the 200 nm high fiber in figure 6.16, does in fact not completely diminish at any point. Meaning that e.g. figure 6.18 does produce plasmons, despite the scattering showing that σ_{diff} is zero at exactly the predicted plasmon angle.

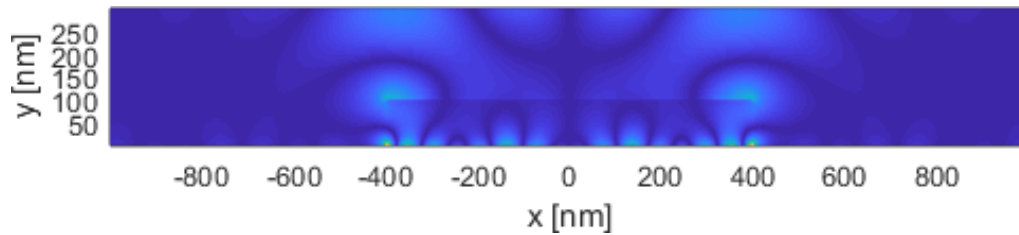


Figure 6.21. The absolute value of real part of the y -component of the electric field is shown in- and outside of the scatterer. Near field scattered by a fiber that is 100 nm high and 800 nm wide.

To further examine for different heights, a color plot is made in order to see the σ_{diff} around the plasmon peaks for all the calculated widths for all the calculated heights. This is shown in the left plot in figure 6.22.

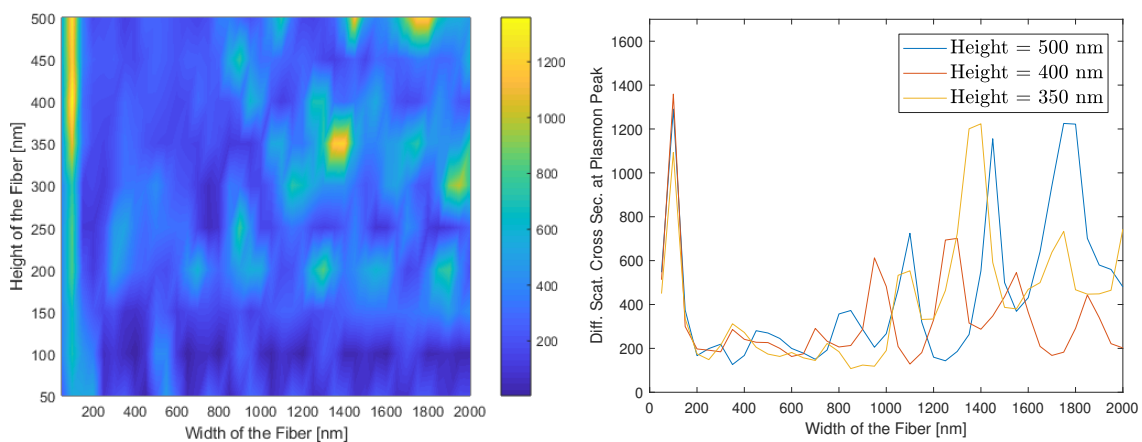


Figure 6.22. The left plot shows the σ_{diff} around the plasmon peaks for every calculated dimensions of the fiber. The right plot shows σ_{diff} around the plasmon peaks for every calculated width, however, only for three different heights; 350 nm, 400 nm and 500 nm.

From the colorplot one can see that some form of oscillation is present for every height, however, it appears that it varies for different heights. One thing to note is that it shows that the 100 nm high fiber is in general a quite poor fiber for exciting plasmons, as it is only really good at around 100 nm wide and it is one of the few heights where the exciting of plasmon completely diminish for certain widths. However, a 100 nm wide fiber is in general great at exciting plasmons no matter the height, although it does seem that for a higher fiber the 100 nm wide fiber becomes better, peaking at 400 nm high. Furthermore, it appears that this fiber is the best, with similar good excitation for a 350 nm high fiber and 500 nm high fiber.

To closer examine and find the best fiber for exciting plasmons a plot of σ_{diff} around the plasmon peaks for every width with heights 350 nm, 400 nm, and 500 nm is shown in figure 6.22. For these heights it appear that the simple oscillations have been swapped out for irregular peaks. As can be seen some of the best peaks are found when the fiber is 100 nm wide, however, for the 350 nm high fiber a comparable peak appear for a 1400 nm wide fiber. Additionally for a 500 nm high fiber, two peaks appear for a 1450 nm wide fiber and a 1750 nm wide fiber. In figure 6.23 the downwards σ_{diff} for two of the best fibers are shown.

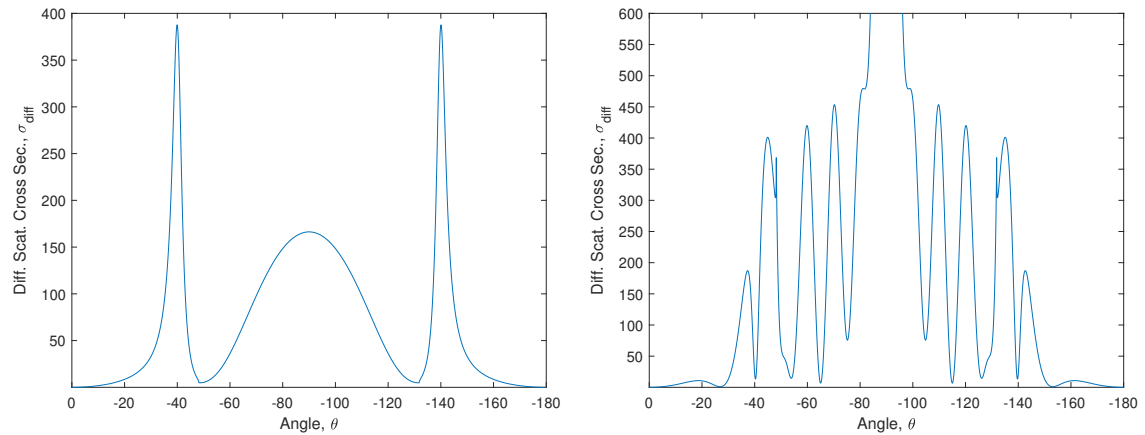


Figure 6.23. Plot of downwards scatter for fibers of sizes 400 nm high, 100 nm wide (left) and 500 nm high, 1450 nm wide (right).

For the fiber of size $400 \times 100 \text{ nm}^2$ the scattering pattern is still of the simple form as it was for a height of 100 nm. However, it has become more potent at exciting plasmons, as the plasmon peaks have become significantly higher, but not wider.

For the the $500 \times 1450 \text{ nm}^2$ fiber, the problem of it not being completely clear what is a plasmon and what is not is again present. In fact at the leakage angle there does not appear to be any peak, but due to the two high peaks next to it the integral become large.

Incident Wave without Significant Loss

The obvious next step is to examine the same effect, bur for the longer incident wavelength of 780 nm. For this wavelength loss is significantly less of a problem, this results in the $1/e$ decay length to become around $280 \mu\text{m}$ which, if compared to its 390 nm counterpart, is almost 100 times longer. The plasmons therefore have ample time to leak into the substrate before it is absorbed. This results in more focused and easily distinguishable plasmon peak and fewer effects that distort the scattering pattern. This can be seen in figure 6.24, where the downwards scattering for a fiber of size $700 \times 2850 \text{ nm}^2$ is shown.

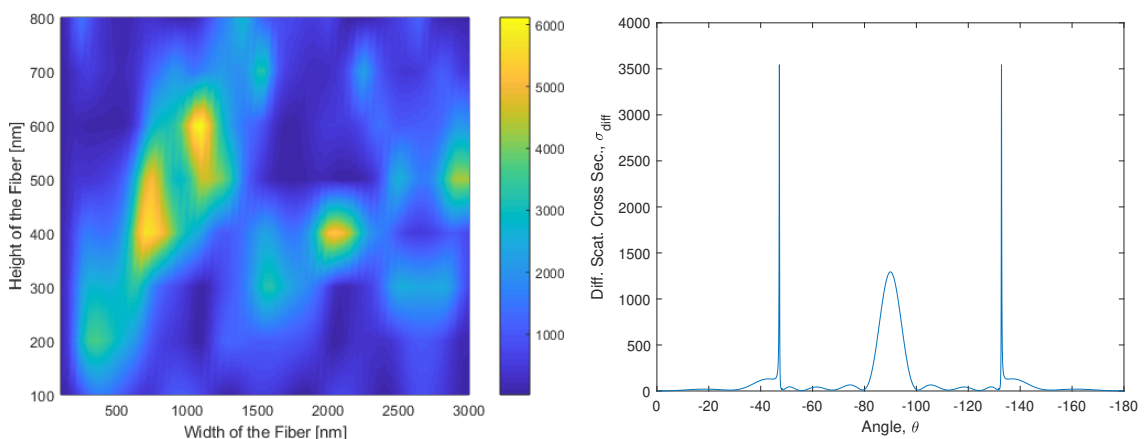


Figure 6.24. The left plot shows the σ_{diff} around the plasmon peaks for every calculated dimension of the fiber. The right plot shows the downwards scattering of a fiber of size $700 \times 2850 \text{ nm}^2$.

This fiber is one of the worst offenders of having "extra effects" overflowing the scattering

pattern, however, the plasmon peaks are still clearly visible and not altered by these effects in any significant capacity. Additionally in figure 6.24, a colorplot is also presented which shows how effective at exciting plasmons the different fiber sizes are. From this plot it can be seen that fibers of different heights again does not agree on which width is the best. It does appear that the 100 nm, 200 nm and 300 nm heights somewhat follow the same trend in regards to the width, however, other heights does not replicate this. The σ_{diff} relative to width for these three heights are shown in figure 6.25, as well as a similar plot for the heights 400 nm, 600 nm and 800 nm.

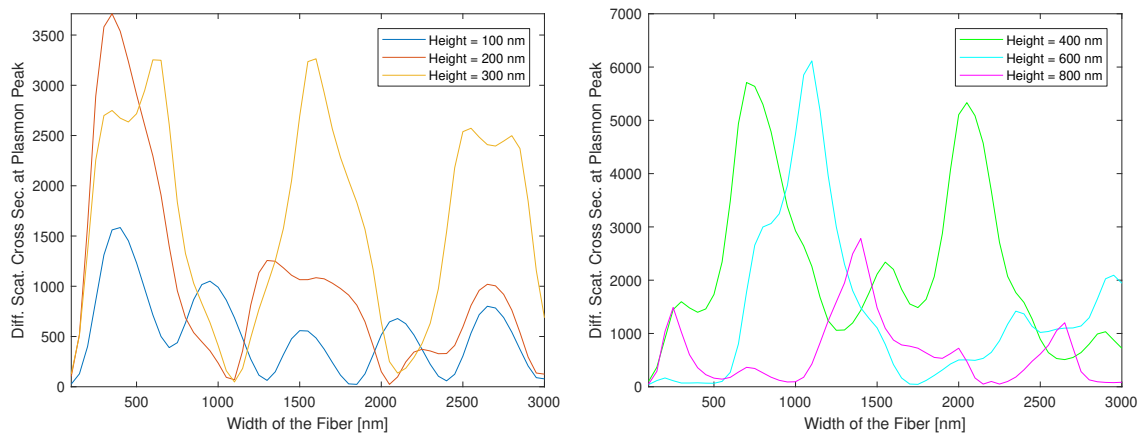


Figure 6.25. Two plots that show σ_{diff} around the plasmon peaks for every calculated widths, with constant heights. The heights in the left plot are 100 nm, 200 nm and 300 nm, and they are 400 nm, 600 nm, and 800 nm for the right.

While it is true that the 100 nm, 200 nm and 300 nm high fibers do have some similar peaks, the 100 nm high fiber is drastically different from the two other with two extra peaks that are present where the rest are at a minimum. This story continue for the higher heights, where none of the plots have peaks at the same widths.

These observation paints the picture that making a rigid and simple formula that predicts which size of the fiber is best at exciting plasmons is more complicated than initially assumed. Even using this incident wavelength that does not have significant loss, it still seem that it becomes to complicated to predict the best fiber, especially when examining the height of the fiber.

6.2.3 Summary

When it comes to the validity of the initial hypothesis, very few things, if any, point towards it being correct in terms of what is examined. For both the 390 nm and 780 nm case, i.e. figures 6.7 and 6.13, the observed oscillations did not diminish when at a width equal to the SPP wavelength of the air-silver interface.

In general, when analyzing the results for larger heights, the oscillation of the peaks becomes irregular and significantly more complicated, as the result changes drastically for just a small change in height. This results in the observations straying even further from the initial hypothesis.

It is also found that, especially when applying a lossy incident wavelength, additional effects appeared for wider fibers, that made it difficult to distinguish the plasmons peaks.

It is believed that the complexity arises with the amount of allowed modes that enables complicated interference of the fields inside of the fiber.

The combination of all these results, points to that making a rigid and simple formula that predicts which size of the fiber is best at exciting plasmons, for any given wavelength, is not possible or at least much more complicated than initially thought. Even using an incident wavelength that does not have significant loss, it still seems that it becomes too complicated to predict the best fiber, especially when including the height of the fiber.

6.3 Near Field Examination and Alternative Hypothesis

In general, when examining the near field inside of the fiber, one does not find results that confirm the initial hypothesis. Examining the effects of a change in fiber width for the near field, one does not find a reliable way of determining whether the fiber provides good plasmon excitation. However, when observing the absolute value of the y -component of the near field inside of the fibers, a specific tendency appears. No matter the width of the fiber, inside the fiber the same standing wave was present. An example of this is shown in figure 6.26, where the near fields inside a 100 nm high fiber, for different widths and an incident wavelength of 780 nm, are shown.

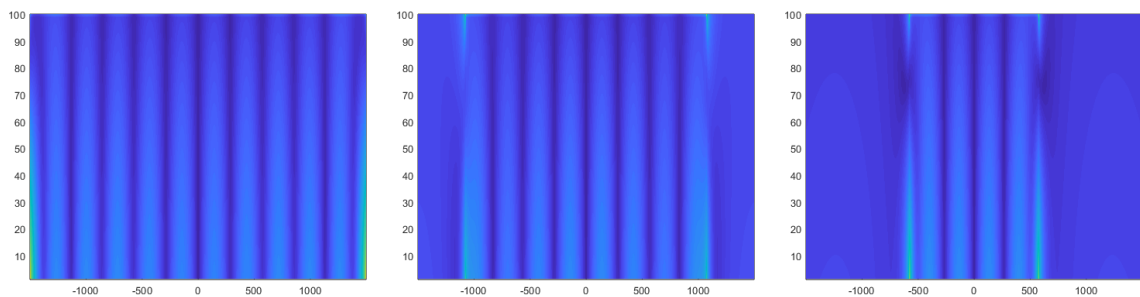


Figure 6.26. Near field for a 100 nm high fiber, from left to right the widths of the fibers are: 3000 nm, 2150 nm and 1150 nm. This shows the standing wave inside of the fiber, that does not change in relation to the width of the fiber. The incident wavelength used is 780 nm and the axes show the position in x and y given in nm.

Examining the field for any one of these fibers, one will find that the wavelength of this standing wave is around 560 nm, which is equivalent to the plasmon wavelength at the fiber-silver interface found for a 100 nm high fiber, Tab. 3.1. Logically this suggests that if the effectiveness of a fiber should be dependent on what happens inside of the fiber, then the period of that should be similar to the wavelength of the SPP inside the fiber. This is in agreement with what was found for the 100 nm high fiber with a 780 nm incident wave, seen in figure 6.13. Here the difference in width between the best fibers at exciting plasmons are exactly the 560 nm that is the plasmon wavelength inside the fiber. However, this is not a general tendency for every height of the fiber or if one uses a lossy incident wavelength. In fact, this only appears for the 100 nm high fiber, with the 780 nm incident wavelength, as the period for every other width becomes irregular and inconsistent. Although it must be said that if one wants to discuss the most general mechanics of exciting plasmons, then this is the fiber that one should examine, as it does not appear to be as affected by the additional effects that higher fibers or lossy incident wavelengths cause.

If one ignore these much more complicated effects and wants to explain why the period of good plasmon excitation is equivalent to the plasmons wavelength inside of the fiber, then a possible hypothesis would be to consider the sides of the fibers as dipoles that excites a plasmon both inside and outside of the fiber. The concept is presented in figure 6.27.

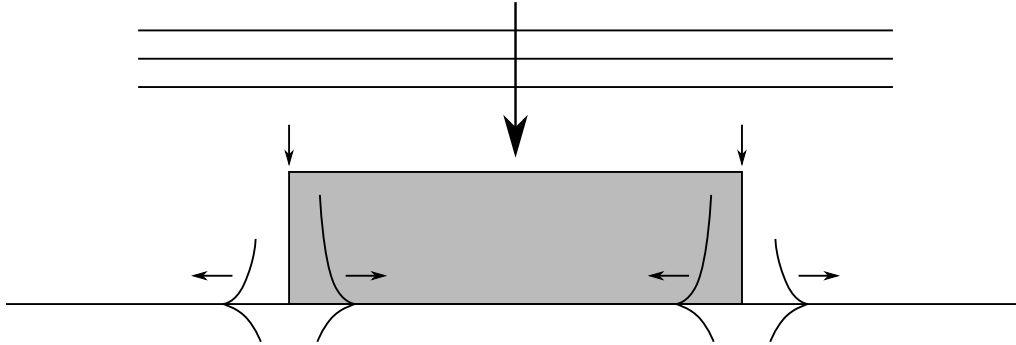


Figure 6.27. Alternative hypothesis for describing what constitutes a fiber that is good at exciting SPPs. If two plasmons are excited at each side of the fiber, then the SPP inside of the fiber must match in phase to the outside SPP on the other side to maximize SPP excitation.

Here it can be seen that each side of the fiber excites an air-silver SPP away from fiber and a fiber-silver SPP inside of the fiber. The relative phase of these SPPs can be difficult to determine, however, When the fiber width matches the phase change of the SPP mode inside the fiber, such that the phase change makes the air-silver SPP mode in phase with the fiber-silver SPP mode, constructive interference happen, resulting in the best SPP excitation.

when the fiber is has a width such that the SPP inside the fiber constructively interfere with the SPP outside of the fiber on the other side, then the SPP excitation would be optimum. When the fiber is then made one fiber-silver SPP wavelength wider, it would again be optimal at exciting plasmons.

Since no further simple examples can be found for the loss-less incident wavelength of 780 nm, without increasing the height, different wavelengths are examined in order to test the validity of the new hypothesis. Here it is calculated only for a 100 nm high fiber, in order to again diminish the complicated effects of a higher fiber and the wavelengths are chosen so to have minimal loss as well. The extra wavelengths that are examined are; 550 nm and 1000 nm. The σ_{diff} around plasmon peaks for different widths are shown for both wavelengths in figure 6.28.

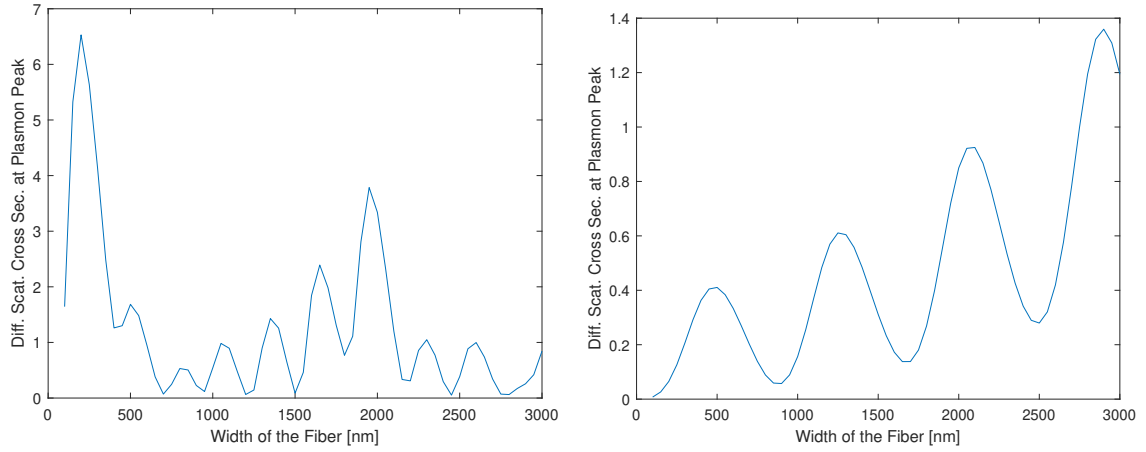


Figure 6.28. Two plots that show σ_{diff} around the plasmon peaks for every calculated widths, both have a height of 100 nm. The left plot is for an incident wavelength of 550 nm, and the right plot for an incident wavelength of 1000 nm.

The mode index for modes inside of a 100 nm high fiber, applying the two wavelengths in question are then found. For the 550 nm wavelength one mode is found with index: $n'_m = 1.7344$ and $n''_m = 0.0111$, resulting in a SPP wavelength of $\lambda_m \simeq 317$ nm. For the 1000 nm wavelength one mode is found with index: $n'_m = 1.2160$ and $n''_m = 0.0009$, resulting in a SPP wavelength of $\lambda_m \simeq 822$ nm.

First the 550 nm wavelength, here it is clear that the oscillation between peaks are much smaller, which also fits with the shorter SPP wavelength. Looking at the difference between each peak it becomes clear that it compares great with the SPP wavelength of 317 nm. As the difference between each peak, which is calculated only for an interval of 50 nm, is always 300 nm or 350 nm.

For the 1000 nm wavelength, a similar effect is observed. The oscillation is, as could be predicted, a lot slower and examining each peak the difference between them is then found to be around 800 nm and 850 nm. This is again in good agreement with the SPP wavelength inside of the fiber.

These results are both in good agreement with the stated hypothesis, as they peak at widths equal to the SPP wavelength, and also do not have oscillations related to other effects. However, these results are, as mentioned, only limited to the case of low fibers, with loss-less incident wavelengths. This points to that the hypothesis might describe an effect inside such a fiber, however, there are more effects that complicate the premise significantly.

It is not trivial to predict at which width the initial peak is present. This can be explained from the hypothesis, as the relative phase between the SPPs outside and inside of the fiber is undetermined. Thus it is unknown at which width the initial phase match will occur.

6.4 Effect of the Thickness of the Silver Film

It is discussed in Ref. [11] that for a thicker silver layer in general gives rise to higher SPP attenuation. The attenuation is zero at a critical thickness, i.e. the SPPs will have the least problem leaking the substrate as possible. Thus there is some thickness, d_{crit} , that is optimal for observing as much leakage radiation as possible, which is typically found to be between 50 - 100 nm [11]. It is not trivial why such a critical thickness exists for thin films, however, the explanation is given in Ref. [29]. Since, at the critical thickness there is no attenuation, k_x must be real. This means that the wave is propagating along the interface, and it can be shown that it also means that the wave is purely evanescent parallel to the interface.

In order to find the critical thickness for the examined structure, five cases have been tested for a thickness ranging from 5-100 nm. The result is shown in figure 6.29.

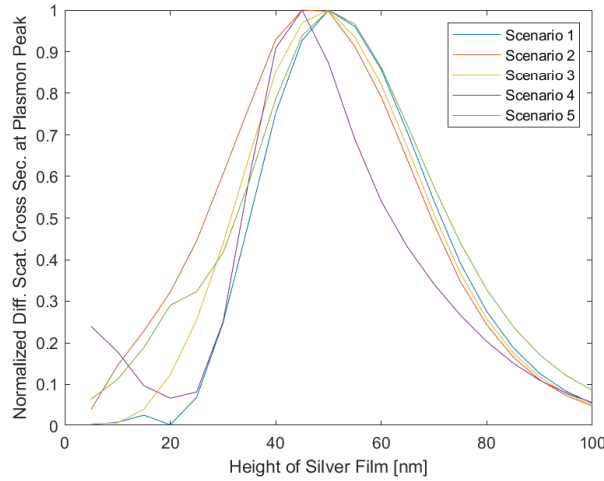


Figure 6.29. A normalized σ_{diff} around the plasmon peaks, for five scenarios, is plotted in order to compare them. Scenario 1: wavelength $\lambda = 780$ nm, width $W = 100$ nm, height $H = 100$ nm. Scenario 2: $\lambda = 780$ nm, $W = 700$ nm, $H = 100$ nm. Scenario 3: $\lambda = 780$ nm, $W = 350$ nm, $H = 200$ nm. Scenario 4: $\lambda = 390$ nm, $W = 300$ nm, $H = 200$ nm. Scenario 5: $\lambda = 390$ nm, $W = 100$ nm, $H = 100$ nm.

In this plot the different scenarios all have their peak centered around $d = 45$ to 50 nm. This points to the critical thickness for the structure to be around the aforementioned thicknesses. This legitimized the used thickness of 40 nm, though the given setups in this report can be further optimized by using the found critical thickness. Examining thicknesses over 100 nm gives more diminished plasmon peaks, as the SPPs cannot leak into the substrate since the silver film is too thick.

However, from figure 6.30, where σ_{diff} for different silver thicknesses for different fibers is shown, it is found that the thickness of the silver film affects the effect the width has on plasmon excitation, similar to how the height affects the plasmon excitation.

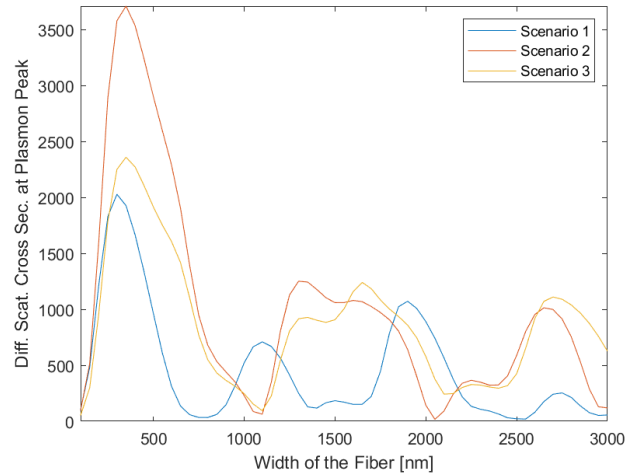


Figure 6.30. The differential scattering cross section is plotted versus the width of the fiber. The height for all plots is 200 nm. The wavelength used is 780 nm. Scenario 1: $d = 20$ nm. Scenario 2: $d = 40$ nm. Scenario 3: $d = 60$ nm.

It is clear that the peaks are not consistent across the plots, hence the best fiber dimensions for some silver thickness is not necessarily the best for another silver thickness, as can be seen by the difference in scenario 1 and 3 in figure 6.30. Since the critical thickness is not consistent for all fiber widths, one cannot determine a singular critical thickness. Figure 6.31 confirms this observation since the critical thickness is not the same as for the plots in figure 6.29.

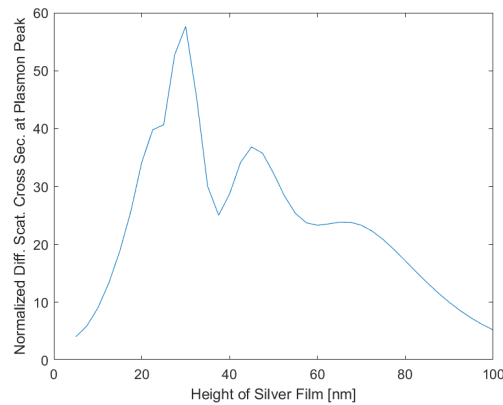


Figure 6.31. The differential scattering cross section plotted versus silver film thickness. The fiber geometry is width is 350 nm and height is 100 nm which is illuminated by light with a wavelength of 390 nm.

The jagged form of figure 6.31 also shows how complicated the critical thickness in reality is to determine.

Chapter 7

Analysis of Results in Three Dimensions

In addition to the dimensions of the fiber, the angles of dipoles inside of the fiber are of great importance. This results in an asymmetric coupling of the SPPs through SHG. In this chapter, this second order effect will be analyzed and the aim will be to maximize this asymmetric coupling, with the possibility of focusing the SPPs in only one direction. This is useful in the case that a photonic component in a photonic circuit is required to only have a strong SPP signal in one direction.

In the works of Ref. [5], [7] and [10] the orientation of the dipoles have so far only been considered to be rotated in the cross sectional plane to the fiber at an angle of 25° from the horizontal axis.

An analysis of the impact that this orientation has on the scattering cross section and asymmetry is of importance to decipher an optimal dipole orientation. The fiber is orientated in space given in figure 7.1.

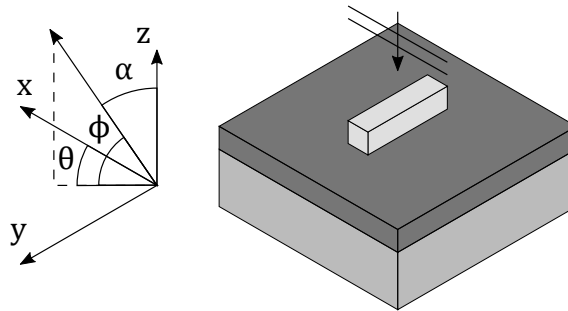


Figure 7.1. Illustration of a fiber placed on a layered structure, the orientation of the fiber in three dimensions is given.

Plots of the differential scattering cross section for SHG will also be calculated for cases where the linear scattering is using the same SH wavelength. This is done in order to demonstrate that the result from linear scattering is applicable to SHG as long as the wavelengths are alike.

Since the 3D computation is demanding in computation time and memory, the resolution of the discretization is downgraded to use $N_d = 16$, i.e. 16 elements per 100 nm, this means that the three dimensional discretization elements are $(6.25 \text{ nm})^3$ in volume.

7.1 Preliminary Theory

The three dimensional simulations are based on the methods discussed in chapter 4. The polarization density, which are give by the orientation of the dipoles, is given in equation (4.31) as

$$\mathbf{P}(\mathbf{r}, 2\omega) = \chi^{(2)} \hat{\mathbf{n}}_{\text{dip}} (\hat{\mathbf{n}}_{\text{dip}} \cdot \mathbf{E}(\mathbf{r}, \omega))^2,$$

where $\hat{\mathbf{n}}_{\text{dip}}$ is the orientation of the dipoles and ω is the angular frequency of the incident FH wave. In a polar coordinate system $\hat{\mathbf{n}}_{\text{dip}}$ is given as

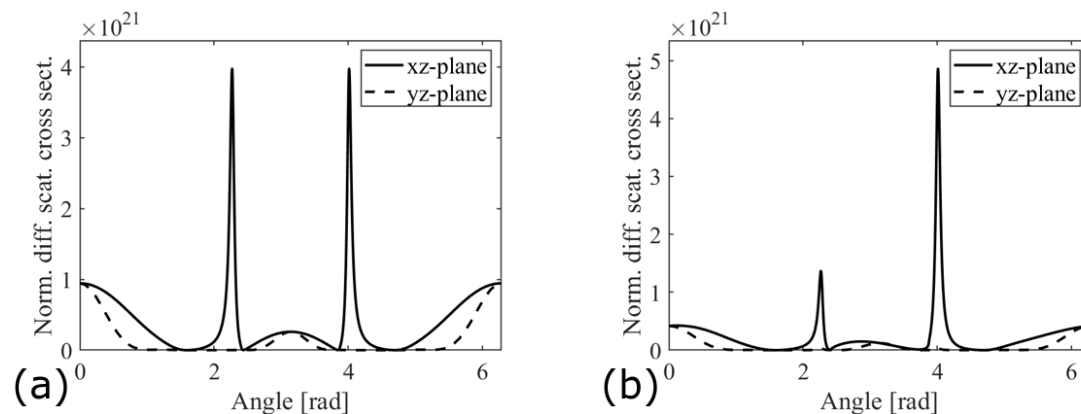
$$\hat{\mathbf{n}}_{\text{dip}} = \hat{\mathbf{x}} \sin \theta \cos \phi + \hat{\mathbf{y}} \sin \theta \sin \phi + \hat{\mathbf{z}} \cos \theta. \quad (7.1)$$

where $\theta \in [0, \pi]$ and $\phi \in [0, 2\pi[$. However, it is easier in this case to refer to the angle between the interface and the dipole, thus $\phi = \pi/2 - \alpha$, where α is that angle. In this context a better notation for θ is β . For the context of this analysis the strength of the SHG effect, $\chi^{(2)}$, has no relevance as it does not effect the angular distribution, thus is set to 1 inside of the fiber and 0 otherwise.

The scattered field from linear scattering is required to calculate the SHG, thus it is necessary to do two full simulations, one for the linear scattering case and one for SHG applying the previous result.

7.2 Asymmetric Coupling by Dipole Orientation

It is a time consuming task to do enough simulations to yield a reasonable resolution of angles tested, thus the angles tested is $\alpha, \beta = \{0^\circ, 30^\circ, 60^\circ, 90^\circ\}$ and their respective combinations. The effect of changing α is presented first, then the additional effects when changing β will be discussed as well. Changing α only changes the radiation pattern in the xz - and yz -plane, thus the results will be examined in these planes. In figure 7.2 the cross sections have been normalized with the physical cross section of the nano-fiber $W \cdot L$, as done in Ref. [10], and the angular resolution is given in radians.



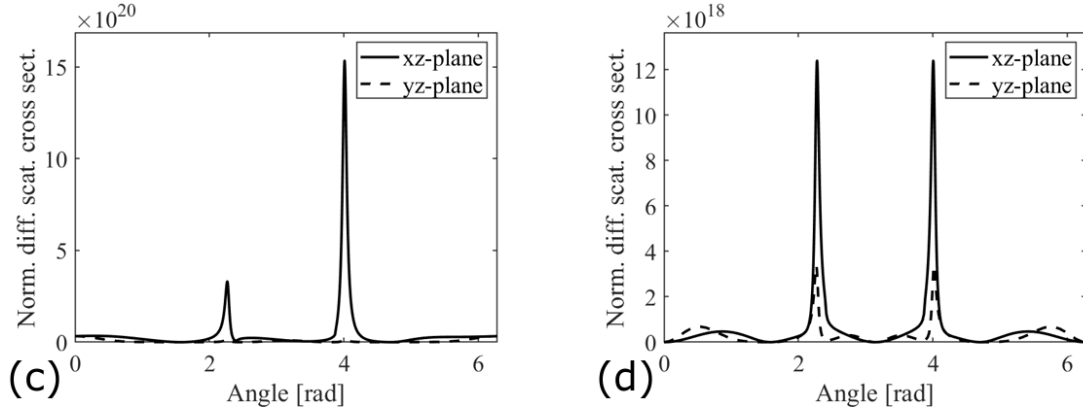


Figure 7.2. Normalized differential scattering cross section is shown for a nano-fiber with refractive index $n_2 = 1.65$ placed on a 40 nm silver film with a quartz substrate, with a SH wavelength of 390 nm. Dimensions of the nano-fiber: height $H = 100$, width $W = 100$ nm, length $L = 400$ nm. Orientation of dipoles: (a) $\alpha = 0^\circ$, $\beta = 0^\circ$. (b) $\alpha = 30^\circ$, $\beta = 0^\circ$. (c) $\alpha = 60^\circ$, $\beta = 0^\circ$. (d) $\alpha = 90^\circ$, $\beta = 0^\circ$.

These plots are cross sections for both the downward and upward scattered field, where the angle is zero in the vertical upwards direction. For now, the analysis focuses on the highest recorded peak. Here the highest SPP-related peaks are shown in Fig. 7.2(b). As could be expected, for both for $\alpha = 0^\circ$ and $\alpha = 90^\circ$ no asymmetry is observed. It is interesting that the for $\alpha = 30^\circ$ the peaks are significantly stronger then for $\alpha = 60^\circ$.

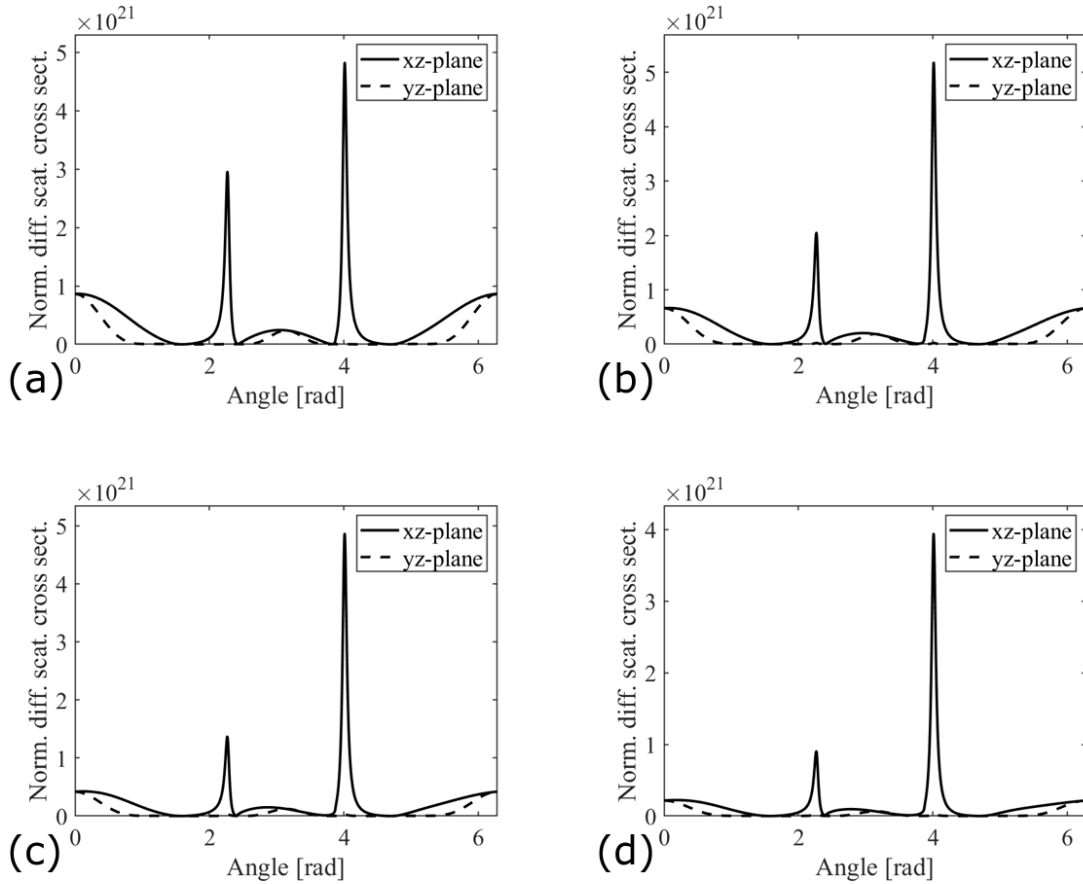


Figure 7.3. These figures are calculated for the same parameters as in Fig. 7.2. However, here $\beta = 0^\circ$ for all plots and (a) $\alpha = 10^\circ$. (b) $\alpha = 20^\circ$. (c) $\alpha = 30^\circ$. (d) $\alpha = 40^\circ$.

In figure 7.3, a test of α with intervals of 10° is conducted and shows that both $\alpha = 10^\circ$ and $\alpha = 30^\circ$ produce similar magnitude of peaks. However, for $\alpha = 20^\circ$ the peaks is marginally larger in comparison. However, if one intends to have the peak as focused in one direction as possible, $\alpha = 20^\circ$ is not an optimal choice, as it is observed that the difference between the two peaks becomes greater for the larger of these angles. So in figure 7.2 the most focused SPP excitation is observed for $\alpha = 40^\circ$, however, this has the weakest overall peak strength.

It would be interesting to see if one could find an angle α , this results in no SPP excitation in one direction. The best angle found is for $\alpha = 80^\circ$, and the result is shown in figure 7.4

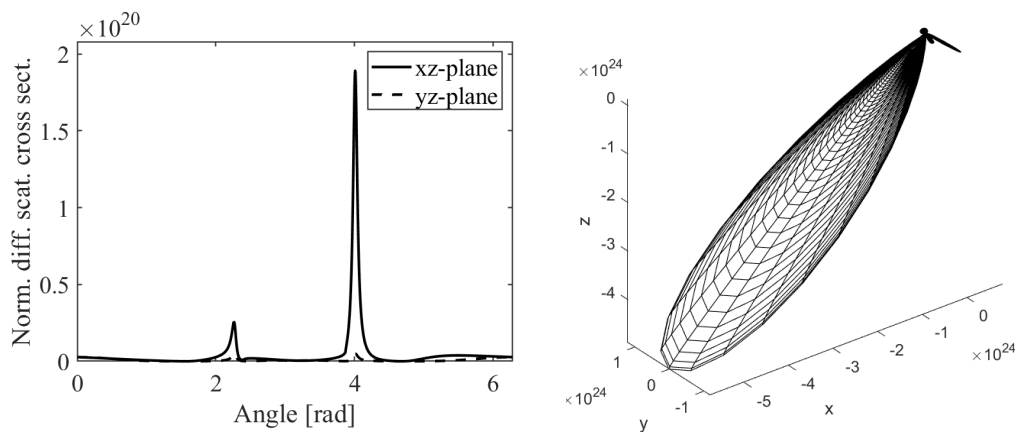


Figure 7.4. These figures are calculated for the same parameters as in Fig. 7.2, however, here the an dipole orientation is given by $\alpha = 80^\circ$ and $\beta = 0^\circ$.

This angle of α results in very focused SPP excitation, however, there is still a minor peak in the opposite direction. However, it is observed that again the overall SPP excitation is significantly weaker than in Fig. 7.3. So for the α it does not seem that one can extinguish excitation in one specific direction without diminishing it in the other. If one examines larger angles, the peaks become symmetrical again, as seen in figure 7.2(d).

For the next part of the analysis, a change in β will be included and examined. Testing the different possible orientations of the dipoles result in the 3D radiation patterns, examples of this is shown in figure 7.5. The axis represented is labeled x , y and z , however they represent the non-normalized differential scattering cross section in respective direction.

It can be seen that in general, for any of the given values of α , that when changing beta the plasmon peaks become significantly smaller. This effect is also observed for the upwards scattering, which also becomes smaller for higher beta. If the dipole is turned by the angle β it becomes partially aligned with length of the fiber, thus essentially the radiation pattern twists such that it follows the new orientation of the dipole.

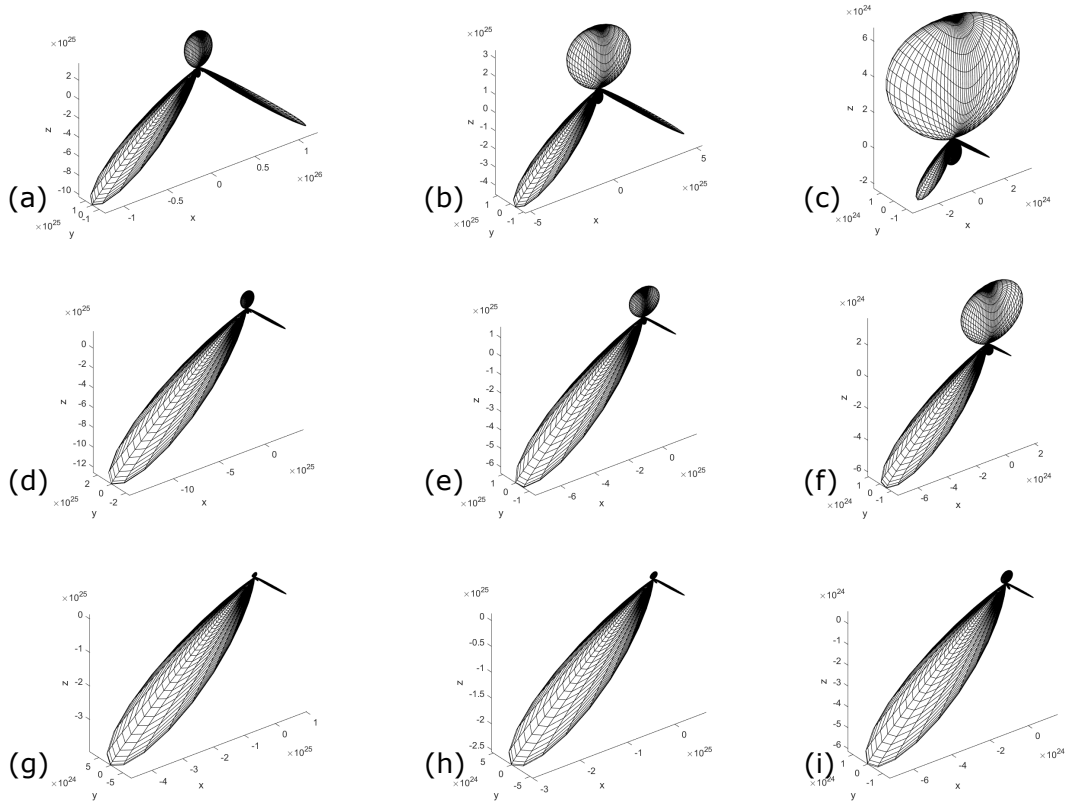


Figure 7.5. These figures are calculated for the same parameters as in Fig. 7.2, however now α and β are both varied. Orientation of dipoles: (a) $\alpha = 0^\circ$, $\beta = 0^\circ$. (b) $\alpha = 0^\circ$, $\beta = 30^\circ$. (c) $\alpha = 0^\circ$, $\beta = 60^\circ$. (d) $\alpha = 30^\circ$, $\beta = 0^\circ$. (e) $\alpha = 30^\circ$, $\beta = 30^\circ$. (f) $\alpha = 30^\circ$, $\beta = 60^\circ$. (g) $\alpha = 60^\circ$, $\beta = 0^\circ$. (h) $\alpha = 60^\circ$, $\beta = 30^\circ$. (i) $\alpha = 60^\circ$, $\beta = 60^\circ$.

This in general results in a shift in the radiation pattern so that it is opposite below and above the air/silver interface. The effect is subtle, but enough to see at closer inspection in e.g. figure 7.6.

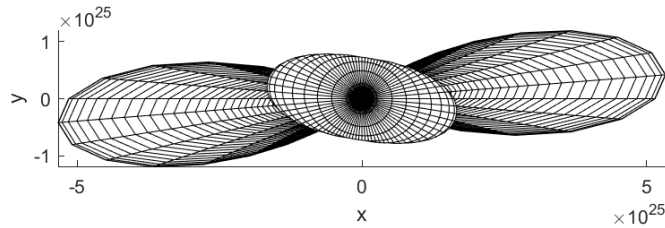


Figure 7.6. Top down view of figure 7.5(b) ($\alpha = 0^\circ$, $\beta = 30^\circ$).

However, the effects of changing beta does not appear to have a positive influence on either the plasmon excitation or plasmon focusing, which is goal in question.

Studying cases where $\beta = 90^\circ$ shows that it is possible to excite SPPs in the parallel direction to the fiber, this is seen in figure 7.7, where $\alpha = 0^\circ$.

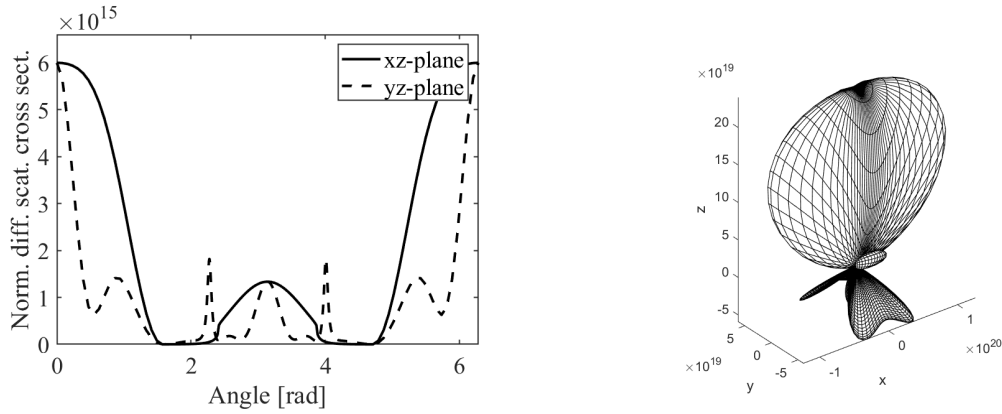


Figure 7.7. These figures are calculated for the same parameters as in Fig. 7.2, however, with $\alpha = 0^\circ$ and $\beta = 90^\circ$.

It is clear from the figure that plasmons excitation parallel to the fiber is achieved, however, it is very weak compared to other plasmon excitation. From this perspective, this is the same case as from a 400 nm wide, 100 nm high and 100 nm long fiber, with an SH wavelength of 390 nm. If one ignores the length, this resembles the case for the two dimensional calculations, in figure 6.8, which resulted in poor plasmon excitation.

It also appears that both parallel and perpendicular plasmon excitation is possible simultaneously, this is shown in figure 7.8, where the dipole orientation is given by the angles $\alpha = 60^\circ$ and $\beta = 90^\circ$.

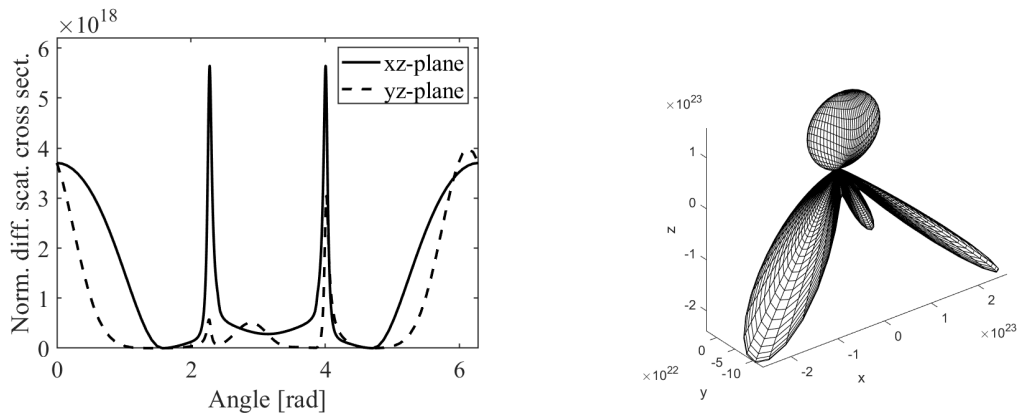


Figure 7.8. These figures are calculated for the same parameters as in Fig. 7.2, however, with $\alpha = 60^\circ$ and $\beta = 90^\circ$.

However, the most predominant features are still the ones diagonally to the fiber.

7.3 Comparing Linear Scattering to SH Scattering

In this section different fiber dimensions will be analyzed and the differential cross section will be calculated. The main purpose is to test that the main results obtained in chapter 6 provide a similar result for the SHG case. Due to three dimensional calculation being much heavier computationally only relatively small fibers is analyzed.

The first data that is presented is for three different fibers, with an SH wavelength of 390 nm. These fibers was all previously examined in chapter 6, for an incident FH wavelength

of 390 nm. In figure 7.9, a clear correlation from the 2D calculations to the SH 3D case with the same SH wavelength is found. The SHG distributes the plasmons predominantly in one direction, however, the form total scattered field matches with what was expected from the 2D calculations.

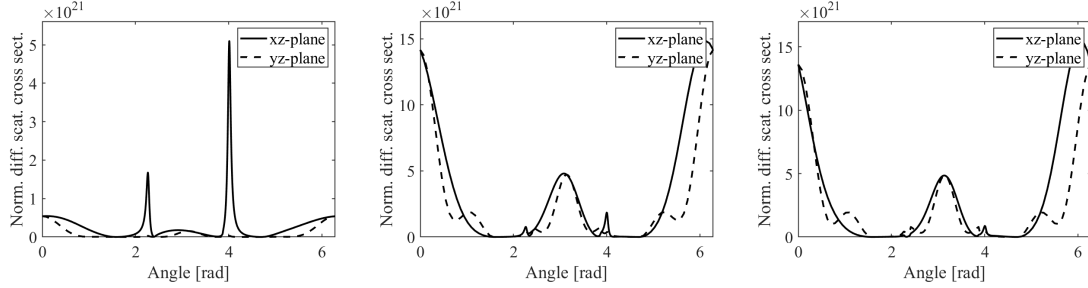


Figure 7.9. These figures are calculated for the same parameters as in Fig. 7.2. The dipole orientation is $\alpha = 25^\circ$ and $\beta = 0^\circ$ and the length of the fiber is set to 400 nm and the height to 100 nm. The widths are: 100 nm, 350 nm and 400 nm respectively

In the rightmost plot in figure 7.9 it is observed that there is clear excitation of SPPs, although minor, even though no SPPs was shown for the equivalent 2D calculations. It is not clear if the plasmons observed in the right most figure, is a result of the finite length of the fiber or a result of SHG. Therefore, is the same fibers calculated in three dimensions, but for linear scattering. This is shown in figure 7.10.

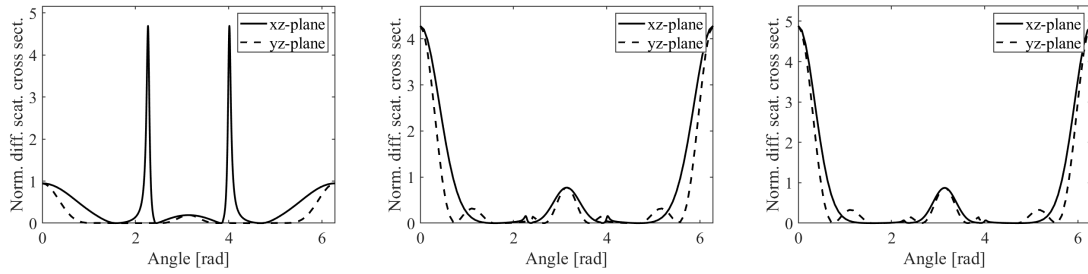


Figure 7.10. These figures are calculated for the same parameters as in figure 7.9. The length of the fiber is set to 400 nm and the height to 100 nm. The widths are: 100 nm, 350 nm and 400 nm respectively

Here it is clear that the peaks are extinguished for the 400 nm wide fiber, thus confirming that the observed peaks is a result of SHG and not the finite length.

Chapter 8

Conclusion

The overall goal of this report, was to examine the mechanics of plasmon excitation by a nanofiber on a silver film on quartz. In order to analyze this, a numerical solution method for both two and three dimensions was constructed.

Effect of the Fiber Dimensions

It was initially hypothesized that fibers with widths equal to the wavelength of the SPP mode outside of the fiber, would result in diminished plasmon excitation. However, this initial hypothesis had to be rejected. As the fibers changed in height, the widths of optimal fibers would change drastically and the result would become unpredictable and irregular.

A new hypothesis was then formulated, which hypothesized that if a given fiber width was optimal for exciting plasmons, then other optimal widths would be wider by an integer of the SPP wavelength inside of the fiber. However, this hypothesis only appeared to be correct if the fibers were low and one did not apply a lossy incident wavelength. In conclusion it does not appear to be possible to construct a simple model for predicting the optimal fiber for plasmon excitation, as there is simply too many effects that interfere.

Effect of the Silver Film Thickness

The efficiency for the SPP excitation for different fiber sizes, was also examined in relation to the thickness of the silver film, d . The critical thickness was found not to be consistent for all widths, thus one was not able to find a singular critical thickness applicable to all fiber sizes.

SHG and Dipole Orientation

In general, the scattering pattern was altered greatly by the change in angles; α and β . However, if one intends to create an asymmetric coupling it is found that one should alter α since the effects caused by changing β did not provide any useful asymmetry. It does not appear that one can focus SPP excitation entirely in one specific direction, however, the angles that provided the most asymmetry also lowered the overall effectiveness of SPP excitation.

It was shown that if the dipoles are orientated along the fiber it is possible to excite SPPs radiating parallel to the fiber. Changing both α and β , coupling in both the parallel and perpendicular directions to the fiber was found to be possible simultaneously.

It was also shown that the results of the two dimensional case could be reconstructed on three dimensions by using linear scattering. Using SHG, the plasmon peaks did not extinguish completely for a fiber with a width of 400 nm, however, the result was still in great correlation to what was found previously.

Bibliography

- [1] Kiat Seng Yeo. *Intellectual Property for Integrated Circuits*. J. Ross Publishing, 2009. ISBN 1932159851.
- [2] The history of the integrated circuit (microchip). <https://www.thoughtco.com/history-of-integrated-circuit-aka-microchip-1992006>, April 2017. Last visited on: 16/5/2019.
- [3] Lene Gammelgaard et. al. Bjarke S. Jessen. Lithographic band structure engineering of graphene. *Nature Nanotechnology*, 14(4):340–346, February 2019. doi: 10.1038/s41565-019-0376-3. URL <https://doi.org/10.1038/s41565-019-0376-3>.
- [4] Francesco Bonaccorso Andrea C. Ferrari et. al. Science and technology roadmap for graphene, related two-dimensional crystals, and hybrid systems. *Nanoscale*, 7(11):4598–4810, 2015. doi: 10.1039/c4nr01600a. URL <https://doi.org/10.1039/c4nr01600a>.
- [5] Paw Simesen, Thomas Søndergaard, Esben Skovsen, Jacek Fiutowski, Horst-Günter Rubahn, Sergey I. Bozhevolnyi, and Kjeld Pedersen. Surface plasmon polariton excitation by second harmonic generation in single organic nanofibers. *Optics Express*, 23(12), 6 2015. ISSN 1094-4087. doi: 10.1364/OE.23.016356.
- [6] Stefan Alexander Maier. *Plasmonics: Fundamentals and Applications*. Springer, 2007. ISBN 0387331506.
- [7] Esben Skovsen, Thomas Søndergaard, Jacek Fiutowski, Paw Simesen, Andreas Osadnik, Arne Lützen, Horst-Günter Rubahn, Sergey I. Bozhevolnyi, and Kjeld Pedersen. Local excitation of surface plasmon polaritons by second-harmonic generation in crystalline organic nanofibers. *Opt. Express*, 20(15):16715–16725, Jul 2012. doi: 10.1364/OE.20.016715. URL <http://www.opticsexpress.org/abstract.cfm?URI=oe-20-15-16715>.
- [8] J. Brewer, M. Schiek, and H.-G. Rubahn. Nonlinear optical properties of CNHP4 nanofibers: Molecular dipole orientations and two photon absorption cross-sections. *Optics Communications*, 283(7):1514–1518, April 2010. doi: 10.1016/j.optcom.2009.12.014. URL <https://doi.org/10.1016/j.optcom.2009.12.014>.
- [9] K. Pedersen, M. Schiek, J. Rafaelsen, and H.-G. Rubahn. Second-harmonic generation spectroscopy on organic nanofibers. *Applied Physics B*, 96(4):821–826,

- August 2009. doi: 10.1007/s00340-009-3688-4. URL <https://doi.org/10.1007/s00340-009-3688-4>.
- [10] Thomas M. Søndergaard. *Green's Function Intergral Equation Methods in Nano-Optics*. CRC Press, 1st edition, 2019. ISBN 978-0-8153-6596-9.
- [11] Lukas Novotny and Bert Hecht. *Principles of Nano-Optics*. CAMBRIDGE UNIV PR, 2006. ISBN 0521832241.
- [12] Erwin Kreyszig. *Advanced Engineering Mathematics*. John Wiley & Sons Ltd, 2011. ISBN 0470646136.
- [13] Heinz Reather. *Surface Plasmons on Smooth and Rough Surfaces and on Gratings*. Springer-Verlag Berlin Heidelberg, 1st edition, 1988. ISBN 978-3-662-15124-2.
- [14] Alex H. Barnett. Greens functions for the wave equation. <https://math.dartmouth.edu/~ahb/notes/waveequation.pdf>, December 2008. Last visited on: 30/5/2019.
- [15] John David Jackson. *Classical Electrodynamics Third Edition*. Wiley, 1998. ISBN 9780471309321.
- [16] Murray R Spiegel. *Schaum's Mathematical Handbook of Formulas and Tables*. McGraw-Hill, 1998. ISBN 0070382034.
- [17] M. Abramowitz and I. A. Stegun. *Handbook of Mathematical Functions*. New York: Dover Publications, 1965. ISBN 9780486612720.
- [18] John R. Reitz, Frederick J. Milford, and Robert W. Christy. *Foundations of Electromagnetic Theory (4th Edition)*. Addison-Wesley, 2008. ISBN 0321581741.
- [19] Tom W B Kibble and Frank H Berkshire. *Classical Mechanics*. Imperial College Pr, 2004. ISBN 1860944248.
- [20] H. Weyl. Ausbreitung elektromagnetischer wellen über einem ebenen leiter. *Annalen der Physik*, 365(21):481–500, 1919.
- [21] V. Pasiskevicius. Nonlinear crystals for solid-state lasers. In *Handbook of Solid-State Lasers*, pages 139–167. Elsevier, 2013. doi: 10.1533/9780857097507.1.139. URL <https://doi.org/10.1533/9780857097507.1.139>.
- [22] M. B. Raschke and Y. R. Shen. Sum-frequency generation at surfaces. *Encyclopedia of Modern Optics (2nd edition)*, pages 184–189, 2004.
- [23] D. E. Aspnes. Local-field effects and effective-medium theory: A microscopic perspective. *American Journal of Physics*, 50(8):704–709, 1982. doi: 10.1119/1.12734. URL <https://doi.org/10.1119/1.12734>.
- [24] A. D. Yaghjian. Electric dyadic green's functions in the source region. *Proceedings of the IEEE*, 68(2):248–263, Feb 1980. ISSN 0018-9219. doi: 10.1109/PROC.1980.11620.

-
- [25] J Nachamkin. Integrating the dyadic green's function near sources. *Antennas and Propagation, IEEE Transactions on*, 38:919 – 921, 07 1990. doi: 10.1109/8.55590.
- [26] George B. Arfken and Hans-Jurgen Weber. *Mathematical methods for physicists*. Elsevier Acad. Press, 2011.
- [27] Mathias Lohne. The computational complexity of the fast fourier transform, 2017. URL <https://folk.uio.no/mathialo/texts/fftcomplexity.pdf>. Last visited on: 29/4/2019.
- [28] Dimitris G. Manolakis and Vinay K. Ingle. *Applied digital signal processing: theory and practice*. Cambridge University Press, 2011.
- [29] J J. Burke, G I. Stegeman, and T Tamir. Surface-polariton-like waves guided by thin, lossy metal films. *Physical review. B, Condensed matter*, 33:5186–5201, 05 1986. doi: 10.1364/OL.8.000383.

Appendix A

Additional Theory

A.1 Boundary Conditions

In order to find the fields on each side of an interface, boundary conditions of Maxwell's equations needs be considered. Such conditions are derived by the integral form of Maxwell's equation which can be found from applying Stokes' and Gauss's theorem. The two theorems are as follows

$$\text{Stokes' Theorem} \quad \oint_{\partial\Sigma} \mathbf{F} \cdot d\mathbf{l} = \iint_{\Sigma} \nabla \times \mathbf{F} \cdot \hat{\mathbf{n}}_s dS, \quad (\text{A.1})$$

$$\text{Gauss's Theorem} \quad \oiint_{\partial\Omega} \mathbf{F} \cdot \hat{\mathbf{n}}_s dS = \iiint_{\Omega} \nabla \cdot \mathbf{F} dV, \quad (\text{A.2})$$

where \mathbf{F} is some vector field, Σ is some fixed surface with closed boundary curve $\partial\Sigma$, Ω is some fixed volume with closed boundary surface $\partial\Omega$ and $\hat{\mathbf{n}}_s$ is the normal vector to the surface. Applying these theorems yields the Maxwell's equations in integral form [11],

$$\oint_{\partial\Sigma} \mathbf{E}(\mathbf{r}, t) \cdot d\mathbf{l} = - \iint_{\Sigma} \frac{\partial \mathbf{B}(\mathbf{r}, t)}{\partial t} \cdot \hat{\mathbf{n}}_s dS, \quad (\text{A.3})$$

$$\oint_{\partial\Sigma} \mathbf{H}(\mathbf{r}, t) \cdot d\mathbf{l} = \iint_{\Sigma} \left(\mathbf{J}_s(\mathbf{r}, t) + \frac{\partial \mathbf{D}(\mathbf{r}, t)}{\partial t} \right) \cdot \hat{\mathbf{n}}_s dS, \quad (\text{A.4})$$

$$\oiint_{\partial\Omega} \mathbf{D}(\mathbf{r}, t) \cdot \hat{\mathbf{n}}_s dS = \iiint_{\Omega} \rho_s(\mathbf{r}, t) dV, \quad (\text{A.5})$$

$$\oiint_{\partial\Omega} \mathbf{D}(\mathbf{r}, t) \cdot \hat{\mathbf{n}}_s dS = 0. \quad (\text{A.6})$$

Consider the integral equation (A.3). If the integral is done over the line path as shown in figure A.1 and letting the side of the box collapse such that only the electric field parallel to the interface is considered, the first boundary condition can be found.

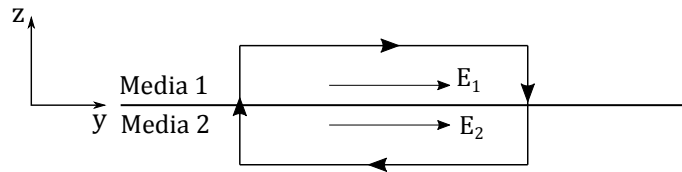


Figure A.1. A rectangular line path shown to cross the interface of two media with different dielectric constant. The parallel component to the interface of an electric field is shown.

Assuming that there is no surface charge density the same result can be found for the magnetic field using (A.4) [11][18],

$$E_{1y} = E_{2y} \quad \text{which can be written in vector form as} \quad \hat{\mathbf{n}}_s \times \mathbf{E}_1 = \hat{\mathbf{n}}_s \times \mathbf{E}_2, \quad (\text{A.7})$$

$$H_{1y} = H_{2y} \quad \text{which can be written in vector form as} \quad \hat{\mathbf{n}}_s \times \mathbf{H}_1 = \hat{\mathbf{n}}_s \times \mathbf{H}_2. \quad (\text{A.8})$$

Similar relations can be found by considering a three dimensional box that spans across the interface, this is known as a Gaussian pillbox and is shown in figure A.2.

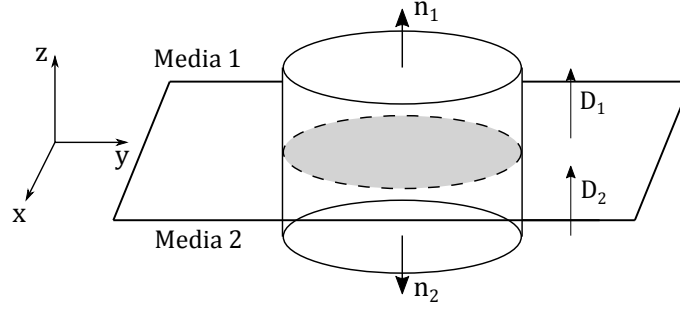


Figure A.2. A box that spans across two media with different dielectric constant. This box is also known as a Gaussian pillbox. The parallel component of the displacement field at the interface is shown

As before, letting the structure collapse towards the interface, normal contributions vanish and only the top and bottom of the pillbox needs be considered. Assuming there are no surface charges and the media are non-magnetic, equations (A.5) and (A.6) can be applied to find that [11][18]

$$D_{1z} = D_{2z} \quad \text{which can be written in vector form as} \quad \hat{\mathbf{n}}_s \cdot \mathbf{D}_1 = \hat{\mathbf{n}}_s \cdot \mathbf{D}_2, \quad (\text{A.9})$$

$$B_{1z} = B_{2z} \quad \text{which can be written in vector form as} \quad \hat{\mathbf{n}}_s \cdot \mathbf{B}_1 = \hat{\mathbf{n}}_s \cdot \mathbf{B}_2. \quad (\text{A.10})$$